THESIS

INTRASEASONAL VARIABILITY IN THE DIURNAL CYCLE OF PRECIPITATION IN THE PHILIPPINES

Submitted by
Michael B. Natoli
Department of Atmospheric Science

In partial fulfillment of the requirements
For the Degree of Master of Science
Colorado State University
Fort Collins, Colorado
Spring 2019

Master's Committee:

Advisor: Eric D. Maloney

Michael M. Bell
Jeffrey D. Niemann

Copyright by Michael B. Natoli 2019

All Rights Reserved

ABSTRACT

INTRASEASONAL VARIABILITY IN THE DIURNAL CYCLE OF PRECIPITATION IN THE PHILIPPINES

Precipitation in the region surrounding the South China Sea (SCS) over land and coastal waters exhibits a strong diurnal cycle associated with a land-sea temperature contrast that drives a sea-breeze circulation. The boreal summer intraseasonal oscillation (BSISO) is an important modulator of the daily mean precipitation rate and the amplitude of the diurnal cycle. Using 19 years of the CMORPH precipitation product for the Philippines, it is shown that in aggregate the diurnal cycle amplitude is maximized before the arrival of the broader oceanic convective envelope associated with the BSISO. Over Luzon Island in the northern Philippines, the diurnal cycle amplitude is not in phase with daily mean precipitation, which peaks with the large-scale BSISO convection. An increase in nocturnal and morning precipitation more than compensates for the reduced precipitation rates during the afternoon peak amidst the BSISO active period. This pattern is not seen over Mindanao Island in the southern Philippines, where diurnal cycle amplitude tends to determine daily mean precipitation. A strong diurnal cycle in coastal waters west of the Philippines is evident in the transition from the inactive to active phase, due to offshore propagation of convection generated over land.

This behavior is dramatically different on small spatial scales within the Philippine archipelago, depending strongly on topography. For example, the BSISO influence on the diurnal cycle on the eastern side of the high mountains of Luzon is nearly opposite to the western side. It is proposed, using wind, moisture, and radiation budget products from the ERA-Interim reanalysis, that the enhanced diurnal cycle over land and coastal waters west of the mountains during BSISO suppressed phases is a consequence of increased insolation and weaker prevailing onshore winds. Offshore propagation, and thus the diurnal cycle over the coastal waters of the SCS, is suppressed until ambient mid-level moisture increases during the transition to the active BSISO phase. In the BSISO enhanced phases, strong low level winds out of the southwest combine with increased cloudiness to suppress the sea-breeze circulation and thus the diurnal cycle of precipitation in the SCS region. Strong frictional moisture convergence leading the BSISO is not found to be concurrent with the peak in the diurnal cycle. Results are consistent when examined in other precipitation products or BSISO indices, and support conclusions derived from studies focusing on intraseasonal modulation of precipitation in other regions of the Maritime Continent, with some important local distinctions owed to geography.

ACKNOWLEDGEMENTS

This work was supported by the Climate and Large-Scale Dynamics program of the National Science Foundation under grant AGS-1441916 and by the Office of Naval Research under PISTON grant N00014-16-1-3087.

TABLE OF CONTENTS

LIST OF FIGURES

Chapter 1

Introduction

1.1 Purpose

The Madden-Julian Oscillation (MJO) has extensive impacts over a vast portion of the world, despite its convective signal being confined to a narrow band of the tropics (Madden and Julian 1972, Knutson and Weickmann 1987, Hendon and Salby 1994). The MJO is a large, slowly eastward propagating area of active convection in the tropical atmosphere (Madden and Julian 1972, 1994). Enhanced convective activity leads to increased storminess, and thus elevated latent heating to the troposphere via the condensation of water vapor. Potent heating in the tropical atmosphere generates waves that reach across the planet, akin to the ripples created after dropping a stone in a calm body of water. If a stone is instead dropped into a disturbed body of water, the ripples may not be visible to the naked eye. The global climate system is more comparable to a disturbed body of water, such that understanding the impact of one particular wave signal becomes complicated, amidst all of the other signals and noise.

Despite decades of research and significant progress on the MJO, a complete understanding of the phenomenon remains out of reach, particularly for the Northern Hemisphere summer (Jiang et al. 2018). The MJO is also of particular interest because of its unique time-scale of about 30-60 days, providing the potential for prediction skill of remote weather patterns on subseasonal to seasonal timescales (Zhang 2013). This study intends to add another piece of the MJO puzzle by illuminating the impact on precipitation in the Philippines and South China Sea, in the hopes of providing clarity for a largely overlooked component of the MJO system and inspiring future research towards a comprehensive theory encompassing all seasons and all regions affected. This firs chapter will include a discussion of the body of literature relating to the diurnal cycle of precipitation over land and ocean, the background state in the region of MJO activity, the dynamics of the MJO, and finally the interactions between the MJO and the diurnal cycle, highlighting along the way the gaps in the collective knowledge of the field this study aims to fill.

1.2 The Diurnal Cycle

1.2.1 The Oceanic Diurnal Cycle

The diurnal cycle of precipitation over tropical oceans has been of interest to the community for much of the last century. Before the advent of satellite technology, this was a much more difficult problem to address. Despite such challenges, several pioneering efforts were made to understand these patterns. Kraus (1963) used observations from a number of weather ships operating across the global oceans to estimate the diurnal cycle, and found a distinct nocturnal maximum in precipitation frequency, and related this to the diurnal cycle in radiation. While these observations were outside of the tropics, they still mark a major step forward in studying the oceanic diurnal cycle. Specifically, Kraus argued that there is more cooling at night from longwave radiation at cloud top than at cloud base, which increases the instability and enhances convection. Additionally, he proposed that during the day, shortwave radiation heats the cloud tops, providing a stabilizing influence. This direct radiation-convection interaction hypothesis has been explored extensively in the literature and remains one of the major possible mechanisms today (Wallace 1975, Randall et al. 1991). Another suggested mechanism was the semi-diurnal solar tide in surface pressure, leading to modulation of convergence and divergence (Brier and Simpson 1969). Deser and Smith (1998) later found that the semi-diurnal cycle dominates zonal wind, whereas the diurnal cycle is most important for meridional wind, which is more important for convergence at the equator. While Deser and Smith did not relate their findings back to precipitation, S. Yang and Smith (2006) found that the oceanic diurnal cycle has a tendency for a primary and secondary maximum, but that it is not semi-diurnal in nature, reducing the popularity of the solar tide hypothesis (Lindzen 1978).

Gray and Jacobson (1977) presented another alternative hypothesis based on an indirect interaction between radiation and convection. Their results corroborated the idea of a strong morning maximum in deep convection over tropical oceans, reporting significantly greater precipitation in the morning compared to the evening, particularly over the West Pacific. They found a different pattern over the region of study for the Global Atmospheric Research Program (GARP) Atlantic Tropical Experiment (GATE) field campaign in the tropical Atlantic, with an afternoon precipitation maximum, and minimum near midnight. To explain this, they suggested that the disparity in the GATE region was a result of the high frequency of squall lines in that region initiated from Africa in an environment of greater vertical wind shear. In the West Pacific, where squall lines are infrequent, a different mechanism was required. They rejected the idea of radiation inducing stability changes, asserting that these changes would be too small. Instead, they purported that the cloud free region experiences more radiational cooling at night, which leads to compensating subsidence warming, which further enhances convergence into the convective region. This hypothesis has been supported by many studies since (e.g. Folz and Gray 1979, McBride and Gray 1980, Ackerman and Cox 1981) and remains in consideration today (Ruppert and R. Johnson 2016, Klotzbach et al. 2017).

While the mechanism remained an area of debate, more evidence came out over the years to support the idea of a morning precipitation maximum over open water, but with more nuance. Satellite technology allowed for a novel look at the diurnal cycle using infrared retrievals, which give an estimate of cloud top height, a proxy for rainfall. In a study of the diurnal cycle in August of 1979, Augustine (1984) found that while the first harmonic of the diurnal cycle dominated, with a maximum near dawn, a semi-diurnal cycle was also evident, adding to a secondary maximum in the mid-afternoon. Albright et al. (1985) found two primary modes of convective variability in January-February 1979 on diurnal time scales, one with an afternoon maximum found in the South Pacific Convergence Zone (SPCZ) and GATE regions, and another in which convective activity increases overnight towards a sunrise maximum, found in the Inter-Tropical Convergence Zone (ITCZ). The dominance of the first harmonic over the second harmonic suggests that the solar tide mechanism (Brier and Simpson 1969) could not be the primary driver. Furthermore, the mechanisms of Kraus (1963) and Gray and Jacobson (1977), while plausible for the sunrise maximum, are unable to explain the other mode of diurnal variability with an afternoon maximum.

Hartmann and Recker (1986) analyzed outgoing longwave radiation retrievals from several satellites and found that the diurnal cycle of high clouds is completely out of phase with the diurnal cycle of mid-level and low clouds. Nevertheless, they found a maximum in OLR, corresponding to a minimum in cloudiness in from 0600 to 1200, consistent with previous observations in the SPCZ. This out of phase relationship was also seen to some extent by Gray and Jacobson (1977). As the satellite era drew on, the community had access to longer time series of infrared observations of tropical clouds, allowing some composite studies to add more to the story. Janowiak et al. (1994) found that the diurnal cycle of oceanic brightness temperature was highly sensitive to the selection of threshold used to define deep convection. The coldest (highest) cloud tops were found to peak in the early morning, much earlier than the diurnal cycle of warmer (mid-level) cloud tops, supporting the findings of Hartmann and Recker (1986). Nitta and Sekine (1994) used nine years of brightness temperature retrievals from geostationary satellites to paint a comprehensive picture of the global diurnal cycle. Over open ocean, they noted a weak diurnal cycle over the ITCZ and SPCZ, peaking in the morning, with a secondary maximum in the afternoon. These authors also found some seasonal variability in the character of the diurnal cycle. Evidence for a pronounced morning maximum in oceanic precipitation was supported by further studies of brightness temperature retrievals and station observations (e.g. G.-Y. Yang and Slingo 2001, Dai 2001).

Concurrently, the community was building an understanding of the mechanisms that produce this oceanic diurnal cycle with advances in modeling. Randall et al. (1991) simulated the diurnal cycle of convection using a general circulation model GCM, finding that it can actually perform quite well in replicating the observed diurnal cycle in a control run. Experiments showed that the early morning maximum in rainfall over the open ocean, albeit weaker than observed, was simulated by the model. When the radiative impacts of clouds were omitted from the model, a diurnal cycle of the same phase was still simulated, but it was of much weaker amplitude. While their results showed that the diurnal cycle over open ocean can be qualitatively explained by direct interaction between radiation and convection (Kraus 1963), they noted that this is not mutually exclusive with the indirect mechanism proposed by Gray and Jacobson (1977), which could also be important. The model of Liu and Moncrieff (1998) also suggested that direct radiation-convection interaction was the primary modulator, but that the difference between cloud and cloud-free radiation, proposed by Gray and Jacobson (1977) was less important.

The Tropical Ocean Global Atmosphere Coupled Ocean-Atmosphere Response Experiment (TOGA COARE) field campaign in the equatorial west Pacific ocean in 1992-1993 added significantly to the collective understanding of the oceanic diurnal cycle. Sui et al. (1997) used observations collected during TOGA COARE augmented by satellite observations to demonstrate that diurnal precipitation can be grouped into three stages: warm morning cumulus, afternoon convective showers, and nocturnal convective systems. They showed that while afternoon precipitation comes from more scattered convective cells, the nocturnal rainfall maximum consists of deep convection and broad stratiform precipitation. These stages also fit nicely into the trimodal distribution of the cloud population proposed by R. Johnson et al. (1999). Chen and Houze (1997) found that the prevalence of clouds in each of these stages varies on intra-seasonal time scales. This will be further elaborated on in section 1.4.

As more precipitation estimates derived from satellite microwave retrievals became available, many studies in the 21st Century took advantage of these rich datasets to explore the oceanic diurnal cycle. Furthermore, microwave observations are generally more accurate than infrared since they respond more directly to precipitation, rather than high clouds (Yamamoto et al. 2008). These measurements also allowed researchers to explore some more detailed features of the cloud population at different times of day. Nesbitt and Zipser (2003) found that the morning maximum in oceanic precipitation is almost entirely due to mesoscale convective systems (MCS), and that non-MCS precipitation contributes relatively little to the diurnal cycle. They showed that MCSs are significantly more common during the early morning hours, and this drives the diurnal cycle in precipitation, rather than more intense rainfall. Comparatively little signal was found in the convective intensity as a function of time of day. Thus, they asserted that the nocturnal environment is more suitable for the development of MCSs and for MCSs to last longer, which drives the observed pattern. These findings help explain the disparity in the diurnal cycle based on cloud level considered found by Hartmann and Recker (1986) and Janowiak et al. (1994).

Studies by S. Yang and Smith (2006, 2008) found that oceanic convective rainfall is 25% greater at night with an early morning maximum, and a secondary maximum in the afternoon, while the contributions from stratiform and convective processes are fairly consistent. While much of the focus of the community was on deep, organized convection, the diurnal cycle of shallow convection is also of interest. Ruppert and R. Johnson (2016) found that diurnal warm layers in the ocean surface are important for forcing the afternoon mode of shallow convection previously discussed. Diurnal warm layers preferentially form when the sky is clear and the winds are calm (Matthews et al. 2014), and actually contribute a nonlinear process to the atmosphere, as removing the diurnal cycle of SST significantly reduces rainfall and convection (Ruppert and R. Johnson 2016). Similar importance of the diurnal warm layer in undisturbed periods over open ocean in driving the secondary afternoon maximum in precipitation is evident in other studies (e.g. Sui et al. 1997, Sakaeda et al. 2018). While there is now a consensus on the timing and convective make-up of the oceanic diurnal cycle, the mechanism driving it is still somewhat of an open question. It is unclear even after decades of research if the direct or indirect radiation-convection interaction mechanism is most important, but both are still widely accepted as possibilities (Ruppert and R. Johnson 2016, Klotzbach et al. 2017). In recent years, this question has fallen out of favor, and more work has been dedicated to understanding the variability of the diurnal cycle, which will be the subject of section 1.4.

1.2.2 The Continental Diurnal Cycle and Maritime Continent

Over land, measuring the diurnal cycle of precipitation is substantially easier since the signal is generally stronger and stationary observations with long records are available. As a result, the quest to understand continental diurnal cycle has a less dramatic history. The idea that land-based convection peaks in the afternoon is more widely known by the scientific community and the general public. Nevertheless, many studies over the years have worked to establish and understanding of the mechanisms that cause In coastal regions, the land heats up faster than nearby oceans due to its lower thermal inertia, which leads to a sea-breeze circulation that then drives convergence and convection over land (Pielke 1974). Similarly, mountain slopes heat up faster under the solar load compared to the free-atmosphere above the valley. The more buoyant air on the mountain slopes rises, forcing upslope flow (Rampanelli et al. 2004, Hughes et al. 2007). Kousky (1980) showed that sea- and mountain-valley breezes contribute significantly to an observed afternoon maximum in land-based precipitation over northeast Brazil over elevated terrain, with a nocturnal maximum in mountainous valleys. Mapes et al. (2003a) demonstrated the presence of an afternoon peak in precipitation over the high mountains of the Andes in Colombia, with nocturnal maxima observed over low-lying terrain surrounded by mountains, such as Lake Maracaibo. This afternoon maximum was also observed over Australia both in the tropics and subtropics by Keenan and Carbone (2008). Others have noted a favored afternoon maximum in the Rocky and Appalachian mountains in North America (Carbone and Tuttle 2008). A series of global studies showed that this pattern is found all across the world (Cairns 1995, Nitta and Sekine 1994, Dai 2001, G.-Y. Yang and Slingo 2001, Nesbitt and Zipser 2003, S. Yang and Smith 2006, 2008, Kikuchi and B. Wang 2008).

While the prevalence of this pattern all around the world is quite intriguing, that is not the focus of this thesis. Instead, of greatest interest is the diurnal cycle of precipitation over the Maritime Continent (MC), a major source of convective heating for the global atmosphere (Ramage 1968). With its complex topography situated amongst some of the warmest sea surface temperatures (SST) on Earth, the MC makes understanding precipitation patterns much more difficult. To accurately capture the detailed features of the diurnal cycle over this region in a model, high enough resolution to resolve clouds is often required (Birch et al. 2015). Furthermore, errors in a global climate model in this region cascade into immense errors from pole to pole (Neale and Slingo 2003). An understanding of the variability of the diurnal cycle is still incomplete, so this thesis aims to add new information to the body of work, focusing on the less studied boreal summer season. The rest of this section will summarize the body of work on the MC diurnal cycle to date.

Qian (2008) succinctly described the mechanisms controlling the mean state diurnal cycle over the MC. Their model runs showed that daytime differential heating of the landmass causes sea-breeze circulations that later converge near the center of the the MC islands, and combine with mountain-valley breezes to enhance convection over mountains. Cells begin to merge and organize, particularly over larger islands. This study also demonstrated that the representation of the complex topography of the MC is very important, by showing a significant underestimation of precipitation when topography was removed, and dramatic impacts on the general circulation of the atmosphere due to the loss in latent heating. These findings have also been corroborated by many other studies using radar, satellite observations, and models (Cairns 1995, Dai 2001, Nesbitt and Zipser 2003, Mori et al. 2004, Tabata et al. 2011, Biasutti et al. 2012). Mori et al. (2004) also went further to show the diurnal cycle of convective and stratiform precipitation, showing that over Sumatra island, the convective peak is brief and comes early, followed by a peak in stratiform rainfall later in the evening, indicating a transition from convective to stratiform after peak precipitation.

Numerical simulations by Saito et al. (2001) showed some disparity between the windward and leeward sides of the Tiwi Islands near Australia. On the windward side, the sea-breeze front moves faster, but convection is shallower and less organized. Conversely, convection on the leeward side of terrain is more well defined, with stronger updrafts. They note that the convergence zone sets up leeward of the island's center, and invigorates the updrafts. It is unclear if the results can be generalized to the rest of the MC. This subject will be explored in later chapters of this thesis. Dai (2007) used satellite derived precipitation estimates to show that the diurnal cycle over MC islands is primarily due to changes in the frequency of precipitation, not the convective intensity, similar to the findings of Chen and Houze (1997) over open water, and supported by gauge analysis by Kanamori et al. (2013). While examining the diurnal cycle over tropical landmasses, a number of studies have also noted a pronounced tendency for offshore propagation of convective systems into near coastal waters overnight (e.g. G.-Y. Yang and Slingo 2001, Mapes et al. 2003a, Kikuchi and B. Wang 2008).

1.2.3 The Coastal Diurnal Cycle

After a field campaign studying the boreal winter monsoon in the Maritime Continent, Houze et al. (1981) presented new observations from Borneo, one of the largest islands of the MC. The authors presented evidence for an extremely regular diurnal cycle over both land and ocean. They proposed that the diurnal cycle offshore was initiated by the overnight land breeze converging with the background northeasterly winds associated with the monsoon system. Later in the night, convective cells merge and consolidate, continuing until the land breeze ceases during the morning hours. Then, convection decays over the ocean and shifts to the island.

This hypothesis has been explored extensively in the literature, frequently using the island of Sumatra as a case study. Mori et al. (2004) used microwave-derived satellite precipitation estimates to argue that diurnal convection over Sumatra propagates both directions away from the peak topography in the center of the island. Convection is initiated by the sea-breeze, and then propagates to the northeast in the evening hours, which they propose is because of the background westerly wind in the lower troposphere. Anvils are sheared off to the west by easterlies in the upper troposphere. Similarly, the land-breeze initiates further convection on the southwest coast of the island, which then propagates further offshore, but a different mechanism (to be discussed later) is proposed to explain this. Notably, they also indicate that the amplitude of the diurnal cycle decreases as convection gets further from shore.

Sakurai et al. (2005) employed satellite infrared retrievals to paint a similar picture. They note propagation in both directions from the initiation over Sumatra's high topography, up to 500-km away, with the westward direction dominating. The authors argued that westward propagation was due to the upper-tropospheric easterlies, and noted that eastward propagation occurs most frequently when the low level flow has an easterly component, similar to the hypothesis of Mori et al. (2004). Similarly, Yanase et al. (2017) used composites from nearly two decades of satellite retrievals to argue that when the entire profile consists of easterlies, convective and stratiform rainfall propagate westward. However, when lower-tropospheric winds are westerly, convective systems are advected eastward, while stratiform precipitation is still sheared off to the west. Tulich and Kiladis (2012) suggested that it is the wind shear, not the mean flow at any layer, that favors predominant propagation to the west.

While compelling, the argument that this apparent propagation of diurnal convection is driven by the land and sea breezes interacting with the background flow cannot fully explain the observations. Ohsawa et al. (2001) showed that the land breeze is too weak, and it begins too late in the night to be the sole mechanism. They also note that an offshore maximum in precipitation is evident even when the prevailing monsoonal flow is offshore. G.-Y. Yang and Slingo (2001) performed an exhaustive analysis of the global diurnal cycle, and noticed a dramatic tendency for offshore propagation around the MC islands. An estimation of the propagation speed of these features lead them to hypothesize that gravity waves were responsible.

In a study focusing on the Andes mountains of Colombia near the eastern Pacific ocean, Mapes et al. (2003b) used a mesoscale model to propose gravity waves as the the main mechanism driving offshore propagation, and hypothesized that this mechanism could play a role in other regions, like the MC. They postulated that gravity waves are initiated in the presence of elevated heating over high topography amongst the surrounding stratified layers. The wave propagates offshore at about 15 ms^{-1}, close to the pace of offshore propagation of diurnal convection. As the gravity wave passes, there are small changes in temperature in the low to mid-troposphere that are enough to change the sign of the buoyancy of low-level air after midnight. While they believed that waves should propagate both west and east, they argued that the lack of eastward propagation could be explained by interference from other convective patterns over the Amazon. In their 2004 study, Mori et al. also proposed gravity waves as a potential driver of propagation offshore to the southwest of Sumatra. Tulich and Kiladis (2012) argued that some diurnally propagating squall lines fit the dispersion curves of convectively coupled intertia-gravity waves.

Love et al. (2011) provided convincing evidence that gravity waves are an important contributor to diurnal phase propagation over Sumatra island using satellite observations in addition to a regional model run at varying resolutions. They proposed that the transition to a convective heating profile over high topography in the early afternoon initiates a deep gravity wave that propagates rapidly offshore, inducing downwelling and thus adiabatic warming and stabilization in the mid-levels. When the heating profile over land transitions back to one of stratiform precipitation, another shallower gravity wave is ignited. This wave induces cooling in the mid-troposphere which destabilizes the atmosphere and primes it for convection. They argued that the inability of models to accurately represent the diurnal cycle could be due to an inability to capture gravity waves in lower resolution models or convective parameterizations. Similar results were presented by Hassim et al. (2016) for the island of New Guinea. While they found that convection propagates offshore too slowly to be directly coupled to the gravity wave, they hypothesized that the gravity wave destabilizes the atmosphere offshore and increases the convective available potential energy (CAPE) before convection arrives.

Much of the body of work on the diurnal cycle near the MC has focused on the boreal winter season, and on the largest islands near the equator. However, during the boreal summer season, the background monsoon state shifts much of the convection away from the equator, towards the Indian subcontinent, southeast Asia, the South China Sea (SCS), and the Philippines (Biasutti et al. 2012). This thesis will explore this part of the world in an effort to show how off-equatorial land-masses in boreal summer fit in with the established theory of the MC diurnal cycle.

1.3 The Madden-Julian Oscillation

1.3.1 Discovery and Early Work

In addition to small scale features largely on the mesoscale like the diurnal cycle, there has also been considerable interest in large-scale disturbances in the tropics. Matsuno (1966) developed a theory for waves in the equatorial atmosphere based on a shallow water system of equations. However, in the early 1970s, two scientists found something that didn't quite fit. Madden and Julian (1971) stumbled upon a statistically significant oscillatory pattern in zonal wind and pressure at Canton Island in the equatorial pacific with a period of 40-50 days. They had no reason to suspect the existence of such a phenomena, as it didn't fit in with established equatorial wave theory (Wheeler and Kiladis 1999). In their 1972 follow-up, Madden and Julian elaborated further on this novel discovery, describing the existence of a global-scale oscillation in winds and surface pressure with a 40-50 day period, which would later be dubbed the Madden-Julian Oscillation (MJO) after its discoverers.

The MJO is an area of enhanced convection concentrated over the Indo-Pacific warm pool that propagates slowly eastward with a phase speed of about 5 ms^{-1} (Madden and Julian 1994). Anomalous convection is associated with anomalous divergence (convergence) in the upper (lower) troposphere, which drives an out-of-phase relationship between zonal winds in the upper and lower troposphere (Madden and Julian 1971). This pattern is mirrored by a correspondent suppressed convection anomaly associated with circulation anomalies of the opposite sign. Taken together, the suppressed and enhanced convective anomalies appear as a zonal wavenumber 2 pattern over the warm pool (Hendon and Liebmann 1994). Hendon and Salby (1994) used observations and reanalysis to show close correlations between outgoing longwave radiation (OLR), temperature, vertical velocity, and surface convergence. Knutson and Weickmann (1987) found that while anomalies in convection propagate only over the warm SSTs of the Indo-Pacific warm pool, the circulation cells tracked through upper-tropospheric velocity potential (a measure of large-scale divergence), circumnavigate the globe at a much faster speed than when they are coupled to convection. While the convective anomaly is confined to the tropics (Madden and Julian 1972), the MJO has impacts globally via forcing of a wave train into the winter hemisphere (Knutson and Weickmann 1987, Matthews et al. 2004).

Gill (1980) used an idealized model to show that an anomalous heating source along the equator creates equatorially trapped waves that correspond to Matsuno's (1966) shallow water theory. He proposed broad latent heating associated with enhanced convection on the equator forces an eastward propagating Kelvin wave on the eastern front, and Rossby gyres manifest as low-level cyclonic anomalies and upper-level anti-cyclonic anomalies, on the western front. These results are summarized in Gill's Figure 1, which is included here as Figure 1.1. In this figure, the heating anomaly is centered at 0 in the x-direction. Strong vertical motion is indicated centered on the heating anomaly, with weak subsidence on the western flank behind the Rossby gyres. Low level winds are predominantly easterly to the east, associated with the Kelvin wave response. To the west, cyclonic wind anomalies appear. While not shown here, anti-cyclonic circulation anomalies in the upper troposphere are also forced on the western side of heating in both hemispheres. Knutson and Weickmann (1987) used observations to argue that these circulation anomalies are present off the equator in both hemispheres but are stronger in the winter hemisphere. In addition, circulation anomalies of the opposite sign to those in Figure 1.1 are forced by the MJO suppressed convection. These Rossby gyres can help initiate wave-trains that travel primarily into the winter hemisphere, modulating surface weather in the mid- and high-latitudes (Hendon and Salby 1994, Matthews et al. 2004). These authors collectively contributed a significant body of knowledge of the MJO to the community, but underlying questions regarding MJO dynamics remain. A few ground-breaking field programs that established a firmer understanding of the structure and character of the MJO are discussed next. Then, theory that attempts to explain what the MJO is, why it exists, and why it looks the way it does will be reviewed with a focus on moisture mode theory. Finally, this chapter will section will conclude with an overview of the boreal summer-time behavior of the MJO.

1.3.2 Field Observations and the Convective Cloud Population of the MJO

In addition to contributing immensely to the understanding of the oceanic diurnal cycle, the The Tropical Ocean Global Atmosphere Coupled Ocean-Atmosphere Response Experiment (TOGA COARE) field campaign was one of the first to extensively document intra-seasonal variability related to the MJO. While not designed as an MJO experiment, researchers found that the MJO was fundamental in modulating the precipitation patterns observed. Lin and R. Johnson (1996) found a that a gradual buildup in tropospheric moisture was observed before an MJO event, and a rapid drying the lower troposphere occurred near the end of the event as strong westerlies took over. Chen and Houze (1997) showed using TOGA COARE observations that the MJO suppressed period consisted of short-lived, small, and shallow convective systems that peak in the afternoon and decay overnight. Alternatively, the MJO active phase brings favors upscale development into MCSs overnight, leading to a morning maximum in precipitation.

Sui et al. (1997) took a different approach, but also concluded that diurnal warm layers in the ocean during the suppressed period help to drive an afternoon convective maximum. For the enhanced phase, they argued that precipitable water is more available, which allows for growth overnight, and the observed morning maximum. R. Johnson et al. (1999) made a novel finding, that contrary to conventional wisdom, the distribution of the cloud population in the tropical oceans is trimodal, with shallow cumulus, cumulus congestus, and deep convective clouds. The cloud tops in these modes are typically found near the trade wind inversion, 0C stable layer, and the tropopause, respectively. The authors argued that the previously overlooked cumulus congestus clouds are actually very important for the development of the MJO, via the moistening of the mid-troposphere caused by detrainment.

A more recent major field campaign was specifically designed to target the MJO. The Cooperative Indian Ocean Experiment on Intraseasonal Variability in the Year 2011 (CINDY)/Dynamics of the MJO (DYNAMO) field campaign took place in the central Indian Ocean in the boreal autumn and winter season of 2011-2012. Observations were collected for three strong MJO events, one in each of the last three months of the 2011 calendar year. These three events became the subject of extensive research in the seven years since. R. Johnson and Ciesielski (2013) found that the active MJO convective envelope of the October 2011 event largely consisted of westward propagating disturbances with a period of two days, while the November 2011 was dominated by two Kelvin waves. Soundings taken in the region showed a gradual moistening of the low- to mid-troposphere in the approximately two weeks leading up to each event. Other studies have supporting this finding using satellite estimates of column water vapor, as well as reanalysis (e.g. Myers and Waliser 2003, Kiladis et al. 2005). Sobel at al. (2014) used reanalysis data from these events to argue that this moistening was driven by horizontal advection across the mean moisture gradient by the MJO winds, which also assists in the drying process after peak precipitation. These findings were corroborated by Ruppert and R. Johnson (2015) and Tseng et al. (2015), who also indicated the importance of vertical advection in driving these events. Moistening processes will be a focus of the next subsection.

DYNAMO also inspired work on exploring the convective cloud population of the MJO and transition from suppressed to active MJO state. Addressing the dynamics side of the make-up of the DYNAMO MJO events, Zuluaga and Houze (2013) proposed that the active phase of the MJO was largely dominated by westward propagating inertia-gravity waves, lasting 2-4 days. Kikuchi et al. (2018) explored the wide variety of convectively coupled equatorial waves found during the DYNAMO events in order to establish a general structure common to all events. They advocated for the existence of a hierarchy of convective structures making up the MJO. The DYNAMO events largely consisted of eastward propagating convectively coupled Kelvin waves, each composed of westward propagating cloud clusters, some of which could be classified as westward inertia-gravity waves.

A series of studies used radar observations to explore the synoptic and mesoscale features present in the MJO envelope. Zuluaga and Houze (2013) composited short periods of active rainfall within the MJO to learn that shallow convective cores peak before the rainfall maximum, followed by deep convective cores, and wide convective cores during peak rainfall. Afterwards, broad stratiform regions became more prevalent. Xu and Rutledge (2014) composited several events in the DYNAMO period to show that the pre-onset period is characterized by high CAPE, moist low-levels, dry mid- to upper-levels, and reduced wind shear, which promotes isolated, shallow convection. Over a period of two weeks, shallow convection moistens the mid-troposphere, which allows for deep convection, which then moistens the upper-troposphere. When upper-tropospheric moisture is maximized, there is a tendency towards MCSs and stratiform rainfall.

Powell and Houze (2013, 2015) concluded using shipborne and spaceborne radars that the congestus mode helps drive the transition from the suppressed to active MJO state in about 3-7 days. Increasing convective activity creates a positive feedback since intersecting cold pools further invigorate convection (Feng et al. 2015, Rowe and Houze 2015). Thorough analysis of data collected during these important field campaigns have more conclusively demonstrated that isolated, shallow convection driven by diurnal warm layers in the sea-surface dominates the inactive MJO period, while the active period is characterized by deep convection, broad stratiform precipitation, and MCSs. Dias et al. (2013) found that there is considerable variability in the convective organization of the MJO from event to event. Furthermore, while variance of higher frequency waves increases in the MJO active period, they do not change character. (Dias et al. 2017). In other words, the exact level of organization of smaller-scale phenomena is not critical for MJO dynamics. However, the general signal of moistening pre-onset, and the preference for different modes of convection in the active phase, was observed in numerous longer climatological studies as well (Barnes and Houze 2013, Yuan and Houze 2013). While the exact make-up may not be important, small-scale features in general have implications for MJO propagation, which will be discussed in the next subsection.

1.3.3 Moisture Mode Theory for MJO Propagation

Madden and Julian (1971, 1972) noted that the MJO exhibits slow, eastward propagation. Many theories have been proposed to explain the maintenance and propagation of the MJO over the years, both as a dry wave, and one where moisture is required. D. Yang and Ingersoll (2011, 2013) attempted to explain the MJO as Mixed-Rossby Gravity wave packet, propagating with the eastward group velocity of these waves, or as an interference pattern between westward and eastward propagating intertia-gravity waves. Other studies have tried to explain the MJO with only dry dynamics (Majda and Stechmann 2009, Hayashi and Itoh 2017), but without moisture these models are often unable to fully explain the observed patterns. In this section, the body of literature that has led to a more complete understanding of the MJO as a moisture mode will be discussed, i.e. a feature in which moisture is required for its existence and propagation under assumptions of a weak temperature gradient.

Maloney and Hartmann (1998) presented a novel look at the structure and life-cycle of the MJO leading up to moisture mode theory, finding that 1000-hPa moisture convergence is well correlated with water vapor, while 850-hPa convergence lags slightly. Examining this in the context of a coupled Kelvin-Rossby wave, they demonstrate that, in congruence with theory, the pressure minimum where surface convergence is expected is located under the 850-hPa easterlies associated with the leading Kelvin wave. The authors conclude that frictional moisture convergence in the boundary layer assists in moistening the troposphere to the east of convection. Conversely, subsidence and horizontal advection of dry air on the west side of enhance convection associated with the trailing off-equatorial Rossby waves, likely contributes to drying the atmosphere. Matthews (2000) took these ideas a step further and argued that moistening to the east and drying to the west helps drive the eastward propagation of the MJO. Furthermore, they introduced evidence of a globally circumnavigating eastward propagating Kelvin wave initiated by MJO convection decaying in the West Pacific reaches the Indian Ocean in time to coincide with the development of the next event. While a unifying theory remained elusive at the time of these studies, they helped to establish the importance of asymmetric moisture anomalies in determining MJO propagation.

Modeling studies led by Raymond introduced new ideas that solidified a base for the moisture mode theory. Raymond (2000) showed that the saturation deficit helps drive rainfall. In particular, convection and tropospheric water vapor were shown to be closely coupled in both models (Raymond 2000) and observations (Bretherton et al. 2004). In a 2001 followup study, Raymond argued that the tropics are unstable to large-scale vertical displacement. In other words, high-clouds associated with deep convection depress OLR relative to the surroundings, creating a heating anomaly which further promotes lifting and precipitation (Kim et al. 2015). The author also argued that the MJO may be a non-dispersive wave with zero group velocity that is destabilized by the feedback mechanism described above. This model is the first to represent something resembling a moisture mode. Later, Raymond and Fuchs (2009) were able to produce a realistic MJO in an aquaplanet model where precipitation increases with saturation fraction, which further increases the saturation fraction. This was dubbed moisture mode instability, which essentially concludes that the MJO is tightly coupled to total column water vapor.

In two ground-breaking studies, Sobel and Maloney (2012, 2013) developed a simple idealized one-dimensional model to hypothesize that the MJO is a moisture mode. They showed that they can build an MJO-like disturbance using only a single prognostic equation for anomalous column water vapor, which is equivalent to moist static energy under the weak temperature gradient approximation (Sobel et al. 2001). While they were able to extract a linear wave equation for the MJO, the model was unable to replicate its eastward propagation. Next, they modified their model to correct its flaws (Sobel and Maloney 2013). While still retaining a single prognostic equation for column water vapor, this follow up added parameterizations for synoptic scale eddies, horizontal eddies, and frictional convergence, which favor eastward propagation by influencing the moisture budget. Here, they concluded that moisture modes can propagate eastward, as with the MJO, when these processes that promote moistening in the MJO easterly anomalies outweigh drying resulting from the suppression of surface fluxes on the west side of convection. Adames and Kim (2016) were able to further develop this theory in a two-dimensional model, arguing that the MJO was in fact a dispersive wave with westward group velocity, in which new centers of convection develop slightly west of previous ones. In other words, while the main MJO envelope propagates eastward with a phase speed of about 5 ms^{-1}, successive MJO events develop slightly west of the preceding event, corresponding to a westward transport of energy. Jiang et al. (2018) showed with reanalysis data that moisture mode theory can also explain the boreal summer mode, elaborated upon in the next section. Next, some of the mechanics of moisture mode theory will be explored, describing how, in the real world, the MJO propagates.

Through a budget analysis of the MJO moist static energy (MSE) Maloney (2009) found that in a climate model, the increase of MSE prior to MJO onset is primarily driven by horizontal advection of MSE compensating for the latent heat flux anomalies promoting drying. Hsu and Li (2012) used reanalysis to propose that moisture increases ahead of MJO convection are primarily driven by moisture convergence caused by the leading Kelvin wave, similar to Maloney and Hartmann (1998). Specifically, advection across the mean moisture gradient by the MJO winds contributes about 80% of this horizontal convergence. Sobel et al. (2014) found something similar, that horizontal moisture advection is the primary factor causing moistening east of convection and drying west of convection, while radiative anomalies maintain convection. Horizontal advection of moisture to the east becomes less negative ahead of convection, providing a relative source of moistening. These findings were supported by other observational and modeling studies (Zhu and Hendon 2015, Tseng et al. 2015, Powell and Houze 2015). Ruppert and R. Johnson (2015) conclusively showed that local processes alone are insufficient to explain the observed moistening, and advection must be included. During the latter part of the suppressed period, drying processes due to large-scale subsidence and horizontal advection begin to weaken. Vertical advection transports moisture higher in the atmosphere, due to the pressure trough associated with the Kelvin wave east of the enhanced convection. The importance of horizontal moisture advection in determining MJO propagation led many researchers to wonder if this can be used to predict whether or not the MJO will propagate.

Not all MJO events are created equal, and some decay in the Indian Ocean, while others successfully propagate through the MC (Jones et al. 2004). Kim et al. (2014) articulated that the presence and strength of the west Pacific dry anomaly is critical to determining if the MJO will successfully propagate over the MC. Suppressed convection produces a Rossby wave circulation response on its westward tail (Gill 1980), which promotes favorable horizontal moisture advection into the free troposphere in the region east of the enhanced convection centered in the Indian Ocean. Other terms of the MSE budget are in phase with the heating anomaly, indicating that they act to amplify or decay the disturbance, whereas horizontal advection moves it. Specifically, it is the meridional advection related to the Rossby wave response to suppressed convection that assists in priming the MC free troposphere for convection, and successful MJO propagation. Additionally, models tend to be more skillful in their MJO forecasts when a dipole pattern is present with suppressed western Pacific convection (Kim et al. 2016).

The literature discussed in this section portrays a convincing case for the idea that the MJO is a moisture mode instability that depends strongly on the horizontal advection of moisture into the region to the east, and the vertical advection of this moisture higher in the troposphere by convection. Some studies (Peatman et al. 2014) have suggested that similar processes (e.g. horizontal moisture convergence and vertical advection) to those that promote MJO propagation in the moisture mode paradigm also drive MJO modulation of the diurnal cycle over MC islands. This study aims to clarify a few of those hypothesis by analyzing the boreal summer season. Next, some differences in this pattern present in boreal summer will be identified, before exploring how this theory interacts with the diurnal cycle.

1.3.4 The Boreal Summer Intraseasonal Oscillation (BSISO)

Most of the literature presented so far focuses primarily on the winter season. However, the boreal summer mode of the MJO, known as the Boreal Summer Intraseasonal Oscillation (BSISO) is also critical to understand, both in developing a consistent theory, and understanding its global impacts. The top panel of Figure 1.2 shows the variance in interpolated outgoing longwave radiation (OLR; Liebmann and Smith 1996) filtered to include only intraseasonal timescales (20-100 days) in November-April as a percent of the total November-April variance. The bottom panel shows the same thing, but for May-October. The dataset and methods are described in section 3.1. This figure summarizes the importance of intraseasonal variability in each season, showing that for much of the northern hemisphere tropics, intraseasonal variability is even more important in boreal summer compared to boreal winter. In particular, about 20-30% of the boreal summer OLR variance occurs within the 20-100 day band over the South China and Philippine Seas, comparable to the numbers in the frequently studied boreal winter Indian Ocean and MC. In this study, I will use the term MJO to refer to the winter time mode, BSISO to refer to the summer time mode, and simply intraseasonal oscillation (ISO) to refer to both modes taken together. In addition to capturing a significant portion of the local variability in convection, the BSISO modulates the Asian summer monsoon (Lau and Chan 1986, Sengupta et al. 2001, Zhou and Chan 2005), tropical cyclones across the world (Maloney and Hartmann 2001, Sobel and Maloney 2000, Maloney and Dickinson 2003), other modes of tropical waves (Straub and Kiladis 2003), and remote heat waves (Hsu et al. 2017).

Lau and Chan (1986) pioneered new work on the boreal summer mode, showing that while eastward propagation directly along the equator is the norm in the boreal winter time, meridional propagation is evident when the MJO interacts with the monsoon system. In boreal summer, convection still initiates in the Indian ocean, but then develops into an elongated band stretching from northwest to southeast. Convection then slowly moves to the northeast, into the Bay of Bengal and South China Sea. In this season, heating is no longer symmetric about the equator. Thus, the forced Kelvin-Rossby response is also highly asymmetric (Gill 1980, Hendon and Liebmann 1994, Kemball-Cook and B. Wang 2001). Figure 3 from Gill (1980), reprinted as Figure 1.3 here shows the wind and pressure response to an idealized heat source centered off of the equator, analogous to the BSISO. Notice that the Rossby-gyre in the winter hemisphere (Southern Hemisphere in this example) is weakened and replaced with an anti-cyclonic anomaly, while its summer-hemisphere counterpart is strengthened. This pattern has been observed in association with the BSISO in observations and reanalysis (Kemball-Cook and B. Wang 2001, Lawrence and Webster 2002). Furthermore, Lawrence and Webster (2002) noted that northward and eastward propagation occur in concert with one another in nearly 80% of the BSISO events they examined, leading to questions on the potential similarities between mechanisms driving propagation in each direction.

Several mechanisms have been proposed in an attempt to explain this observed northward propagation of the ISO in boreal summer. Sengupta et al. (2001) and Kemball-Cook and B. Wang (2001) pointed to the importance of air-sea interactions and surface fluxes in promoting northward propagation. Others (Hsu et al. 2004, Jiang et al. 2004) have showed that moisture advection in the boundary layer and lower free troposphere consistently leads the convective anomaly to the north. DeMott et al. (2013) used both reanalysis and a model to show that boundary layer moisture advection is critical to northward propagation, while SST-related mechanisms are relevant, but of secondary importance. Jiang et al. (2018) presented novel work on the BSISO, arguing that it fits in well with the moisture mode paradigm, and horizontal advection of mean moisture by the MJO winds assists in propagating the disturbance northward in the summer, in addition to eastward year round. Overall though, there has been comparatively little work done focusing on the BSISO mode compared to the boreal winter MJO. Now, there is more of a recognition in the field that understanding the ISO as a whole must come with a clear theory that works for all seasons.

1.3.5 BSISO Indices

Statistical indices are a convenient way of succinctly summarizing the lifecycle of the ISO. In this section, a few attempts from recent years to create an ISO index are discussed. The most widely used MJO index is the Real-time Multivariate MJO (RMM) index, developed by Wheeler and Hendon (2004). This index is based on the first two leading combined empirical orthogonal functions (EOFs) of 850-hPa zonal wind, 200-hPa zonal wind, and satellite-derived OLR estimates, averaged near the equator. RMM has the obvious advantage of being useful in real time, and thus more relevant for prediction and analysis of current patterns. However, since RMM is based on an fields averaged from 15°S - 15°N, it misses much of the variance outside of this latitude band. Figure 1.4 shows the fractional variance explained by each of the four BSISO indices discussed in this section, calculated by correlating each of the two PC's that define each index with OLR or precipitation at each grid point, and then adding the variance explained by each PC together to get total variance explained by the index. This was done for 1998-2017 for CMORPH, and 1979-2017 for AVHRR OLR, during May-October only. The variance explained by RMM is located in the top right panel of both (a) and (b). Near the equator, RMM captures around 10-15% of the total boreal summer variance in daily mean OLR, and about 5-8% in precipitation. However, it is evident that variance explained drops off quickly poleward of 15°N. Interestingly, composites of OLR or wind based on the RMM index in only boreal summer still look qualitatively similar to composites based on indices specifically design for the boreal summer season (Wheeler and Hendon 2004).

Another major index considered was developed by Kikuchi et al. (2012), and is referred to as the bimodal ISO index in this thesis. This index was designed to capture the propagation of the ISO by using an extended EOF (EEOF) analysis which time-lagged information into the analysis. As a result, the index is skillful in capturing only propagating ISO, not just events that may appear to resemble the EOF but are not the ISO. Furthermore, the bimodal ISO index is based on bandpass filtered OLR, and has two distinct modes based on EEOF analysis from the two solstice seasons (December-February and June-August). These two modes give the index its bimodal nature, with the traditional MJO mode peaking in the boreal winter season, and the BSISO mode peaking in the summer. Variance explained in May-October by just the BSISO mode is shown in the bottom left panels of Figure 1.4(a) and (b). Somewhat surprisingly, this index does not explain much of the variance in OLR, even though it was derived from the same OLR dataset used here. This could be a facet of how variance explained was calculated, as time lag information was not incorporated in this analysis. However, this index still captures about 3-6% of variance in precipitation. Its nature as a smoothed index probably results in explaining less of the variance in real-time variables without any filtering, but it likely captures propagating ISO events better than its real-time counterparts (S. Wang et al. 2018). Had variance explained been calculated as percent of total *intraseasonal* variance explained by the index, this index would likely perform dramatically better.

Next, the BSISO index derived by Lee et al. in 2013 is considered. This index was designed as a direct boreal summer counterpart to RMM, aiming to better capture the variability in the SCS, northern Indian Ocean, and western Pacific away from the equator. The BSISO index here is based on multi-variate EOF analysis of OLR and 850-hPa zonal wind anomalies from May-October only in the Asian monsoon region. By its nature, this index is expected to capture the most variance in daily mean OLR, since that is part of what the EOF is based on. As seen in Figure 1.4, this is indeed the case. Lee's BSISO index is best able to capture the variance around the Philippines, the primary area of interest in this study, for both OLR and precipitation, maximizing in the SCS at around 15-20% of the variance in OLR, and 5-10% of the variance in daily mean precipitation. However, S. Wang et al. (2018) showed that time-lagged reconstructions based on this index do not capture the northward propagation of the BSISO. In other words, an active signal in the Lee et al. (2013) index may not always correspond to a propagating BSISO event. The index is prone to include spurious signals that simply project onto the EOF patterns, but do not move northeastward in time.

The final BSISO index discussed in this thesis is the OLR-based MJO Index (OMI) developed by Kiladis et al. (2014). The OMI takes a unique approach by calculating separate EOFs for a 121-day period centered at every calendar day in the year from bandpass filtered OLR. While many previous indices have incorporated zonal wind anomalies into the EOF calculation due to their tendency to be less noisy compared to OLR, the authors show that using bandpass-filtered OLR avoids the introduction of significant noise. Since OMI accounts for the seasonal variation by calculating separate EOFs for each day of the year, it is useful in all seasons. Additionally, the use of a bandpass filter in the calculation of the EOF patterns assists this index in better representing the northward propagation in time, as it is forced to respond to signals only that occur on 20-96 day timescales (S. Wang et al. 2018).

So far, this thesis has reviewed the body of literature covering the diurnal cycle of precipitation in the tropics, as well as the ISO and its seasonality. Next, prior studies focusing on the interaction between the diurnal cycle and the ISO will be discussed, before motivating the original work discussed in later chapters of this thesis.

1.4 Scale Interactions

1.4.1 Impact of the MJO on the diurnal cycle

The diurnal cycle of convection over the Maritime Continent, a small-scale phenomenon, has been thoroughly described along with the Madden-Julian Oscillation, a global-scale phenomenon that acts on intra-seasonal time scales. However, the question of how these two features interact has yet to be addressed. Returning to the analogy introduced in Section 1.1, two stones of different sizes are now dropped into the lake repeatedly. A single large boulder falls into the lake, creating huge waves across the water surface. In addition, many small stones are dropped into this pattern in regular succession, imposing another set of ripples. How do these ripples interact? In the real world, this question is much more challenging to answer, as not only to the ripples of the MJO and the diurnal cycle interfere, but each affects the very existence of the other. After going through the literature on this subject, it will become clear that this question has not yet been answered satisfactorily.

Sui and Lau (1992) were one of the first to pose the question of how the MJO interacts with smaller-scale, higher-frequency phenomena. They found that while the MJO active period favors 2-4 day disturbances, the MC diurnal cycle tends to actually be suppressed. Similarly, the diurnal cycle is maximized when the large-scale MJO suppressed conditions are overhead. Over open ocean, the diurnal cycle tends to favor the secondary afternoon maximum in shallow convection during the MJO suppressed period, while MCS development leading to a pronounced morning precipitation maximum are favored in the active phase (Chen and Houze 1997, R. Johnson et al. 1999, Xu and Rutledge 2014, Rowe and Houze 2015, Ruppert and R. Johnson 2015, Sakaeda et al. 2018). Xu and Rutledge (2018) found that deep convective activity and lightning associated with an enhanced diurnal cycle over the Philippines and Southeast Asia also peaks before the main convective anomaly arrives.

The interactions between the MJO and the diurnal cycle over land and coastal waters is a more compelling problem. Many studies over the past several decades have explored the relative contributions of MJO winds, insolation, and equatorial wave dynamics in altering the diurnal cycle. Sumatra and New Guinea are fairly similar in geography, characterized by a spine of mountains near the center of the island parallel to the coasts. Several studies have found that the MJO modulates not only the diurnal cycle over land, but also its propagation out to sea. Rainfall, likely related to an amplified diurnal cycle, over New Guinea leads the large-scale convective maximum by about one quarter of a cycle (Matthews et al. 2013). This island also exhibits marked changes in offshore propagation of diurnally initiated convection as a function of MJO phase. During the suppressed period when easterly winds dominate, convection generally propagates offshore overnight to the southwest side of New Guinea, or leeward. However, under the westerly regime, convection initiated by the diurnal cycle propagates in both directions after initiating over the high topography, although southwesterly propagation is less smooth (Ichiwaka and Yasunari 2008). Furthermore, Vincent and Lane (2016) learned that offshore propagation is most pronounced in the lead up to the active phase of the MJO, with convection moving slowly offshore for about 100-200-km, followed by a rapid propagation associated with diurnally generated gravity waves, similar to the proposed mechanism of Love et al. (2011).

Sumatra is perhaps the most heavily studied island of the MC. Fujita et al. (2011) used a collection of datasets and models from various sources to show that the diurnal cycle is most active when weak westerlies are present, or just before the large-scale convection arrives. Similar to New Guinea, convection propagates exclusively westward when the MJO background flow is easterly, and in both directions when the lower-tropospheric flow is westerly (Sakurai et al. 2005, Yanase et al. 2017). Oh et al. (2012) argued that the decline in the diurnal cycle after MJO onset is partially related to the prevailing westerlies disrupting the convergence related to the sea-breeze circulation. These results have been supported by other studies (Birch et al. 2016). Leeward propagating storminess and a diurnal cycle peak before MJO onset was also found for Borneo (Ichiwaka and Yasunari 2006, Kanamori et al. 2013). These results are also corroborated by studies taking a more general look at the entire MC (Rauniyar and Walsh 2011, Sakaeda et al. 2017). The early peak in the diurnal cycle often determines an early peak in total precipitation over land (Peatman et al. 2014), and is robust enough that an index for the MJO can even be developed based on the ratio of oceanic to land-based convection (Vincent et al. 2016).

One of the more comprehensive looks at the impact of the MJO on the diurnal cycle was done by Peatman et al. (2014). They found that not only does the diurnal cycle over land peak about 1/8 of a cycle before the arrival of the main convective envelope, but also that the diurnal cycle drives daily mean precipitation over land such that a similar signal is visible in that field. Also of interest, they showed that infrared brightness temperatures are not a good proxy for convection over islands, while they still perform skillfully over the open ocean. The authors hypothesized that the early peak of the diurnal cycle was due to the elevated insolation indicative of the suppressed MJO period combining with frictional moisture convergence associated with the leading Kelvin wave, and the Rossby circulation trailing the suppressed convection. Moisture convergence explains why the diurnal cycle peaks before onset, and not after. This hypothesis was supported by subsequent modeling work (Birch et al. 2016). All of these major papers on the impact of the ISO on the diurnal cycle, except for a few, focus primarily or entirely on the boreal winter season, and on the large islands near the Equator. The impact of the boreal summer mode on the diurnal cycle remains an open question, particularly off the equator, where the influence of equatorial wave dynamics is reduced. Furthermore, a consistent hypothesis explaining the modulation of diurnal propagation by the MJO has not yet been reached.

1.4.2 Feedback to MJO propagation

While downscale relationships are fairly simple to determine from observations, establishing upscale connections is not so easy. Still, several studies have attempted to address the question of how the diurnal cycle can influence the propagation and maintenance of the MJO. Inclusion of the diurnal cycle dramatically improves the representation of the MJO in a general circulation model (Slingo et al. 2003, Bernie et al. 2008), indicating that understanding this interaction could be important for an understanding of the MJO. There is also evidence that the diurnal cycle can precondition the atmosphere for MJO propagation, and modulate it through diurnally generated gravity waves (Raupp and Silva Dias 2009, Majda and Q. Yang 2016). Hagos et al. (2016) found that representation of the diurnal cycle in a model actually reduces the ability of the MJO to propagate across the Maritime Continent. They proposed that this is because the diurnal cycle initiates convection at nearly the same time across a huge spatial area, covering the entire Maritime Continent, which disrupts the smooth, eastward propagation of the MJO. Diurnally initiated convection competes with the oceanic convection through land-sea breezes and moisture supply.

However, many studies have shown that the diurnal cycle over open ocean is important for moistening the troposphere prior to an ISO event. Cumulus congestus clouds peaking in the afternoon driven by the diurnal warm layer in the sea surface can advect moisture vertically into the free troposphere when under the influence of the suppressed ISO phase (R. Johnson et al. 1999). Furthermore, mid-tropospheric moistening might be inhibited in the absence of a diurnal cycle, indicating the existence of a non-linear contribution of diurnal moistening (Ruppert and R. Johnson 2015, 2016). These studies, while compelling, do not provide a conclusive answer on how the diurnal cycle, particularly over MC islands, feeds back onto the MJO.

1.5 Motivation

While it is tempting to say that once models reach sufficiently high resolution, all of these issues will go away, this is not the case. Increasing resolution alone cannot take the place of improving parameterizations (S. Johnson et al. 2016). As discussed in the prior sections, much of the work in the field has focused on the boreal winter MJO, and the diurnal cycle over large, equatorial islands. But the MC is larger than Sumatra, Borneo, and New Guinea, and different features become dominant when interaction with the monsoon is considered. Fully understanding and simulating the diurnal cycle improves the understanding of the MJO, and vice versa (Slingo et al. 2003, Bernie et al. 2008, Hagos et al. 2016). Thus, the boreal summer season and off equatorial portions of the MC cannot be neglected.

Transitioning the focus from the equator to the Philippines and the South China Sea, the following questions still remain. What does the diurnal cycle look like in a different region with unique geography? Does the diurnal cycle propagate offshore into the South China or Philippine Seas via the same mechanisms observed near the equator? Are these results dependent on the dataset used? Questions also remain regarding the impact of the BSISO on the precipitation in this part of the world. Does the pattern of a diurnal cycle peak prior to MJO onset observed by Peatman et al. (2014) still appear far from the equator? Do these results depend on the selection of index and compositing method? Are the mechanisms proposed by previous papers adequate to explain observations in a new part of the world or is an expanded theory needed? Can the diurnal cycle in the Asian monsoon region impact BSISO propagation in the same way that the diurnal cycle over the near-equatorial islands impacts MJO propagation? This thesis will address all but the last question, which will be motivation for future work.

The following hypothesis is proposed to address the above questions. It is expected that the mean state of the diurnal cycle will look quite similar to regions previously discussed, particularly over the larger islands of the Philippines. Additionally, even though the Philippines are largely outside of the influence of the equatorially trapped Kelvin wave and thus its leading frictional moisture convergence, the forced off-equatorial Rossby wave still promotes a diurnal cycle that leads the main BSISO envelope. Instead of frictional convergence, it is likely that wind patterns in the boundary layer coupled with lower free-tropospheric moisture promote the early signal in the diurnal cycle. Additionally, this pattern is independent of the index used. It is also suggested that the diurnal cycle, particularly its offshore propagation, in the Philippines and Bay of Bengal could assist in preconditioning the atmosphere for poleward propagation of the main BSISO convection, but testing this hypothesis is left for successive studies.

1.6 Outline

In this chapter, the current state of the field and the body of literature relating to the diurnal cycle of convection in the Maritime Continent, the Madden-Julian Oscillation, and the interactions between the two have been described. In Chapter 2, the mean-state diurnal cycle in detail over the Philippines and South China Sea will be discussed, with a focus on the northernmost island of Luzon to answer the first few questions posed in the previous section. In Chapter 3, the influence of the BSISO on the diurnal cycle in this region will be analyzed, in an attempt to test the applicability of the Peatman et al. (2014) results and hypothesis to a different season and part of the world. In Chapter 4, evidence will be presented for a few proposed mechanisms that explain the results in Chapter 3, before summarizing findings, presenting some important conclusions, and motivating future work in Chapter 5.

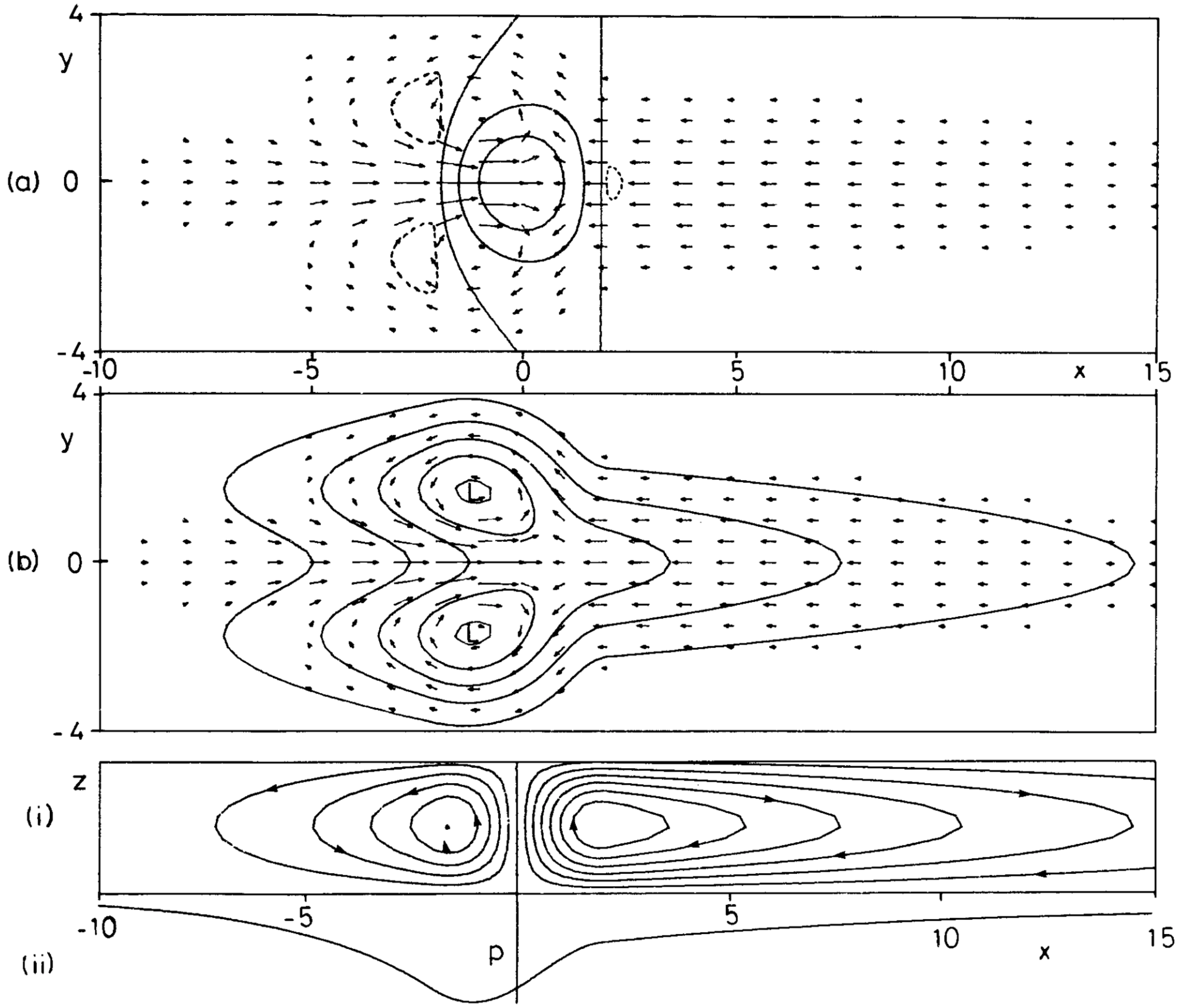

Figure 1.1: Figure 1 from Gill (1980), showing the solution to an idealized heating anomaly symmetric about the equator. (a) shows vertical velocity in contours, at -0.1, 0, 0.3, and 0.6 ms^{-1} with positive in solid contours superimposed on the velocity field for the lower layer of the model. (b) shows contours of perturbation pressure (at intervals of 0.3-hPa), all negative. (c) shows meridionally integrated flow in the xz plane in (i) and perturbation pressure in (ii).

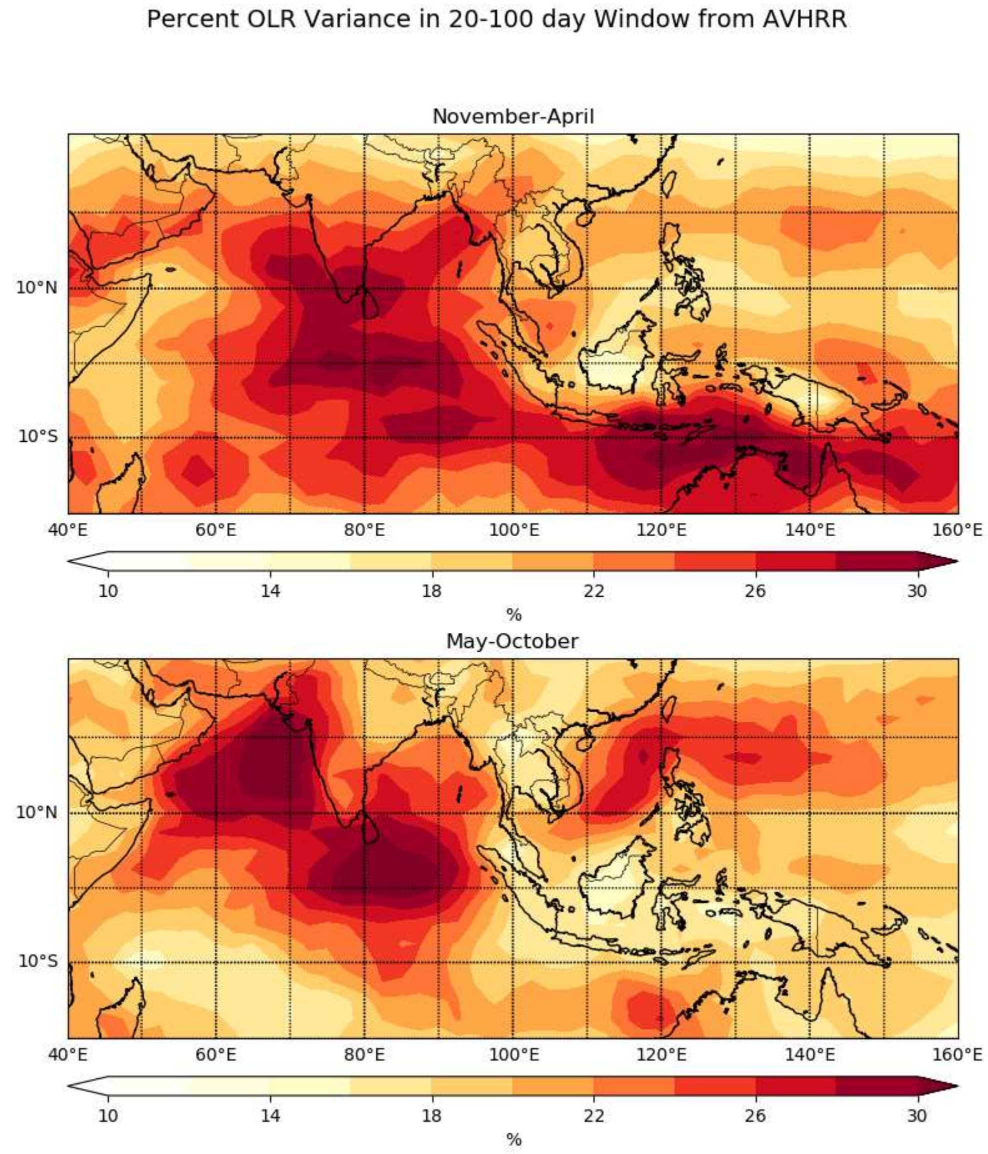

Figure 1.2: Percent of AVHRR OLR variance in 20-100 day band in May-October (top) and November-April (bottom)

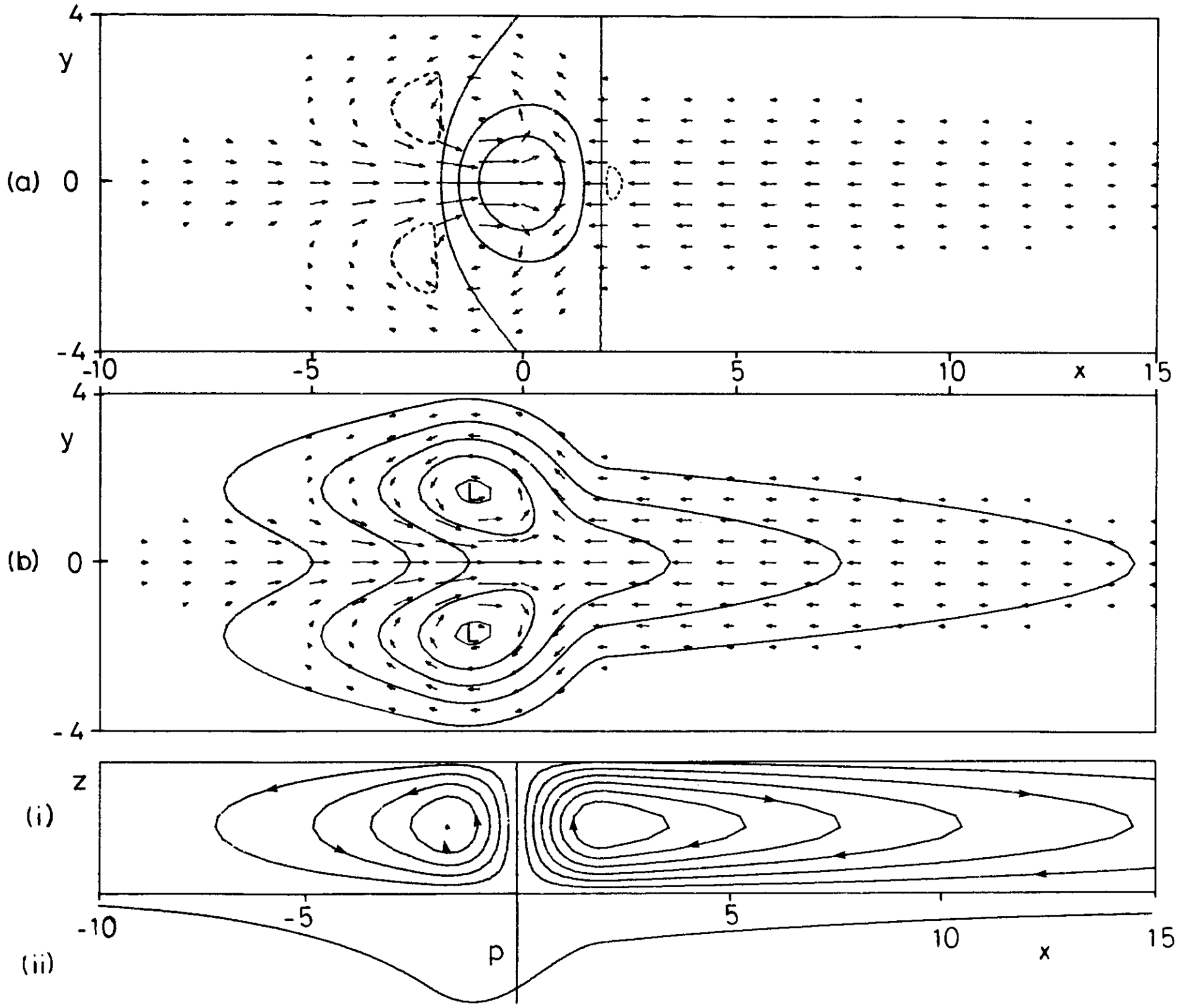

Figure 1.3: Figure 3 from Gill (1980), showing the solution to an idealized heating anomaly symmetric about the equator. (a) shows vertical velocity in contours, at intervals of 0.3 ms^{-1} superimposed on the velocity field for the lower layer of the model. (b) shows contours of perturbation pressure (at intervals of 0.3-hPa), all negative.

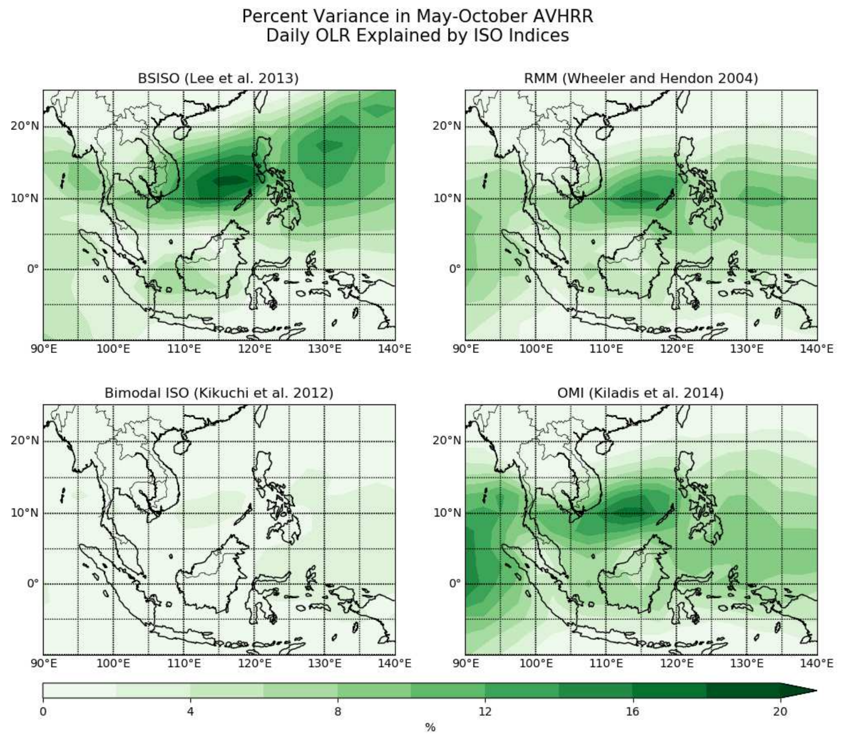

(a) AVHRR OLR

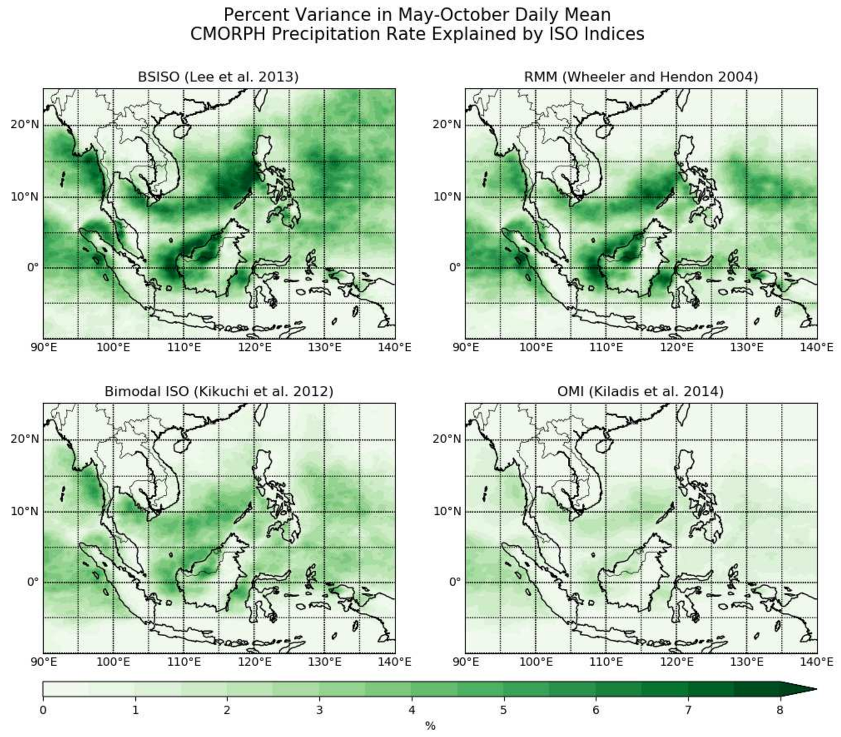

(b) CMORPH Precipitation

Figure 1.4: The fractional variance explained in AVHRR OLR (a), and CMORPH precipitation (b) during May-October by each of the ISO indices discussed in this thesis.

Chapter 2

The Average Diurnal Cycle

2.1 Data and Methods

In this chapter, the boreal summer mean diurnal cycle will be analyzed in several satellite and reanalysis products, comparing the strengths and weaknesses of these products and noting variability among products. The goal of this chapter is to establish a clear understanding of the background state of the boreal summer diurnal cycle before considering its variability in the next chapter.

2.1.1 CMORPH

The first precipitation dataset considered is from the Climate Precipitation Center (CPC) Morphing Technique, or CMORPH (Joyce et al. 2004). CMORPH is a method for combining and filling the gaps between precipitation estimates from various passive microwave sensors. This technique only uses microwave precipitation estimates from satellites in low-Earth orbit, and then these precipitation features are tracked in space using infrared (IR) retrievals from geostationary satellites, available globally every half hour. The IR information helps track features captured by the microwave sensors through periods when no passive microwave information is available. Furthermore, features are tracked both forward and backward in time, and then morphed using a weighted linear interpolation through time and space to account for changes in intensity and location.

The authors note that this method can outperform other multi-satellite blended techniques, and those that rely on IR brightness temperatures (Joyce et al. 2004). In CMORPH, the IR information is only used to track features captured by the passive microwave instruments, and does not add additional precipitation estimates. CMORPH is an estimate of accumulated precipitation at 8-km (at the equator) spatial resolution, and 30-minute temporal resolution, covering 60S-60N from

1998 to the present. For the Philippines and surrounding waters, this study employs the high resolution version of CMORPH, but also relies on the 0.25° by 0.25°, 3 hourly resolution version when showing data over larger areas, where high spatial resolution isn't as important. May-October precipitation estimates from 1998-July 2017 are included.

2.1.2 TRMM

In addition, precipitation estimates derived from or related to the Tropical Rainfall Measuring Mission (TRMM) are considered. The TRMM Multisatellite Precipitation Analysis (TMPA) is another way of providing a complete, gridded, high spatial and temporal resolution dataset with excellent coverage of the global tropics (Huffman et al. 2007). This technique blends precipitation estimates from passive microwave measurements calibrated with the TRMM Microwave Imager and TRMM Precipitation Radar (PR), and finds a "best" microwave precipitation estimate. Next, IR precipitation estimates are created from 3-hourly brightness temperature readings using the calibrated microwave precipitation estimates. The IR and microwave estimates are then combined. If microwave information is available, for a given point, that estimate is included unchanged, while the gaps are filled in with IR estimates. While this provides the "best" estimate for precipitation rate, it results in some discontinuities showing up in the data. This products is known as TRMM 3B42. The "high-quality" version, or 3B42HQ, which considers only the microwave retrievals without any IR information is also included. These precipitation estimates again come from May-October for 1998-2017, at 0.25° by 0.25° spatial and 3-hourly temporal resolution from 50S-50N. Data is available for October 2014-2017 using the calibrations of microwave and IR information from other satellites established during the TRMM mission, even though these years include no information from the TRMM satellite itself.

A precipitation climatology from the TRMM PR is also separately considered in this thesis. Known as 2A25, this product was an active microwave instrument scanning at 13.8 GHz in low-Earth orbit with 16 orbits per day, from 1998 until the TRMM satellite failed in 2014 (Iguchi et al. 2000). 2A25 provides a radar from space, and thus can produce increased reliability over the

MC (Tabata et al. 2011). However, due to TRMM's small footprint, the spatial and temporal coverage is rather poor, making it only useful for case studies and climatology studies. There is insufficient data to have strong statistics for intra-seasonal variability studies due to the poor sampling frequency. 2A25 is provided in orbital format, at 4-km spatial resolution.

2.1.3 IMERG

The last satellite derived precipitation estimate considered comes from the Integrated Multi-SatellitE Retrievals for GPM (IMERG; Huffman et al. 2018), where GPM refers to the Global Precipitation Measurement Mission satellite, launched in early 2014. IMERG serves as the successor to TRMM 3B42, as its algorithm continues the mission of combining precipitation estimates from all available passive microwave instruments, IR satellite estimates, and surface gauges. IMERG improves the resolution over TRMM 3B42 to $0.1°$ by $0.1°$ spatial resolution, and half hourly temporal resolution, similar to the high-resolution CMORPH. Data is available in full coverage from 60S-60N, and partial coverage globally, from 12 March 2014 to the present. For this study, four full boreal summers from 2014-2017 are analyzed. While IMERG provides excellent resolution and interesting comparisons for the boreal summer climatology, there are too few samples of intra-seasonal oscillations in just four summers to establish statistically significant results.

2.1.4 ERA-Interim

While a new reanalysis, ERA-5, is currently being released by the European Centre for Medium Range Weather Forecasting (ECMWF), it was only available from 2008 to the present at the time of writing. As such, ERA-5's predecessor, ERA-Interim (Dee et al. 2011) was a more attractive option. Several variables are used from ERA-Interim in this study in order to fill in gaps that can't be closed with satellite observations alone, or to provide better temporal resolution or coverage of atmospheric variables thus enhancing results from satellite products. When the diurnal cycle was not of interest for a certain variable, the reanalysis provided at 6-hourly temporal resolution from 1998-2017 (to align with CMORPH and TRMM record) proved sufficient. These were then averaged to daily temporal resolution. 250-hPa wind was used at 1° spatial resolution and 850-hPa wind at 0.25° spatial resolution.

6-hourly resolution was deemed not satisfactory for diurnal cycle studies, so the ERA-Interim re-forecast fields were also included (also from 1998-2017). These were created by running the current version of the ECMWF global numerical weather prediction model on historical data, at 00 UTC and 12 UTC, with output every 3 hours. Some variables (i.e. precipitation, insolation) are defined as accumulation since the forecast time, while others (moisture, wind) are instantaneous estimates. For consistency, the 00 UTC run was selected for all times 03-12 UTC, and the 12 UTC run for 15, 18, 21, and 00 UTC. The re-forecast variables used in this study include surface precipitation at 0.125° spatial resolution and surface wind at 0.25° resolution for the broader Maritime Continent, and 0.125° spatial resolution for the Philippine area of focus. Vertical profiles of cloud water content, specific humidity, relative humidity, and temperature supplemented this analysis near the islands of Luzon and Mindanao. These data were analyzed at 0.125° spatial resolution for 28 vertical pressure levels ranging from 1000-hPa to 100-hPa. Pressure surfaces were found every 25 hPa from 1000-hPa-750-hPa and 250-hPa-100-hPa, and every 50-hPa from 750-hPa-250-hPa. This became very useful for exploring intra-seasonal variability in the diurnal cycle due to its excellent temporal coverage and resolution. This chapter also shows that in the mean state, it aligns sufficiently well with satellite observations.

2.1.5 QuikSCAT

The NASA Quick Scatterometer (QuikSCAT; SeaPAC 2016) was one of the earlier attempts at measuring surface wind from space, and was launched as a recovery effort after the premature failure of the NASA Scatterometer in 1997. The SeaWinds instrument onboard is an active microwave radar operating at 13.4 GHz from a sun-synchronous orbit. The satellite collected data in a 1,800-km wide band at 25-km spatial resolution and covered 90 % of the Earth's surface in one day. This instrument provides estimates of wind speed to an accuracy of 2 ms^{-1}, and direction with an accuracy of 20 degrees over the global oceans. Data is available from June 1999 to its failure in November 2009. This product will be used to examine the climatology of wind, and show consistency with more modern satellite wind estimates, but its nature in sun-syncrhonous orbit limits its use for the goal of exploring the diurnal cycle.

2.1.6 ASCAT

The Advanced Scatterometer (EUMETSAT/OSI SAF 2010) is a newer instrument onboard two European satellites, MetOp-A and MetOp-B. Measurements from the 5.255 GHz scatterometer are then processed by NOAA/NESDIS and converted into wind estimates over the global oceans. While the standard ASCAT wind estimates are provided at 25-km resolution from 2007 to the present from the instrument onboard MetOp-A and from 2012 to the present from MetOp-B, this study will only use the version optimized for coastal oceans from MetOp-A, provided at 12.5-km resolution from 2010 to the present. Wind retrievals are included in this study primary to explore wind patterns in coast waters. Thus, it is most fitting to consider the ASCAT product optimized for these purposes.

2.1.7 RapidScat

The RapidScat instrument is a modified version of the QuikSCAT scatterometer for use on the International Space Station (ISS), to fill in after the loss of QuikSCAT (RapidScat Project 2016). The accuracy of RapidScat is similar to that of QuikSCAT, but its footprint is only half that of QuikSCAT because of the lower orbit of the ISS. Conversely, RapidScat achieves a spatial resolution of 12.5-km. When combined with the previously mentioned ASCAT, they can achieve a total spatial coverage similar to QuikSCAT. The advantage to RapidScat is that the ISS is not in a sun-synchronous orbit like QuikSCAT and ASCAT, so this is the first of the satellite wind retrievals that can be used to examine composite diurnal cycles. Unfortunately, RapidScat was not active long, and data is only available from its launch in October 2014 to its failure in August 2016. Thus, this dataset was used to compare to ERA-Interim on diurnal timescales, and validate use of the reanalysis for intra-seasonal variability studies in the next chapter.

2.1.8 Methods

In this chapter, the boreal summer composite diurnal cycle of several variables will be analyzed in depth. Boreal summer is defined as May-October, the extended warm season in the northern hemisphere. For reanalysis and Level-3 satellite products, this was done by simply averaging together all May-October days, separately for each available time step, to create one composite diurnal cycle at the same temporal resolution as the raw data. For Level-2 satellite products provided in orbital format, including TRMM 2A25, QuikSCAT, ASCAT, and RapidScat, the data was first binned to a 0.25° spatial resolution grid. The wind retrievals were first converted from speed and direction to their zonal and meridional components before binning. The binning process was done with a simple re-grid and average in space, and were binned to the closest time step (at 3 hourly resolution). When multiple measurements fit into the same grid cell at the same time. QuikSCAT and ASCAT were binned just to the day the measurement occurred on, not to a diurnal cycle, and the descending and ascending passes were averaged together. This resulted in a grid at 3-hourly temporal resolution for 2A25 and RapidScat, and daily temporal resolution for the sun-synchronous satellites. Then, these were composited into a boreal summer average diurnal cycle, and boreal summer daily average, respectively. Each pass of the satellite was weighted identically, regardless of if only one measurement from the orbital swath fell into the bin or several measurements were averaged together. Additionally, each wind component was averaged separately, as was wind speed.

The first harmonic of the composite diurnal cycle is a clear and concise way to summarize many features of the mean-state diurnal cycle. The harmonics of this composite were analyzed rather than of the entire time series to avoid complications of extensive data gaps in the orbital records, and to smooth out the maps. At any point in this study when spatial averaging was done to a composite diurnal cycle, the first diurnal harmonic was calculated after all averaging was complete. This chapter explores the amplitude and phase of boreal summer composite diurnal cycles of surface wind, precipitation, cloud water, and humidity near the Philippine islands.

Additional statistical analyses on CMORPH precipitation helps illuminate some intriguing features. To determine the percent variance of CMORPH precipitation that occurs on diurnal time scales, the difference is calculated between the total May-October variance and the variance again of the same time-series, smoothed with a 24-hour running mean. The smoothing effectively removes all variance on diurnal time-scales, leaving only the variance that is of interest. Precipitation probabilities are also considered. This study discusses the probability of any non-zero precipitation rates and the probability of excessively high precipitation. The desired threshold would be one that was sufficiently rare, occurring perhaps only a few times per year, but also often enough that statistics are not based on a handful of extreme events in the entire 20-year record. After some experimentation, the threshold of precipitation rates greater than 15 mm in three hours seemed appropriate. The same threshold is used for all grid points in the study. In other words, the full distribution of all precipitation estimates from every May-October day at 00 UTC was taken for each grid point. Then the fraction of non-zero estimates and fraction greater than the threshold chosen for extreme precipitation were pulled out to estimate their probabilities. This was done for all points and all hours.

2.2 The Background State in Boreal Summer

This chapter now moves to a broad overview of precipitation and wind patterns in boreal summer, before exploring smaller spatial and temporal scales. To understand the pattern in the summer alone, the seasonal progression must also be considered. In Figure Figure 2.1, CMORPH precipitation exhibits a robust seasonal cycle, with southeast Asia, the South China Sea (SCS), and the Philippines showing a pronounced maximum during the summer. This also corresponds to the wet season in the northern Maritime Continent, the region of interest. In this season, precipitation is maximized in a few key regions. Figure 2.2 shows this clearly, with average precipitation rates exceeding 10 mm day^{-1} found near the higher terrain of New Guinea, Borneo, and Southeast Asia, off the west coast of Luzon, the northernmost island of the Philippines, in the eastern SCS, in the PISTON domain near the islands of Palau, and most prominently, along the coast of Myanmar in the Bay of Bengal. This pattern is associated with the ITCZ's summertime northward migration, and the Asian monsoon system. Surface wind from ERA-Interim in Figure 2.3 along with maps of its divergence (not shown) suggest that these regions of high precipitation are collocated with convergent surface wind according to the ERA-Interim reanalysis, as would be expected. There is a broad area of general, large-scale convergence over most of the SCS and Philippine sea, with enhanced convergence on the windward side of landmasses. Similarly, surface divergence is often found on the leeward side of islands and elevated terrain, which is likely a driver of the spatial distribution of heavy precipitation in this season.

Figure 2.3 provides a look at the mean state winds over the Maritime Continent (MC). The summer monsoon pattern is prominent, with cross-equatorial flow coming out of the southeast, and then turning towards the northeast after crossing the equator. This results in strong southwest winds at low levels of the atmosphere in the Bay of Bengal, SCS, and southern Philippine sea, impinging on the southern and western shores of MC islands. At 850-hPa, wind speed is stronger and more zonal than surface winds, while following generally the same patterns. Upper tropospheric winds at 250-hPa in this region are out of the east-northeast, with a speed maximum over the equator. These winds are important for shearing the anvils of storms (Ackerman et al. 1988) as well as regulating the offshore propagation of storms and mesoscale convective systems on diurnal time-scales (Mori et al. 2004, Sakurai et al. 2005, Yanase et al. 2017), a major focus of this thesis.

2.2.1 Comparing Precipitation Datasets

In order to argue that satellite derived precipitation and wind estimates are consistent with one another, a detailed comparison of several datasets is offered for the region near the Philippines. Figure 2.4 shows the boreal summer average precipitation rate near the Philippines from several satellite-derived precipitation datasets. While not shown, there are no significant differences in these conclusions when only considering the period of overlap between datasets. Here, the full available record is considered for each dataset. In the CMORPH record, the precipitation maximum offshore of Luzon is quite evident, as well as another maximum over the higher terrain of northern Luzon. Elevated precipitation rates are also found offshore from the smaller islands of the central Philippines, and over the mountainous terrain of Mindanao, the southernmost major island. Lower average precipitation rates are found east of the Philippines, and to the southwest, between the Philippines and Borneo. The other high spatial and temporal resolution precipitation dataset, IMERG, reveals a similar pattern with a few notable distinctions. Near Luzon, IMERG tends to show higher precipitation rates over and just west of the elevated terrain, with somewhat lower precipitation rates compared to CMORPH in the offshore maximum. This is true even when CMORPH is only composited for the period of data availability for IMERG (2014-2017, not shown).

IMERG's predecessor, TRMM 3B42 shows some differences as well. The high-quality (HQ) version of TRMM 3B42 was also included to eliminate a possible bias due to anvil shearing. Since 3B42 relies on infrared retrievals, it could be biased by high, cold cloud tops that are sheared away from the main area of precipitation, potentially resulting in spurious precipitation rates in areas of deep convection (Ohsawa et al. 2001, Yamamoto et al. 2008). The HQ version is microwave-only, with data gaps remaining in the time-series instead of being filled in with infrared measurements. Both 3B42 products show higher precipitation rates over most of the domain when compared to CMORPH and IMERG. Past studies (e.g. Dai et al. 2007) have argued that CMORPH and TRMM 3B42 both have a tendency to overestimate precipitation over land, and underestimate it over ocean when compared to ground based observations. Others (Tan et al. 2017) have shown that IMERG improves upon TRMM 3B42, but IMERG's record is too short for robust statistics on intra-seasonal variability.

The HQ product shows a spatial pattern most similar to CMORPH with two peaks over Luzon, one over the northern high mountains, and another offshore to the southeast of the island. However, inclusion of the infrared retrievals pushes the spatial pattern closer to IMERG, showing a merged area of increased precipitation, with just a single maximum east of Luzon, and no secondary maximum over the higher terrain. Finally, the TRMM Precipitation Radar (2A25) resampled to the 3B42 grid shows a much noisier pattern due to its limited spatial and temporal coverage. Precipitation magnitudes in the 2A25 retrievals are generally lower in magnitude than 3B42 products, with disorganized spatial patterns qualitatively similar to the CMORPH and microwave-only TRMM. In general, the precipitation patterns are quite similar in each of the satellite datasets, suggesting that similar conclusions can be drawn from each dataset. TRMM 2A25 performs quite well in the MC (Tabata et al. 2011), but its limited spatial coverage restricts its utility for the stated goals of this study. Due to its superior temporal coverage and high spatial resolution, CMORPH will be the primary dataset for this thesis, but evidence from other datasets will be periodically included to strengthen the conclusions. Prior work has shown that while not perfect, satellite derived precipitation estimates such as CMORPH and TRMM 3B42 perform reasonably well even over complex topography (Dinku et al. 2008, Nesbitt et al. 2008, Romilly and Gabremichael 2011).

The last precipitation dataset reviewed comes from the ERA-Interim reanalysis. Since this dataset will be used for several variables other than precipitation as an explanation for the conclusions derived in the next chapter, it is prudent to consider the precipitation fields output by this reanalysis product and compare them to the satellite products. However, since convection in ERA-Interim is parameterized, it likely does not represent precipitation perfectly, despite perhaps being more accurate on the large-scale with dynamic variables (Birch et al. 2015). As shown in Figure 2.4, ERA-Interim qualitatively replicates the satellite-derived precipitation patterns reasonably well. However, it tends to produce more precipitation east of the Philippines, in the Sulu Sea (southwest of the Philippines), and in the southern islands of the Philippines. Over Luzon and the SCS, ERA-Interim looks similar to CMORPH. It also captures the location of the maximum over Luzon's higher terrain reasonably, but has the offshore maximum slightly further south, with generally less definition everywhere. This shows that in the mean-state, ERA-Interim is not an outlier amongst the satellite precipitation datasets.

2.2.2 Comparing Wind Datasets

Several satellite wind products are also compared to ERA-Interim. The satellite products are again available for different time periods (occasionally without any overlap), but the patterns are still qualitatively similar over the Philippines. Figure 2.5 shows the boreal summer mean wind vectors and speed, averaged separately for each dataset's full period of record. Overall, the wind patterns over the ocean are quite similar, which is impressive for such different algorithms, sources, and periods of study. All show the consistent impingement of southwesterly flow on the island of Luzon due to the monsoonal trough, along with a convergence zone near and northwest of the island. On the east side of the Philippines, south-southwest winds near Mindanao and southeast winds further north are consistently found. The most distinct differences are present in magnitude of the average wind speed. QuikSCAT and RapidSCAT tend to show slightly higher wind speeds compared to ASCAT and ERA-Interim. While there is no temporal overlap between QuikSCAT and RapidScat and between QuikSCAT and ASCAT, ERA-Interim shows no significant change between QuikSCAT era and ASCAT/RapidScat era (not shown). The reanalysis winds tend to be weaker than all satellite-derived wind estimates, but wind direction and the spatial distribution of wind speed are remarkably similar. These results suggest that ERA-Interim are useful on these scales, which is advantageous because of its high temporal resolution and coverage.

2.3 The Diurnal Cycle of Precipitation

The diurnal cycle is an important driver of the mean-state of the MC region described in the previous section. An in-depth study of the diurnal cycle will build an understanding of the processes that lead to the observed precipitation and wind patterns, which will be important when considering its intraseasonal variability. Figure 2.6 shows the percent of the total variance in CMORPH precipitation that occurs on diurnal time-scales, described in 2.1.8. The largest fractional variance on diurnal timescales is found over land. Over most landmasses of the MC, about 65-80% of the variance is related to the diurnal cycle. Near coastal oceans have about 55-70% of the variance on these scales, with generally less than 50% of the variance for oceans further from landmasses, such as the waters northeast of the Philippines, and in the center of the SCS. This suggests that understanding the diurnal cycle and its variability will be very important in understanding the regulation of total precipitation and storm development.

Figure 2.7 shows the composite diurnal cycle from all days in May-October from 1998-2017. The time stamps on each panel correspond to 3 hour averages of precipitation, according to the time in Manila, Philippines (UTC+8). This was done to avoid the interpolation that would be required to convert to Local Solar Time and the discontinuities that would result from using the local timezone at each grid point. This product is released as a 3-hour total precipitation accumulation, so this was converted to an average precipitation rate in mm hr^{-1}. Precipitation over land begins to develop between 14:00 and 17:00 for most of the MC islands and mainland Asia. These landmasses tend to see the highest precipitation rates in the late afternoon and evening hours, between 17:00 and 20:00. For the larger landmasses, including Sumatra, Borneo, and mainland southeast Asia, precipitation lingers later into the overnight hours when compared to the smaller islands of the Philippines. Heading into the evening and overnight hours, there is strong evidence of precipitation propagating offshore. This is quite clear off of the west coasts of Luzon in Mindanao from 20:00-02:00. Over land, the highest precipitation rates generally peak over 1 mm hr^{-1} in the CMORPH dataset, while the peak average precipitation rates over coastal ocean are notably smaller, around 0.5-1 mm hr^{-1}. Offshore propagation is also evident from the islands of Sumatra and Borneo, as well as from Myanmar into the Bay of Bengal. These results are largely consistent with previous work on the diurnal cycle in various datasets (e.g. Houze et al. 1981, G.-Y. Yang and Slingo 2001, Mori et al. 2004, Sakurai et al. 2005, Kikuchi and B. Wang 2008).

2.3.1 Precipitation Probabilities

Next, probabilities of precipitation will be addressed in order to provide greater insight into precipitation patterns over the course of a day. Figure 2.8 shows the probability of non-zero precipitation within each 3-hour window. Further, Figure 2.9 shows the average precipitation rate only from time steps in which rain was observed, or the conditional precipitation rate. While this precipitation frequency tells us how often precipitation is expected at a given time of day, the conditional precipitation will tell us essentially how hard it is raining, when rain is falling. Multiplying

Figure 2.8 by Figure 2.9, or the probability it is raining by the average precipitation rate when it is raining, will reproduce Figure 2.7.

There is a robust diurnal cycle in the probability of precipitation over land areas such as the Philippines, Sumatra, and New Guinea. For these islands, over 50% of all boreal summer days observe some precipitation between 14:00 and 17:00 and between 17:00 and 20:00. At the same time, conditional precipitation rates are around 1-1.5 mm hr^{-1} for these the Philippines. Comparatively, for most points on these islands (with the exceptions of New Guinea and mainland Asia's mountainous terrain), precipitation probabilities drop to as low as 10% from 02:00-05:00 and from 05:00-08:00, while conditional precipitation rates drop to 0.5-1 mm hr^{-1}. Precipitation probabilities are nearly five times higher in the afternoon compared to the morning, while conditional precipitation rates roughly double at most. Thus, the diurnal cycle in precipitation feature appears to be more dominant and thus this suggests, in accordance with prior studies (Dai 2001, Dai et al. 2007, Kanamori et al. 2013), the diurnal cycle primarily comes from rainfall occurring more often in the afternoon, and the contribution of higher intensity rainfall is secondary.

Coastal waters tend to see a diurnal cycle in precipitation frequency phase lagged behind the diurnal cycle of the nearby landmass. Offshore propagation is visible when looking at both precipitation frequency and intensity, most obvious near larger islands, suggesting that land-based convection may carry its intensity signal out to sea. Over open water, the diurnal cycle is weak in both frequency and intensity, with perhaps a slight tendency towards an early morning peak in precipitation frequency, and a similar pattern in precipitation intensity. Note that this plot is all based on Philippine time, but in reality, there is a four hour time difference within the domain here, so comparing far sides of the plot could differ by more than one full panel. These results are clarified in light of previous work by Nesbitt and Zipser (2003), who showed that the early morning maximum in precipitation is mostly due to an increased number of mesoscale convective systems. In summary, convection that initiates over land in alignment with the mean diurnal cycle may be more intense on average than precipitation that occurs due to other processes. On the other hand, oceanic convection may vary by time of day in terms of when it is most likely to be present, but its intensity is more random as a function of time of day (Nesbitt and Zipser 2003, Dai et al. 2007).

Finally, the probability of unusually high precipitation rates over the course of an average day is examined. Figure 2.10 shows the probability of a 3-hour averaged precipitation rate greater than 5 mm hr^{-1}. (i.e. greater than 15 mm of precipitation in 3 hours) for each 3-hour window. According to this the CMORPH record, extreme precipitation also exhibits a robust diurnal cycle. Over land, extreme precipitation is most likely in the mid-afternoon and evening hours, aligning with the peak in average precipitation rate. Elevated probabilities also appear to propagate offshore into the overnight hours, indicating that for near coastal waters, high-intensity precipitation is most likely at times of the day when it is expected to be impacted by convection that initiated over land. Over the west Pacific, SCS, and Bay of Bengal, extreme precipitation appears most likely in the morning hours and least likely in the afternoon and evening hours.

This detailed analysis of the boreal summer diurnal cycle in precipitation suggests that precipitation initiates in the early afternoon over topography, and then organizes over larger islands as the afternoon progresses. These areas see significantly increased probabilities in precipitation during the afternoon and evening hours, and extreme precipitation events are also most likely during this period. After the sun sets, convection begins to propagate offshore. Similarly, near coastal waters observe a large diurnal amplitude in precipitation frequency and the probability of very high precipitation rates, and a smaller diurnal cycle in conditional precipitation rates. Over the open ocean, the diurnal cycle is weak, but there is some tendency towards an early morning peak related to an increased likelihood of non-zero precipitation rates and extreme precipitation events. This is generally consistent with previous studies on the mean state diurnal cycle in this region from other datasets, indicating that the diurnal cycle in average precipitation rate is more strongly related to increased precipitation probabilities rather than increased precipitation intensity (Dai 2001, Nesbitt and Zipser 2003, Dai et al. 2007, Baisutti et al. 2012, Kanamori et al. 2013).

2.3.2 The Diurnal Cycle near the Philippines

This section will probe the diurnal cycle over the Philippines and reveal greater detail. A map of the topography from the ETOPO2 dataset (National Geophysical Data Center 2006) in this region is shown in Figure 2.11 with some important geographical features labelled for reference throughout this thesis. For the following discussion, the first diurnal harmonic from the composite diurnal cycle of several satellite derived precipitation datasets is considered to show consistency across sources. Figure 2.12 shows the amplitude of the first diurnal harmonic in boreal summer and reveals a few features evident in all datasets. As expected, the most robust diurnal cycle in precipitation is observed over land, particularly near elevated terrain. Furthermore, the satellite derived precipitation estimates show increased amplitudes extending west of the Philippines in coastal waters. Over land, all data sources agree that the amplitude of the first diurnal harmonic is on the order of 10 mm day^{-1}, indicating a large diurnal cycle when compared to the average daily precipitation rates of around 10-12 mm day^{-1}. While ERA-Interim will not be used to study precipitation statistics, it is still worth noting how well this product captures the diurnal cycle when examining other variables in the reanalysis. At first glance, ERA-Interim appears to show a very similar picture in the amplitude of the diurnal cycle. However, closer examination reveals that the reanalysis has higher amplitudes much more confined to land, with a very sharp gradient in near coastal waters. It does not seem to capture the elevated diurnal cycle amplitudes off of the west coasts of Luzon and Mindanao well. Past studies have shown that models with parameterized convection capture offshore propagation quite poorly, likely due to an ability to represent gravity waves (Love et al. 2011). This is likely a contributing factor to the disparity offshore. While not shown, the difference between the minimum and maximum of the composite diurnal cycle, referred to as diurnal range in this study, provide similar conclusions.

Figure 2.13 shows the variance in the composite diurnal cycle explained by its first diurnal harmonic, in order to show that the first diurnal harmonic is a reasonable approximation for the diurnal cycle. The variance explained is generally quite high, suggesting that the composite diurnal cycle of precipitation in May-October resembles a sine-wave. In the satellite records with the best data coverage (CMORPH and TRMM 3B42 have data available for most time steps on all days from 1998-2017), the islands large islands of the Philippines generally have 60-90% of the variance explained by the first diurnal harmonic, while the diurnal cycle over the smaller islands does not look as much like a sine-wave, possibly due to an earlier peak and rapid decline in precipitation shown in Figure 2.7. These products also agree that the first harmonic is a good approximation for the diurnal cycle over much of the ocean, in the SCS, Philippine Sea, and Sulu Sea. There are two regions for which all data products show that the first harmonic is not an adequate representation. North of Palawan Island (west of the main Philippine archipelago delineating the boundary between the SCS and Sulu Sea) and in the SCS around 18°N, 118°E present variance explained numbers of less than 20%. This could be related to propagating diurnal signals interfering with one another, creating a double peak in precipitation rates.

The other satellite products record much lower variance explained numbers, likely due to poor temporal sampling frequency (TRMM 2A25), and limited temporal coverage (IMERG). Finally, ERA-Interim is similar to the products in showing that the first harmonic is a good representation of the diurnal cycle, but misses many of the spatial distinctions seen in the satellite products. In ERA-Interim, the composite diurnal cycle resembles a sine-wave over land and in the Philippine Sea, with 70-100% of the variance explained. One interesting feature is that the composite diurnal cycle in coastal waters surrounding the Philippines has much lower variance explained by its first harmonic when compared to the satellite products. Taking the satellite products as a "ground-truth" (which is not necessarily true), this suggests that ERA-Interim may have some weaknesses over coastal waters. This is supported by prior work which has shown that models with parameterized convection represent the diurnal cycle of precipitation in regions of complex topography and their offshore propagation poorly (Love et al. 2011, Birch et al. 2015).

Figure 2.14 shows the estimated hour of peak precipitation rate in Local Solar Time (LST) as calculated from the first diurnal harmonic of the composite diurnal cycle. For reference, the hour of peak precipitation (without smoothing via the first diurnal harmonic) of the high resolution datasets is shown in Figure 2.15. This is only shown for the high resolution datasets available at

30-minute temporal resolution because they add more detail than the simple 3-hourly resolution of the other products. For CMORPH and IMERG, it is clear that using the peak hour from the first diurnal harmonic tells the same story as the raw peak hour from the composite, but smooths out the features significantly such that they are less noisy and easier to interpret. There are several important features in Figure 2.14. For ease in interpretation, the hour of peak precipitation is plotted such that if precipitation peaks in or close to daytime, it appears in warm colors (yellows, oranges, and reds), while cool colors (blues and purples) indicate a nighttime peak. Over Luzon and Mindanao, precipitation generally peaks around 17:15-20:15 according to CMORPH, IMERG, and TRMM 3B42, most concentrated close to 18:00. TRMM 2A25 shows a slightly earlier peak over Luzon, around 15:45-18:45. Prior work has suggested that inclusion of IR measurements could lead to a later peak in the diurnal cycle observed (Yamamoto et al. 2008). The smaller islands in the middle of the Philippines generally see earlier peaks in precipitation rate, around 14:15-17:15 in all satellite datasets. ERA-Interim tends to be about 3 hours too early when compared to the 4 multi-satellite products, and about 90 minutes earlier than the TRMM PR, but still shows an afternoon peak in precipitation over land, with Luzon and Mindanao peaking later than the smaller islands. The main findings concerning the diurnal cycle over large islands in the Indo-Pacific warm pool are consistent with other studies focusing on different parts of the Maritime Continent (Gray and Jacobson 1977, Houze et al. 1981, Hartmann and Recker 1986, G.-Y. Yang and Slingo 2001, Sakaeda et al. 2017).

One of the most intriguing features of Figure 2.14 is that it quite clearly shows regions that are affected by precipitation that originates over the Philippines. All satellite datasets show offshore propagation, indicated by progressively later peak times further from land. Immediately offshore of Luzon, and extending south to Minidnao, a late evening peak in precipitation is apparent. A degree or so of longitude offshore (about 100-km) a peak occurs shortly after midnight. By about 200-km west of the Philippines, precipitation peaks in the morning hours. However, the amplitude as previously discussed is fairly small this far from shore, indicating that while there is an enhancement in precipitation at these times associated with convection propagating offshore, it is modest compared to the daily mean precipitation. There is some evidence of propagation on the east side of the Philippines too, as indicated by times getting progressively later heading further from land, but this does not appear to be as prominent as progression on the west side. Studies covering other regions of the global tropics have also indicating a preference for westward propagation offshore for Borneo and Sumatra (Mapes et al. 2003a, Mori et al. 2004, Sakurai et al. 2005, Ichiwaka and Yasunari 2006, Tulich and Kiladis 2012, Yanase et al. 2017).

Another interesting feature is the peak time near the island of Palawan, in between the South China and Sulu Seas. Precipitation over the island itself peaks in the early afternoon, and there is some evidence for cells propagating to the northwest, with precipitation peaking in the evening hours. This is also the region that has a very small fraction of the variance explained by a sine-wave in Figure 2.13. It is possible there is some interference in the composite diurnal cycle in this region between propagation off of Palawan, and propagation off of the Philippines main archipelago, that peaks in the morning hours, as shown by the peak times on both sides of Palawan. This provides more evidence that there could be a double peak over Palawan, but this idea will not be explored further in this study. Finally, ERA-Interim shows some progression towards later peak precipitation rates further from shore, and is consistent with the early morning peak offshore, but the behavior is discontinuous in the near coastal waters, rather than a smooth progression to later peak times as seen in the satellite products. In this case, ERA-Interim is likely not indicating precipitation propagating offshore via gravity wave destabilization and advection (Love et al. 2011), but rather is initiating a separate convective system overnight associated with the land breeze. This will be shown clearly in the next section.

2.3.3 Mean-state Offshore Propagation near Luzon

This section take a closer look at offshore propagation from the island of Luzon in order to gain more insight into the characteristics of the diurnal cycle, and provide some more information on the differences in offshore propagation in various datasets. To show a clear and smooth signal, precipitation rates from the composite diurnal cycle are averaged latitudinally from 16°-18°N for longitudes in the vicinity of Luzon. The topography (National Geophysical Data Center 2006) of the Philippines and a box showing the region of averaging for successive plots in this section (and Chapter 3) are shown in Figure 2.16. Box "A" in this plot covers northern Luzon and will be used in this section. Figure 2.17 shows these composite precipitation averages as a function of time of day in Philippine Time (PHT) for each of the precipitation datasets considered. On the bottom, the average topography is included over the same longitudes to clearly identify where and when convection occurs with respect to the mountains and the coastline. In the selected longitude band, topography is aligned in two mountain ranges. On the west side of the island is the higher of the two, the Cordillera Central, with the average topographic height approaching 1500-m. Some of the higher peaks not resolved in the average reach to nearly 3000-m. In the center of the island, a deep valley close to sea level is present, followed by another shorter and narrower range of mountains, the Sierra Madre, on the east side of the island. Precipitation plots are oriented such that noon is at the top of the plot, generally near the expected "beginning" of the diurnal cycle of precipitation over land, with time increasing downwards

The CMORPH average precipitation propagation supports some of the features identified in prior sections. Precipitation first initiates over the Cordillera Central around noon, reaching a peak around 15:00 over the tallest peaks, and then spreading into the valley to the east and to the west coast. Into the evening hours, CMORPH shows robust offshore propagation to the west, and also some minor propagation to the east of the island. In the composite diurnal cycle, propagating precipitation continues further than 100-km out to sea, with a weak signal lingering out to 200-km west of Luzon. The other satellite datasets are in strong agreement with CMORPH. TRMM products and IMERG shows higher precipitation rates in the afternoon maximum over Luzon compared to CMORPH. The 3B42 products show generally higher precipitation everywhere at all times, whereas IMERG generally shows similar precipitation rates to CMORPH outside of the afternoon maximum. The TRMM Precipitation Radar, while much noisier, also has evidence of offshore propagation shifted an hour or so earlier compared to the other products, consistent with the discussion in the previous section and prior work.

When directly comparing TRMM 3B42 with and without Infrared, the results are generally similar but with some notable differences. When infrared measurements are included, the product shows increased precipitation rates and better propagation to the west of the island, while exhibiting weaker propagation to the east. In addition, the IR measurements cause the maximum over the Cordillera Central to persist a few hours longer than in the HQ product. This would be consistent with the hypothesis of anvil shearing potentially biasing the 3B42 product. As mentioned in the prior section, prevailing upper level winds are out of the east-northeast, which would promote shearing of anvils to the west-southwest. Thus, relying solely on IR (which happens when gaps need to be filled in 3B42), may cause the algorithm to identify heavy precipitation biased to the west-southwest (Ackerman et al. 1988).

Lastly, the diurnal cycle in ERA-Interim looks broadly similar to the diurnal cycle in satellite products, but with some notable differences. The diurnal cycle in ERA-Interim is less pronounced over land, with a lower maximum precipitation rate in the afternoon, and higher minimum precipitation rate in the early morning. Furthermore, precipitation tends to initiate earlier when compared to the satellite products. ERA-Interim shows precipitation initiating in the same location as the satellite products, but about 1-2 hours too early. It also tapers the afternoon peak too early, around 18:00 instead of lingering until 21:00 as shown in the satellite products. The most pronounced and important distinction occurs with offshore propagation. While ERA-Interim shows a diurnal cycle over the ocean, it doesn't appear to have as robust of offshore propagation. There is modest evidence of westward propagation off the coast, but it is relatively weak. Instead, the reanalysis does show an increase in oceanic precipitation rate 100-200-km offshore from around midnight to 07:00. The same pattern appears on the east side of the island. While this part agrees with the satellite products, it doesn't connect to the precipitation that initiated over land. One possibility is that the model is not showing sufficient offshore propagation in the mean state, but it is simulating the land-sea breeze circulation adequately, and thus capturing a nighttime maximum over the ocean due to the land breeze (Love et al. 2011, Birch et al. 2015). Thus we proceed with caution when making sweeping conclusions about the propagation of the diurnal cycle based on ERA-Interim fields as reality, noting the potential weaknesses in its convective parameterization. However, the next section will show that even with these weaknesses its representation of precipitation propagation, it can replicate wind patterns adequately.

2.4 The Diurnal Cycle of Surface Wind

The sea-breeze and mountain-breeze circulations play important roles in driving precipitation on diurnal scales over high topography and near coastlines (Qian 2008, Birch et al. 2015). Limited wind estimates will be used to explore the diurnal cycle of surface wind in boreal summer in and around the Maritime Continent, with a focus on the Philippines. It is somewhat difficult to discern the diurnal patterns by just looking at wind speed and wind vectors plotted on a map, so instead the u- and v-components of the surface wind vectors are shown separately. Studying diurnal variations in wind in this region using observations is a challenge. The best, long-term satellite-derived wind estimates come from QuikSCAT and ASCAT. However, both of these satellite are in sun-synchronous orbits, and pass over the a given point on the Earth's surface twice a day, at the same time of the day. Thus, while robust statistics can be built on wind at those specific times of day, two samples per day this is insufficient to study the diurnal cycle. At least 8-samples per day would be desired in order to feel comfortable drawing conclusions. Finally, CYGNYSS is relatively new, and does not provide information on wind direction, which limits its utility to this study. Thus, for gridded satellite observations, that leaves RapidScat.

RapidScat provides was collecting data from onboard the International Space Station (ISS) from 3 October 2014 until it failed on 19 August 2016. The ISS is in a non-sun-synchronous low-Earth orbit, which means that over a long period of time a composite diurnal cycle can be constructed. The orbital RapidScat data were binned to 0.25° by 0.25° spatial resolution and 3-hourly temporal resolution at synoptic times, and then constructed a composite diurnal cycle for the nearly two full boreal summers sampled by the satellite. While this provides a useful view of the mean-state diurnal cycle in the SCS (Lang et al. 2017), it will not be sufficient for studying intraseasonal variability since only two seasons are present. Thus, the ERA-Interim re-forecasts available at synoptic times will be employed, and show that it displays patterns very similar to RapidScat in the composite diurnal cycle. After comparing the two in this section, ERA-Interim will be used primarily to examine the variability of the diurnal cycle as a function of phase of the intraseasonal oscillation, as statistics will be much stronger with decades of data.

Figure 2.18 shows the composite May-October diurnal cycle of surface zonal wind for both ERA-Interim and RapidScat. Similarly Figure 2.19 shows the same for the meridional wind. In this thesis, that positive wind components mean winds from the south or west, and negative wind components mean wind from the north or the east, following convection. While RapidScat is noisier, remarkable similarities to ERA-Interim can be seen. Both show surface easterlies to the north and east of the Philippines and strong westerlies in the SCS and Sulu Sea. For meridional wind, most times of day have consistent weak to moderate southerly flow, but the noise present in RapidScat does show northerlies particularly around Luzon at some times of day. It is unclear if this is real, or a product of the satellite retrieval or short record. While composites of ERA-Interim re-forecast winds for only the 2014-2016 RapidScat period (not-shown) are much closer to RapidScat, some discrepancies remain.

Both the reanalysis and satellite show a strong sea-breeze circulation in zonal wind. Considering the north-south oriented coastlines, the mean state generally shows westerly surface winds impinging on Luzon's west coast (onshore) in both products during the afternoon hours. However, near midnight and into the early morning hours, this shoreline tends to see near zero zonal wind component, or perhaps a weak easterly wind, indicating a weak land-breeze. This circulation pattern is also apparent on the east side of Luzon, and on both sides of Mindanao in the southern Philippines. Since most of the coastline in this region is oriented generally north to south, the diurnal cycle of meridional wind is not quite as interesting. However, both products do show near zero or northerly winds on the north shore of Luzon during the afternoon, and stronger southerly (offshore) winds during the early morning.

The areas that see the strongest diurnal cycles are easily pinpointed in Figure 2.20. This figure shows the amplitude of the first diurnal harmonic of the May-October composite diurnal cycle, similar to Figure 2.12, but for each wind component, and wind speed, all averaged separately. This provides a smoothed look at what is approximately one-half the difference between the maximum and minimum of the composite diurnal cycle. High amplitude oscillations in zonal wind are present along all coastlines oriented north to south (Luzon, Sumatra, southeast Asia, certain aspects of Borneo). Land masses oriented east to west (parts of Sumatra, Java, and Borneo) tend to have a strong amplitude of the diurnal cycle of meridional wind. Interestingly, the near-coastal ocean sees very small amplitudes in the diurnal cycle of wind speed, suggesting that the change in wind direction is much more important. According to ERA-Interim, there is a notable diurnal cycle in wind speed over landmasses, but reanalysis surface winds over topography could be unreliable. In summary, ERA-Interim and RapidScat paint a very similar picture of the diurnal cycle of surface wind in the MC. Each product captures a robust sea-breeze circulation in near coastal waters consistent with previous studies (Houze et al. 1981, Birch et al. 2015, Lang et al. 2017). The similarities between the two in the mean state, and agreement with well established theory, suggest that ERA-Interim may be trustworthy as a reliable representation of historical wind patterns in this area

2.5 Diurnal Variations in Vertical Structure near Luzon

The last topic discussed in this chapter is the vertical profile of moisture, cloud water, and wind. An understanding of the mean-state diurnal cycle in the vertical structure will be important to understanding intra-seasonal variability in offshore propagation. Figure 2.22a shows the May-October composite diurnal cycle in cloud water content and zonal and vertical wind from ERA-Interim re-forecasts averaged latitudinally over the same box covering Luzon shown in Figure 2.16. Figure 2.22b shows the anomalies of these variables from the daily mean. ERA-Interim does fill in values on all pressure levels, even if the isobar intersects land, so values over the Cordillera Central are not reliable below about 850-hPa. The first evidence of vigorous convection appears at 11:00 local time, when there is a surge in cloud water content around 700-800-hPa, over the island of Luzon. Furthermore, a weak sea-breeze is evident on both sides of the island with upward vertical motion beginning to increase in the convergence zone over the mountains. Clouds do follow the topography reasonably closely, with the highest clouds directly over the tallest peaks at this time, and enhanced cloud water content at slightly lower elevations both east and west.

By the early afternoon hours, convection has surged to the tropopause into a towering cumulonimbus cloud, with enhanced cloud water content all the way from 800-hPa to the tropopause in association with strong upward vertical motion and a robust sea-breeze. There is some evidence of enhanced cloudiness propagating westward offshore during the evening and overnight hours, while clouds gradually clear to near or below the daily mean values over Luzon. Again, however, the reanalysis does not show consistent offshore propagation. While there is enhanced cloudiness in the upper troposphere just offshore at 20:00, this disappears by 23:00, before reemerging in the mid-levels during the early morning, corresponding to the same times of day that the precipitation composite sees a gap in offshore propagation. Convection appears to weaken near the coast in the re-forecasts, before re-emerging further offshore. It's disagreement with satellite observations suggest that at least at 23:00, ERA-Interim may be showing spuriously low values of cloud water content and precipitation. The sea-breeze and thus convergence induced upward vertical motion weaken significantly in the evening hours to near zero wind speeds, perhaps with a slight land breeze and weak subsidence. The magnitude of the land-breeze is much weaker than the daytime sea-breeze, indicating that it alone may not be responsible for the nocturnal precipitation maximum offshore. Prior studies have argued that gravity waves initiated by the diurnal cycle over high topography drive precipitation propagation (Mapes et al. 2003b, Love et al. 2011, Hassim et al. 2016).

Figure 2.22 shows the amplitude and peak hour of the first diurnal harmonic of the boreal summer composite diurnal cycle of latitudinally averaged specific humidity from ERA-Interim. All compositing and averaging was done before calculating the first diurnal harmonic. The amplitude in the diurnal cycle of specific humidity is shown as a percent of the daily mean value of specific humidity, so that the vertical structure is visible even when upper tropospheric humidity values are dwarfed by much larger humidity values closer to the surface. The strongest diurnal cycle occurs primarily in lower levels between 700- and 900-hPa and again in upper troposphere above 400-hPa, with little diurnal cycle between 500- and 700-hPa. This is likely related to evaporation of cloud water, as cloud water in Figure 2.21 exhibits smaller anomalies in the middle-troposphere. Strong diurnal cycles in specific humidity are also prevalent at the same levels of the atmosphere offshore to both the west and east of Luzon. The timing of these features provides some insight into their origins.

Over land, specific humidity peaks in the early to mid-afternoon hours at all levels of the atmosphere. This is slightly earlier than expected given the peak times of precipitation from the satellite products, but recall that ERA-Interim also showed its peak precipitation rates slightly earlier than in the satellite products. Elevated specific humidity in the lower- and upper-troposphere also propagate westward offshore, as evidenced by progressively later peak times further from shore. Interestingly, the speed of propagation of these specific humidity anomalies is different between the two levels. At about 800-hPa and 150-km offshore, humidity peaks between 21:00 and midnight, while at 400-hPa the peak is actually closer to 03:00. It is hypothesized that the apparent propagation of the upper-tropospheric humidity is related to evaporation of hydrometeors advected from the cloud tops by the mean wind, as propagation speeds are consistent with the upper-tropospheric wind speed. While the apparent propagation in the lower-troposphere is close to the speed of precipitation propagation, ERA-Interim does not capture this well, leaving this feature as an open question.

2.6 Chapter Summary

In this chapter, a thorough examination and synthesis of the mean state diurnal cycle in boreal summer has been presented, with a focus on the features near the Philippine island of Luzon and offshore propagation of convection. Over the islands of the Maritime Continent, an onshore sea-breeze develops in the late morning hours, fluxing moisture from the ocean towards the high topography of the islands. Cumulus clouds develop shortly after, and then rapidly develop into towering cumulonimbus clouds that reach up to the tropopause. For smaller islands, precipitation peaks during the early to mid afternoon hours. However, for larger landmasses, convection continues to organize into the evening hours, leading to a later peak in precipitation. Upper level winds from the east northeast shear some of the anvil clouds off to the west southwest. As the sun begins to set, this convection that developed near the coast start to propagate offshore in all directions, but with west southwest favored. Offshore, precipitation then reaches a peak overnight and into the morning hours, later further from land. This is likely enhanced by the development of the land-breeze overnight. The amplitude of the diurnal cycle is much more dramatic over the islands, but still notable in coastal waters as these areas are influenced by convection that originated over land. This chapter also explored the diurnal cycle of wind and precipitation in a few different datasets. A strong land-based diurnal cycle with an afternoon peak associated with a strong sea-breeze is seen in all datasets examined. While the satellite precipitation products have subtle quantitative differences, they qualitatively agree that storm cells initiated by the diurnal cycle over land slowly propagate offshore during the overnight hours. This feature is not well represented in ERA-Interim reanalysis, despite representing the diurnal cycle over land and ocean separately with reasonable skill. Now that an understanding of the basic state of the diurnal cycle in this region as been established, its intraseasonal variability can be examined.

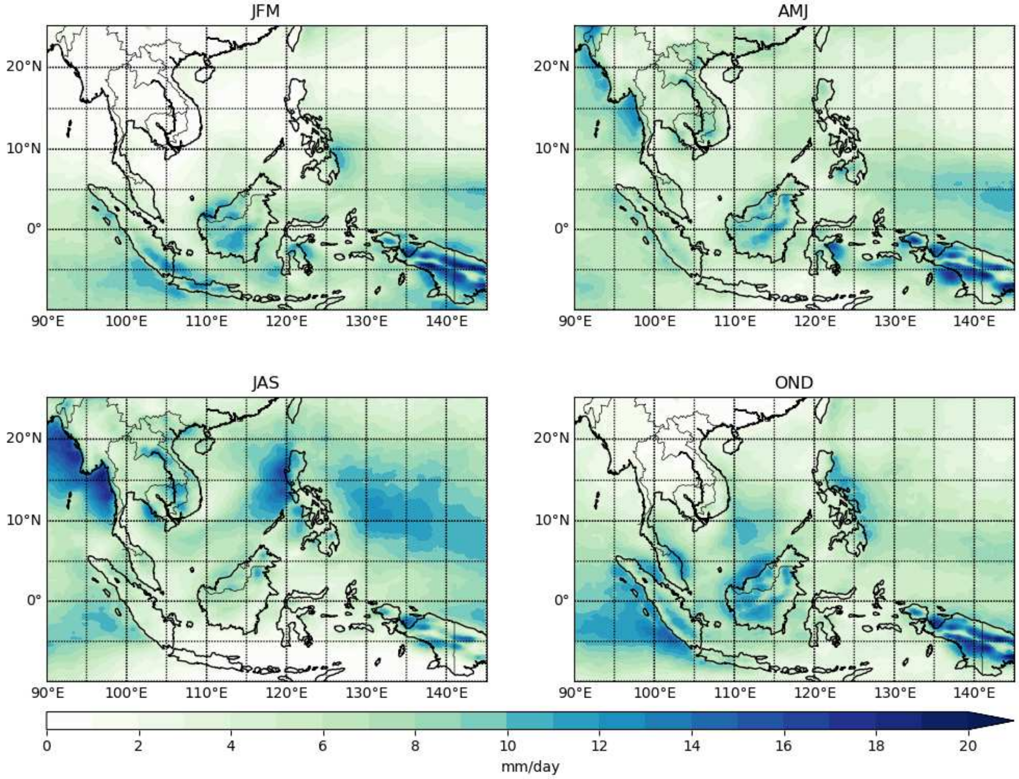

Figure 2.1: Average Precipitation Rate in mm day^{-1} from CMORPH in January-March (top-left), April-June (top-right), July-September (bottom-left), and October-December (bottom-right).

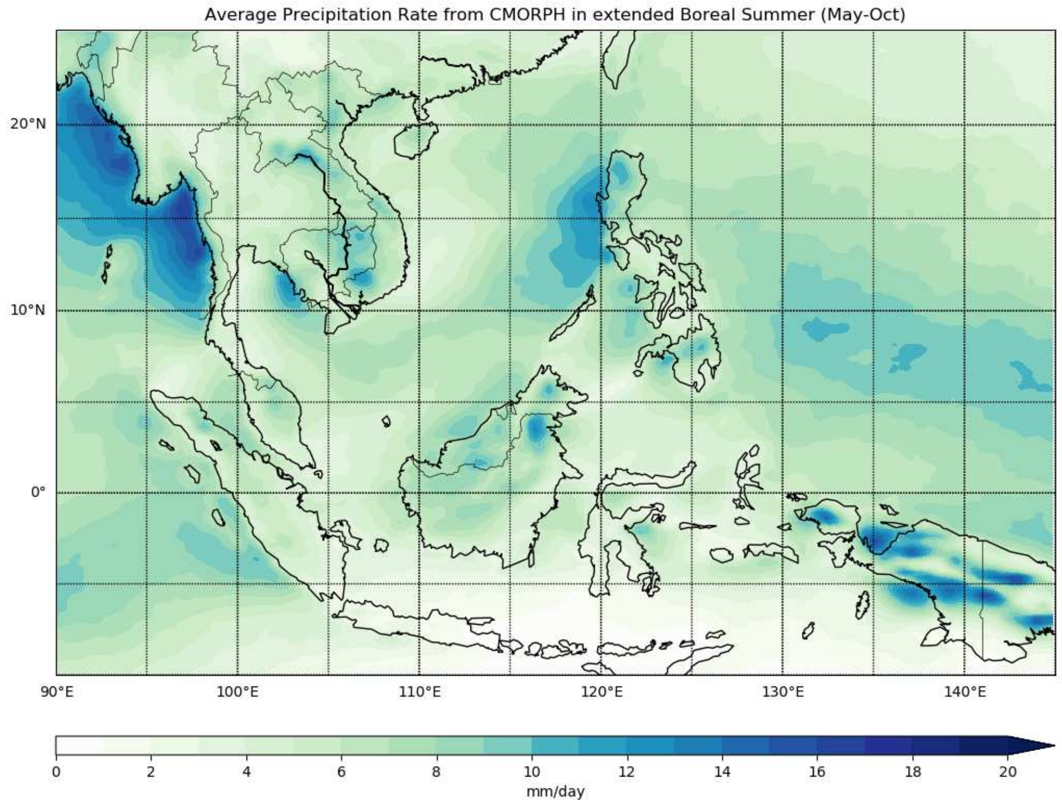

Figure 2.2: Average Precipitation Rate in mm day^{-1} from CMORPH in May-October.

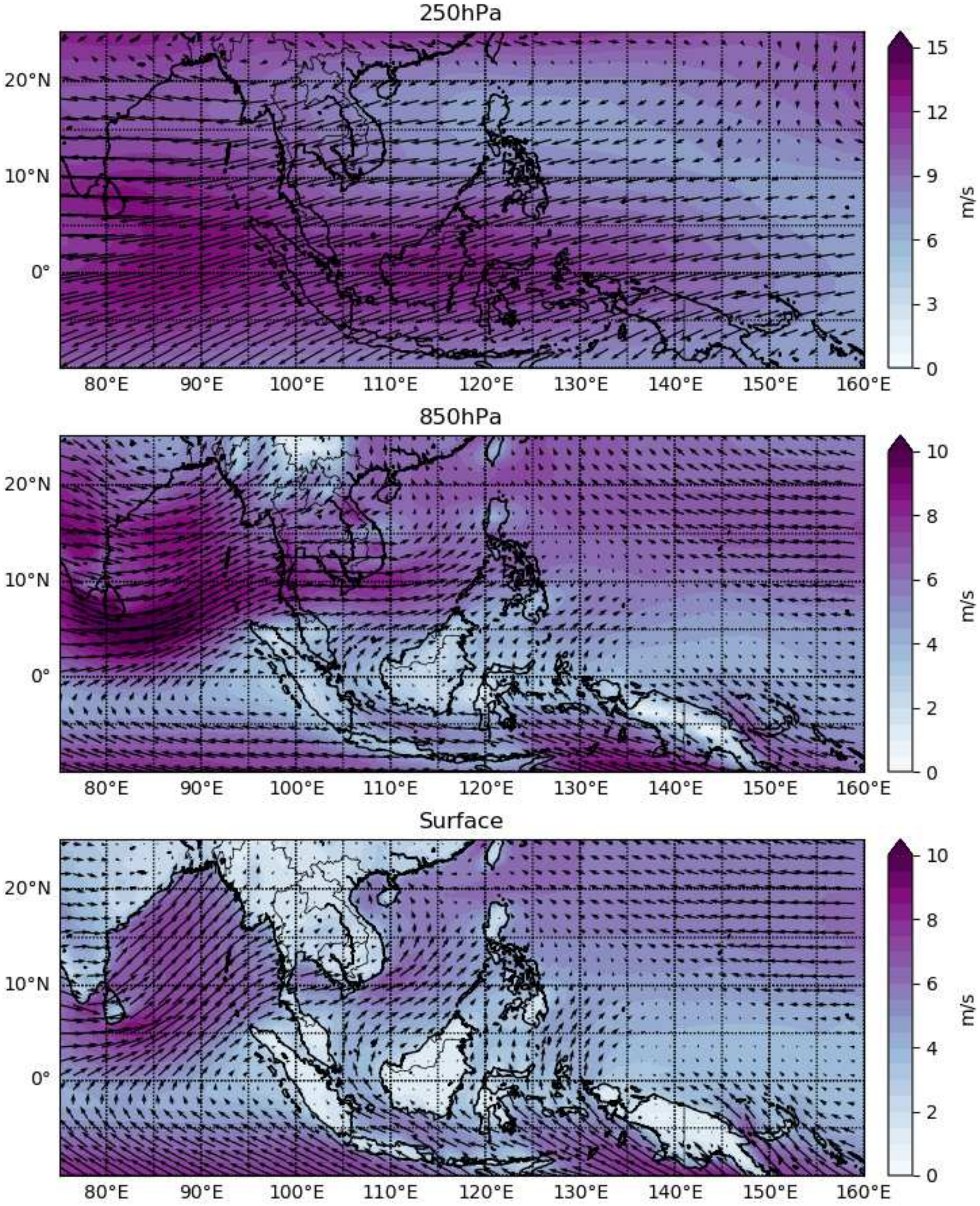

Figure 2.3: Average wind speed in m s^{-1} and vectors in May-October.

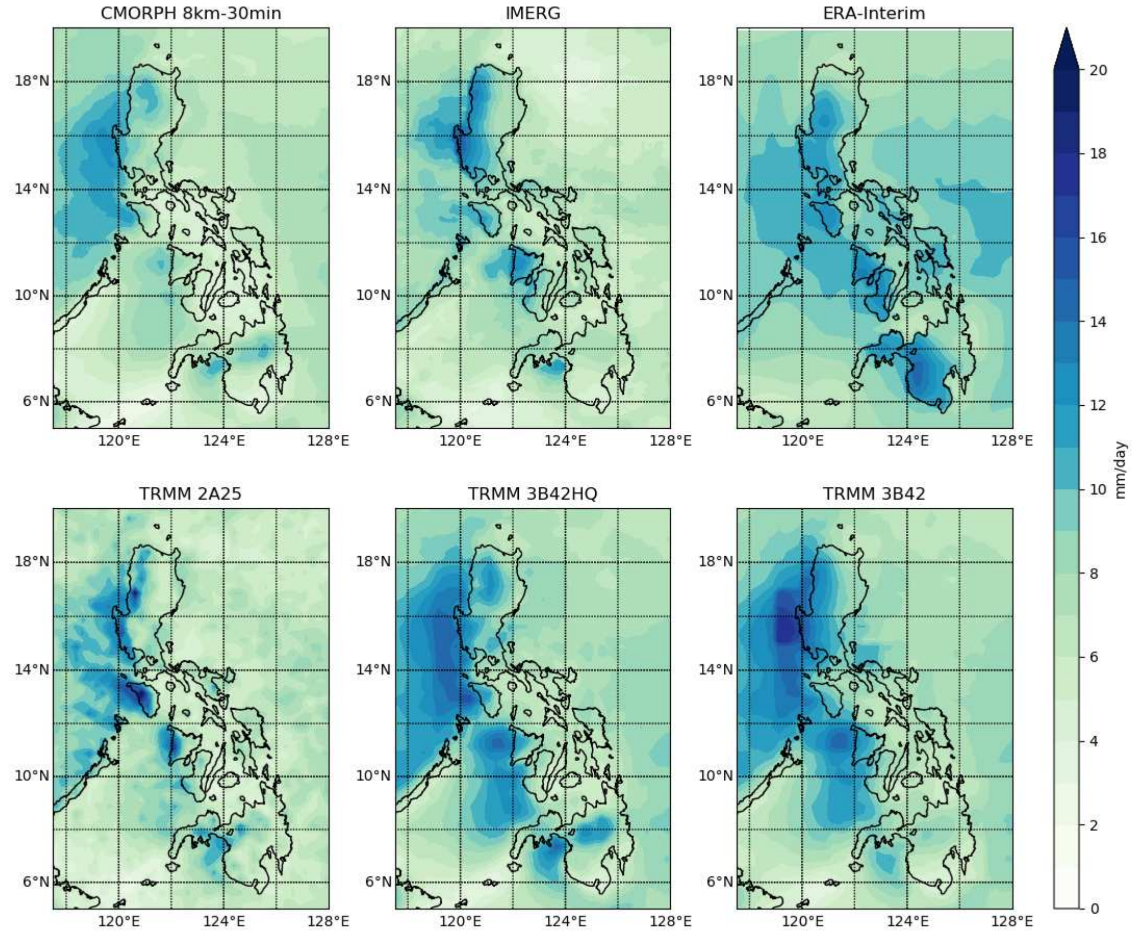

Figure 2.4: Average Precipitation Rate in mm day^{-1} from CMORPH (top-left), IMERG (top-middle), ERA-Interim (top-right), TRMM 2A25 (bottom-left), TRMM 3B42 High Quality (bottom-middle) and TRMM 3B42 with Infrared (bottom-right).

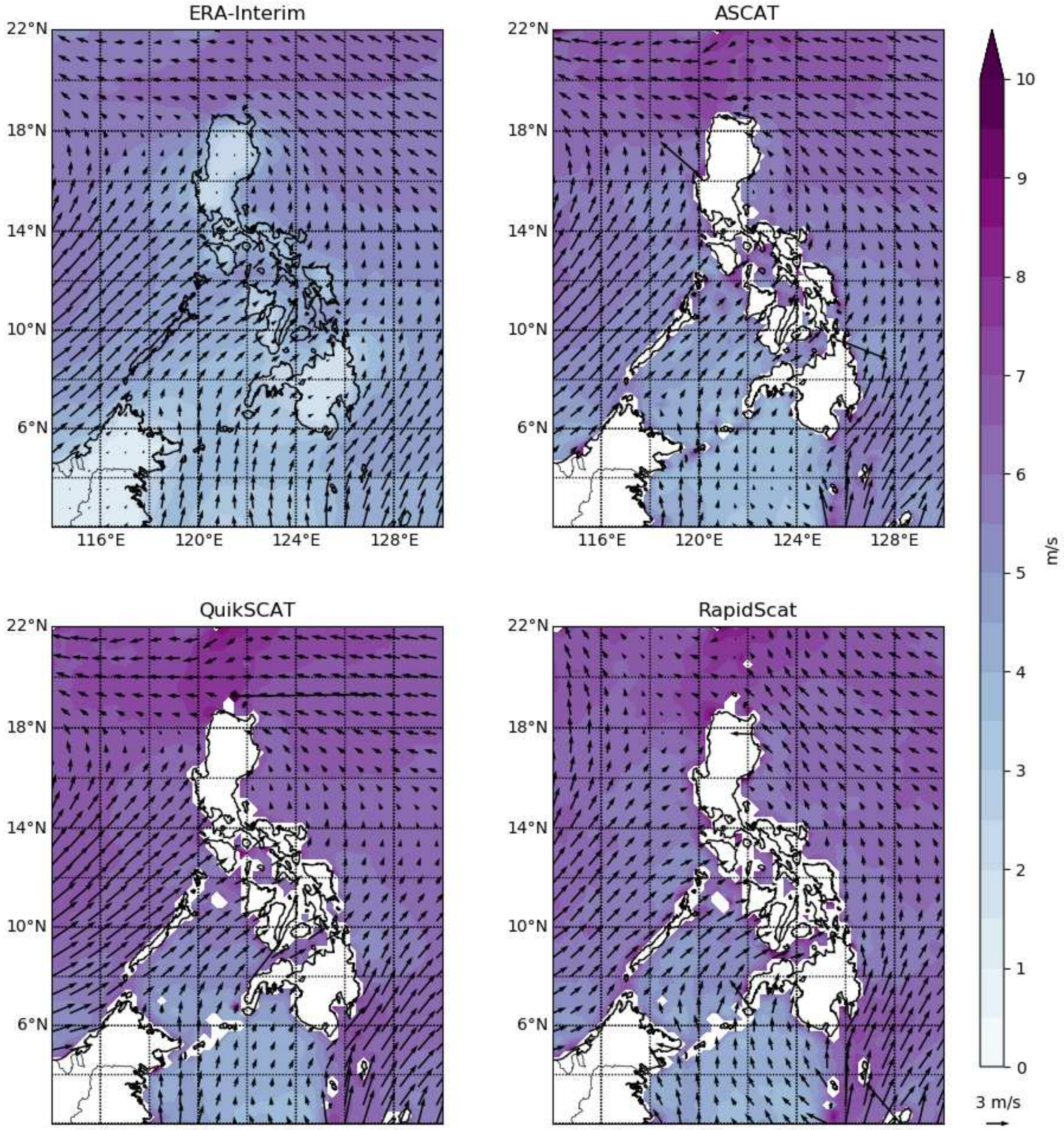

Figure 2.5: Average surface wind speed in m s^{-1} and vectors in May-October from ERA-Interim (top-left), ASCAT (top-right), QuikSCAT (bottom-left), and RapidScat (bottom-right).

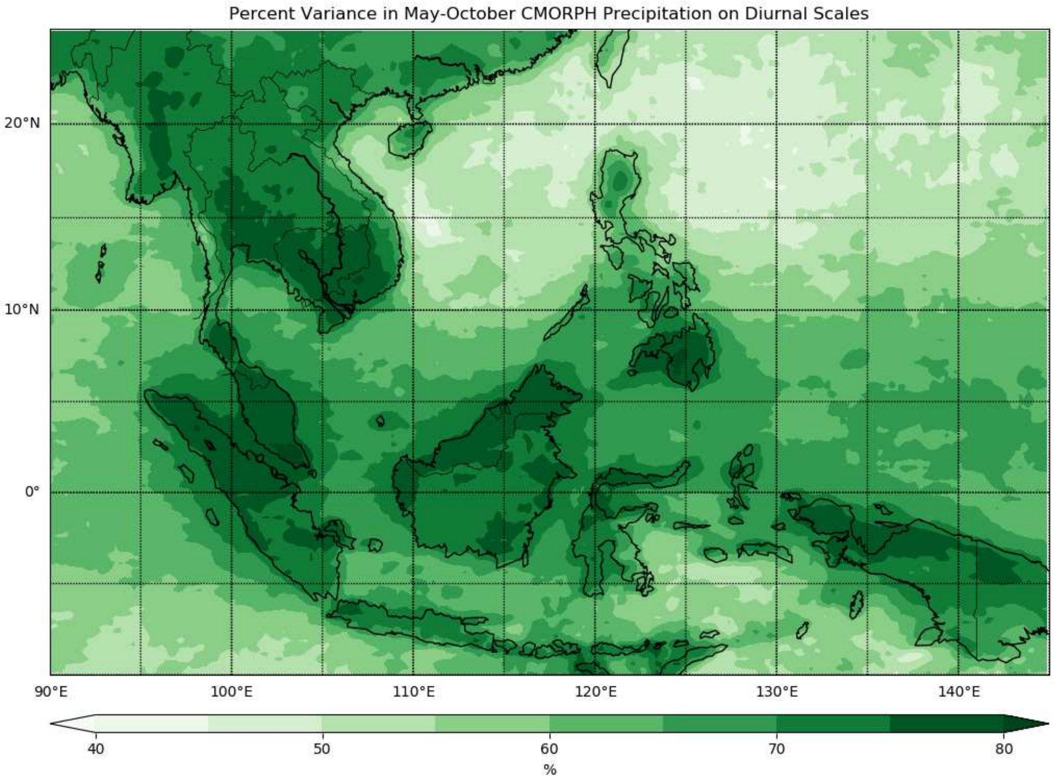

Figure 2.6: Percent Variance in May-October CMORPH precipitation on diurnal time-scales, from data at 3 hourly temporal resolution.

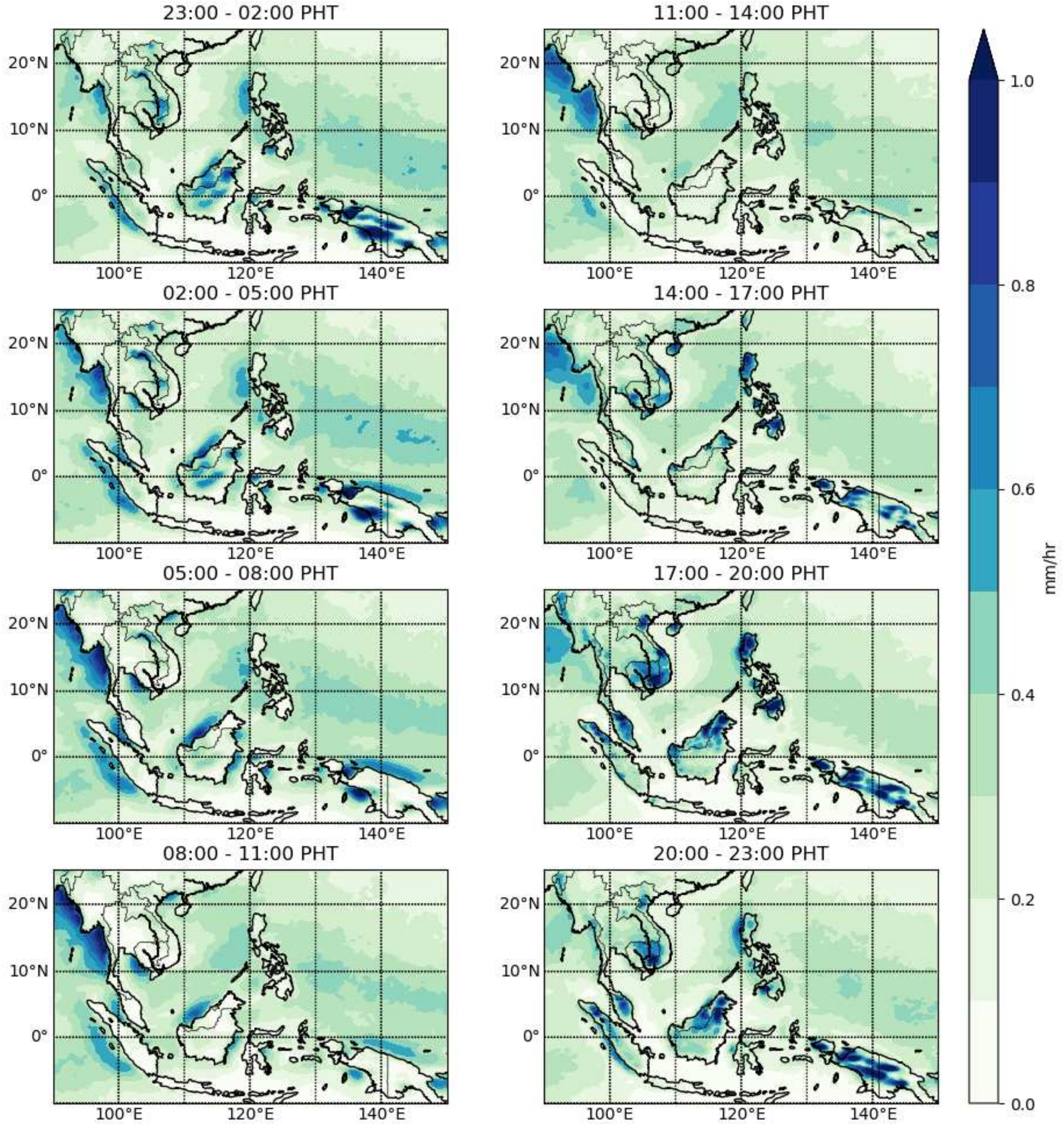

Figure 2.7: Average precipitation rate in 3 hour windows, labelled by hour in Manila, Philippines (UTC+8), in mm $hr^{-1}$from CMORPH from all May-October days, 1998-2017.

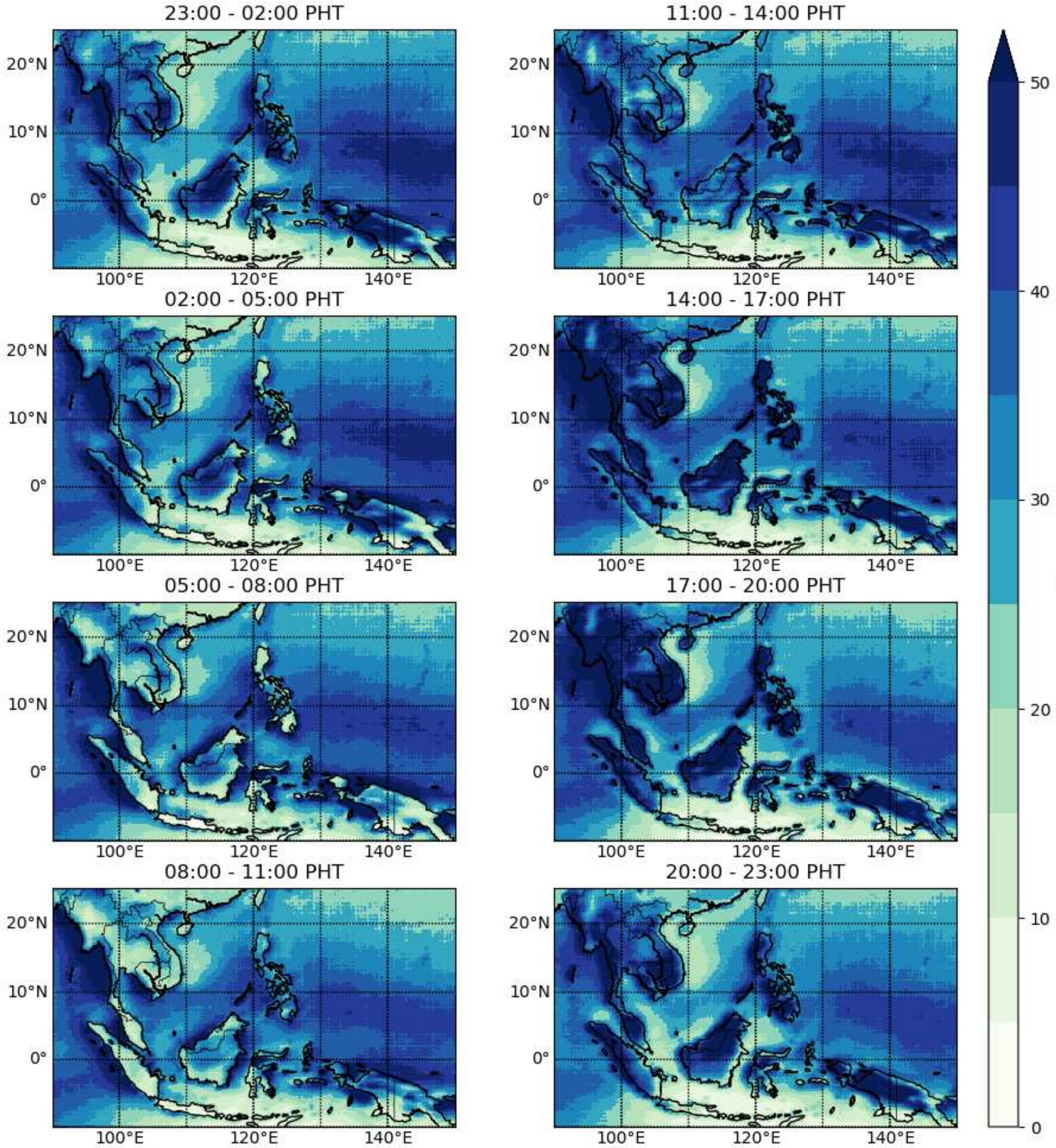

Figure 2.8: Probability of precipitation during the 3-hour window (UTC+8) labelled in May-October from CMORPH.

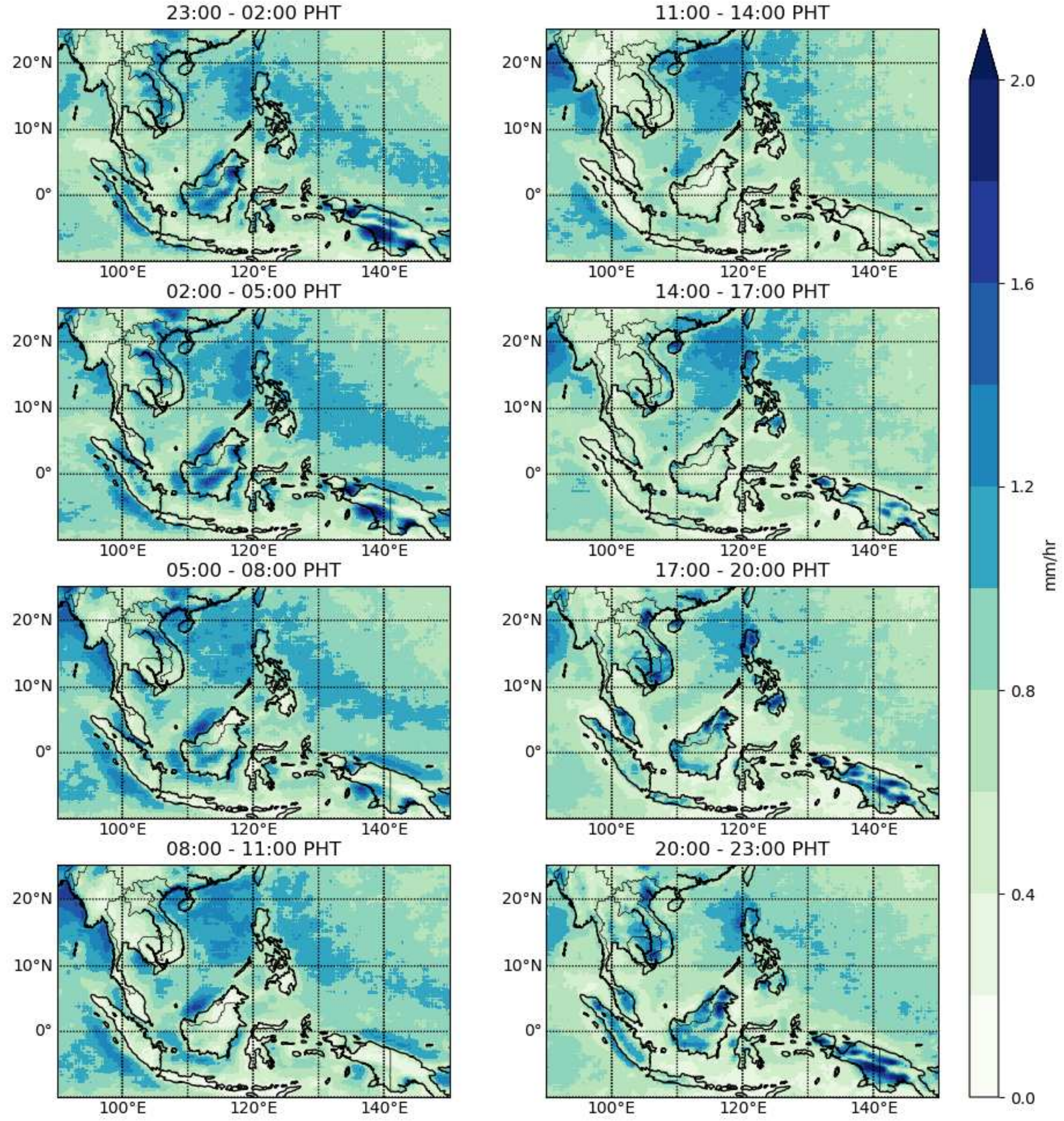

Figure 2.9: Average precipitation rate in mm hr^{-1}, only in time-steps that non-zero precipitation is observed, labelled by hour in Manila, Philippines (UTC+8), from CMORPH in May-October.

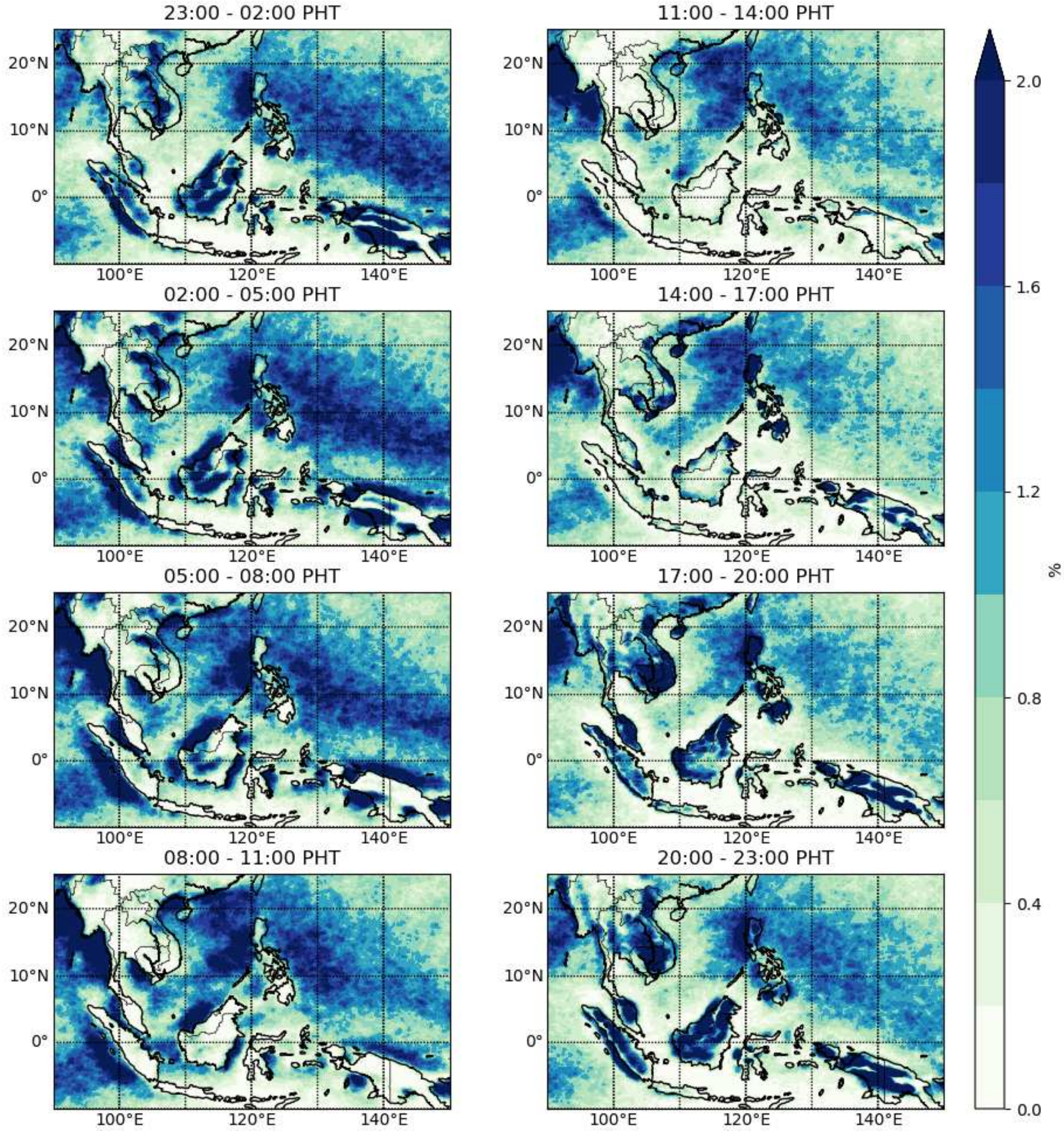

Figure 2.10: Probability of a 3-hour averaged precipitation rate greater than 5 mm hr^{-1} (i.e. greater than 15 mm in 3 hours) by time of day in Manila, Philippines (UTC+8).

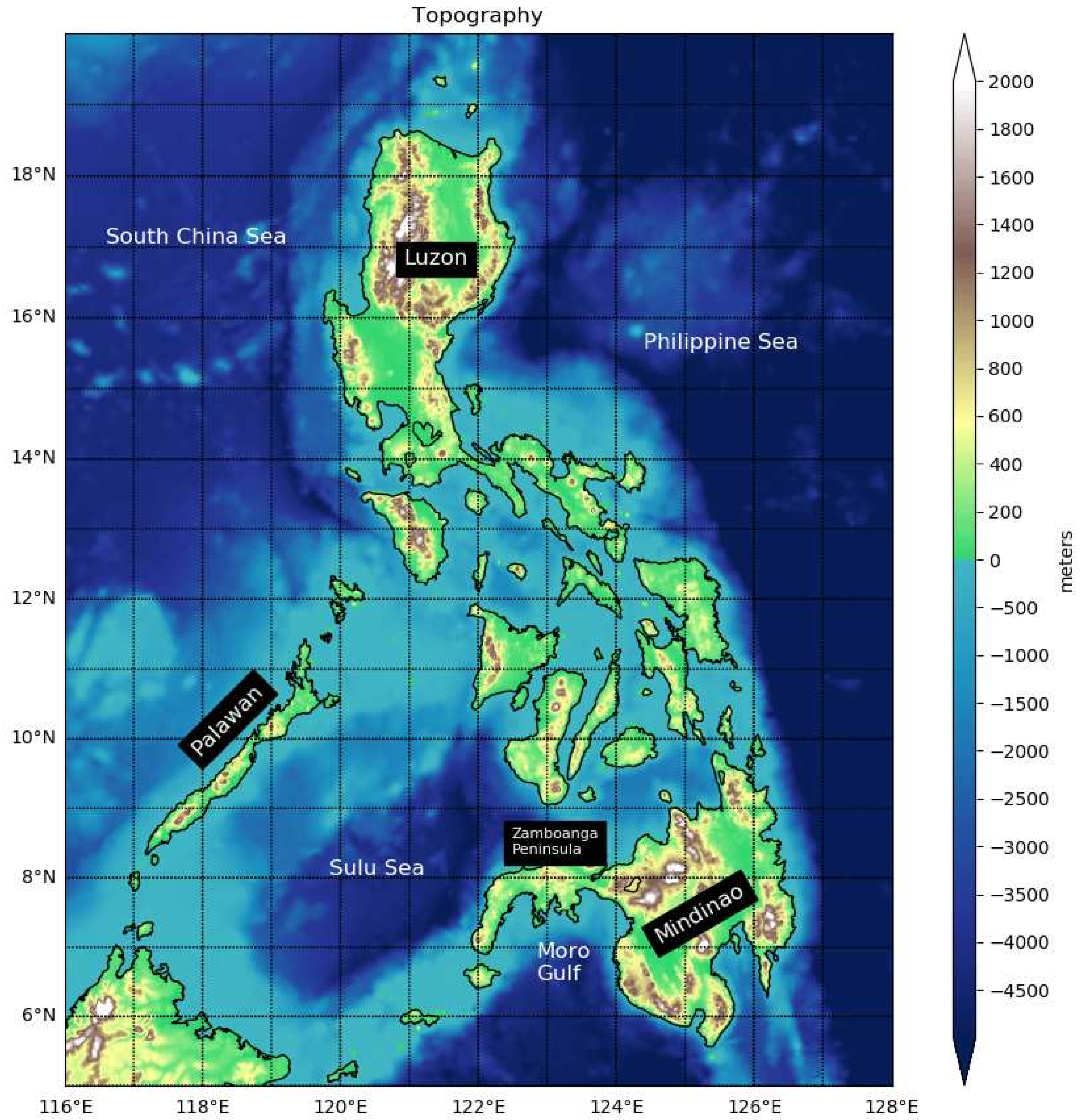

Figure 2.11: ETOPO2 topography and bathymetry (in meters) with labels for important geographical features.

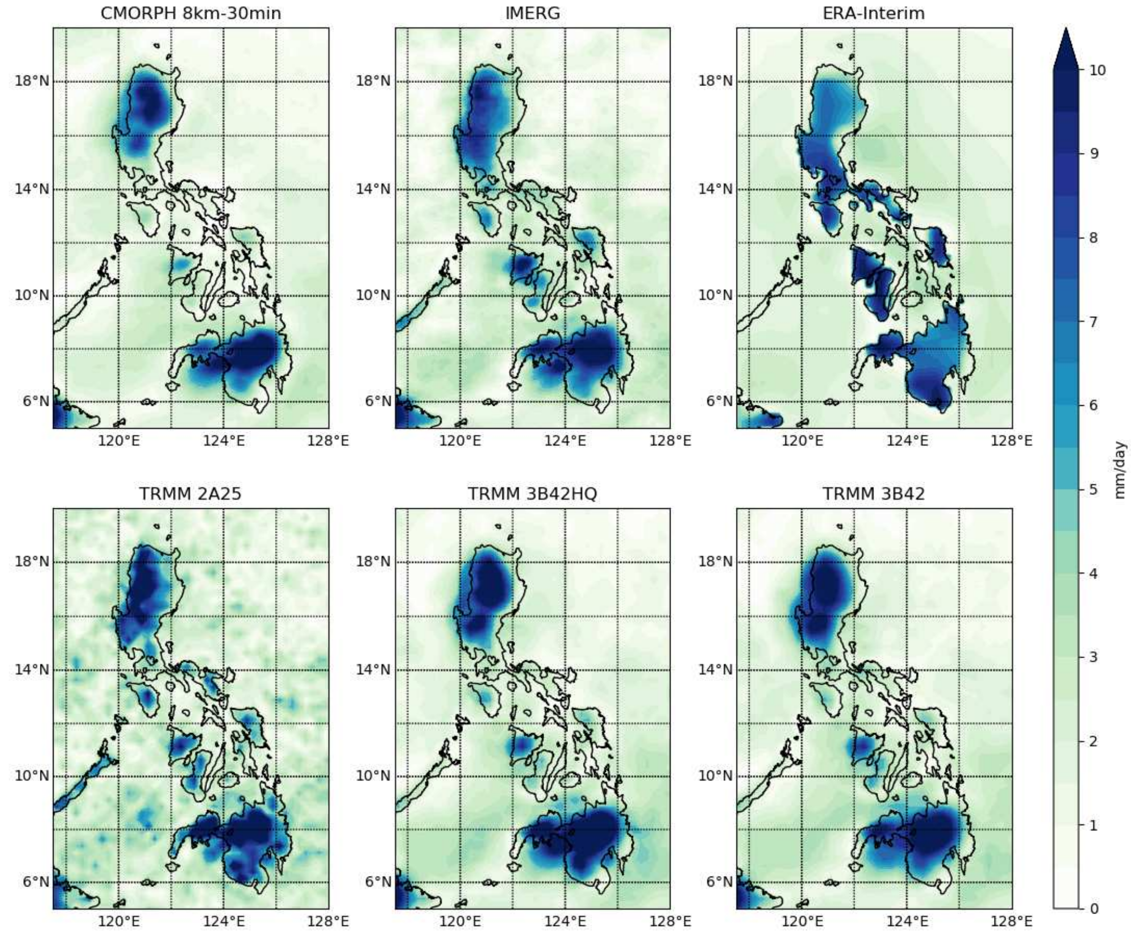

Figure 2.12: Amplitude of the first diurnal harmonic of the May-October composite diurnal cycle from CMORPH (top-left), IMERG (top-middle), ERA-Interim (top-right), TRMM 2A25 (bottom-left), TRMM 3B42 High Quality (bottom-middle) and TRMM 3B42 with Infrared (bottom-right).

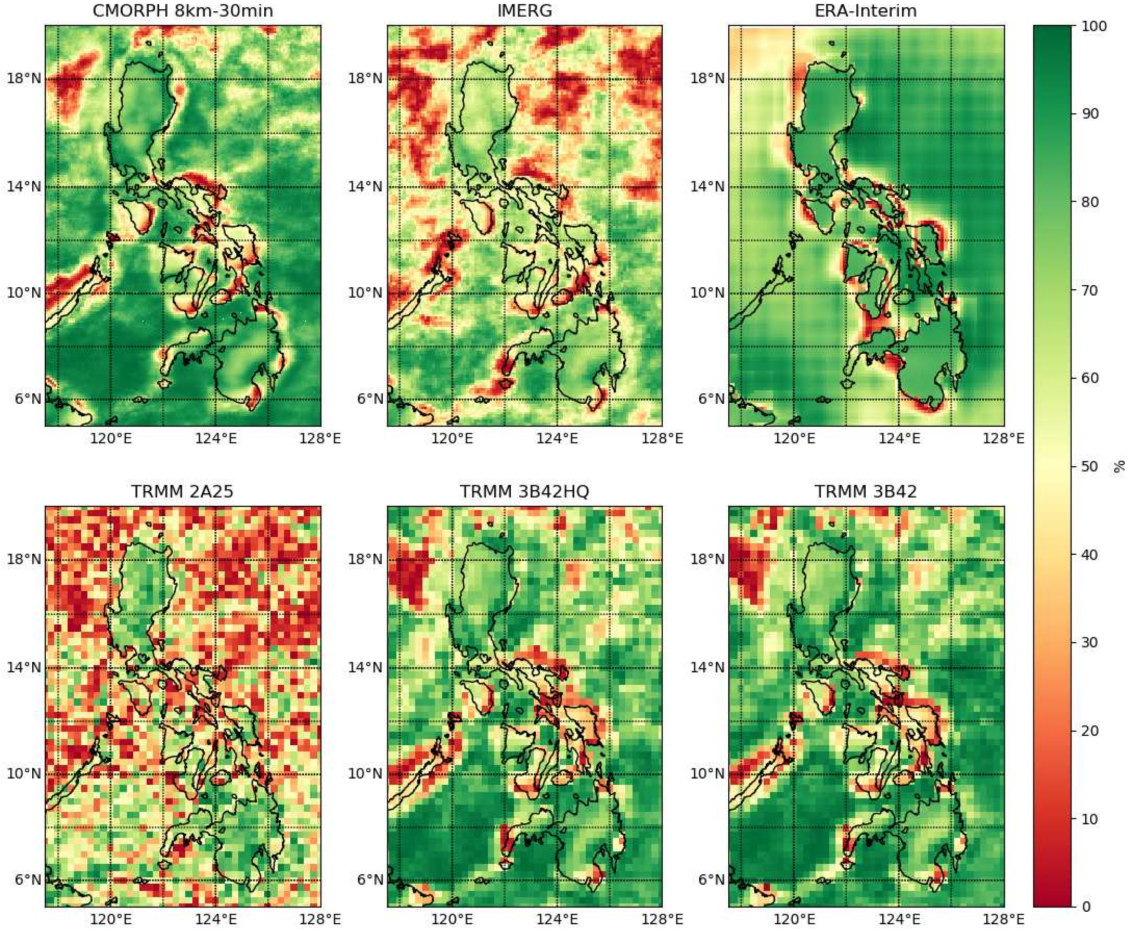

Figure 2.13: Percent variance in the May-October composite diurnal cycle explained by the first diurnal harmonic, from CMORPH (top-left), IMERG (top-middle), ERA-Interim (top-right), TRMM 2A25 (bottom-left), TRMM 3B42 High Quality (bottom-middle) and TRMM 3B42 with Infrared (bottom-right).

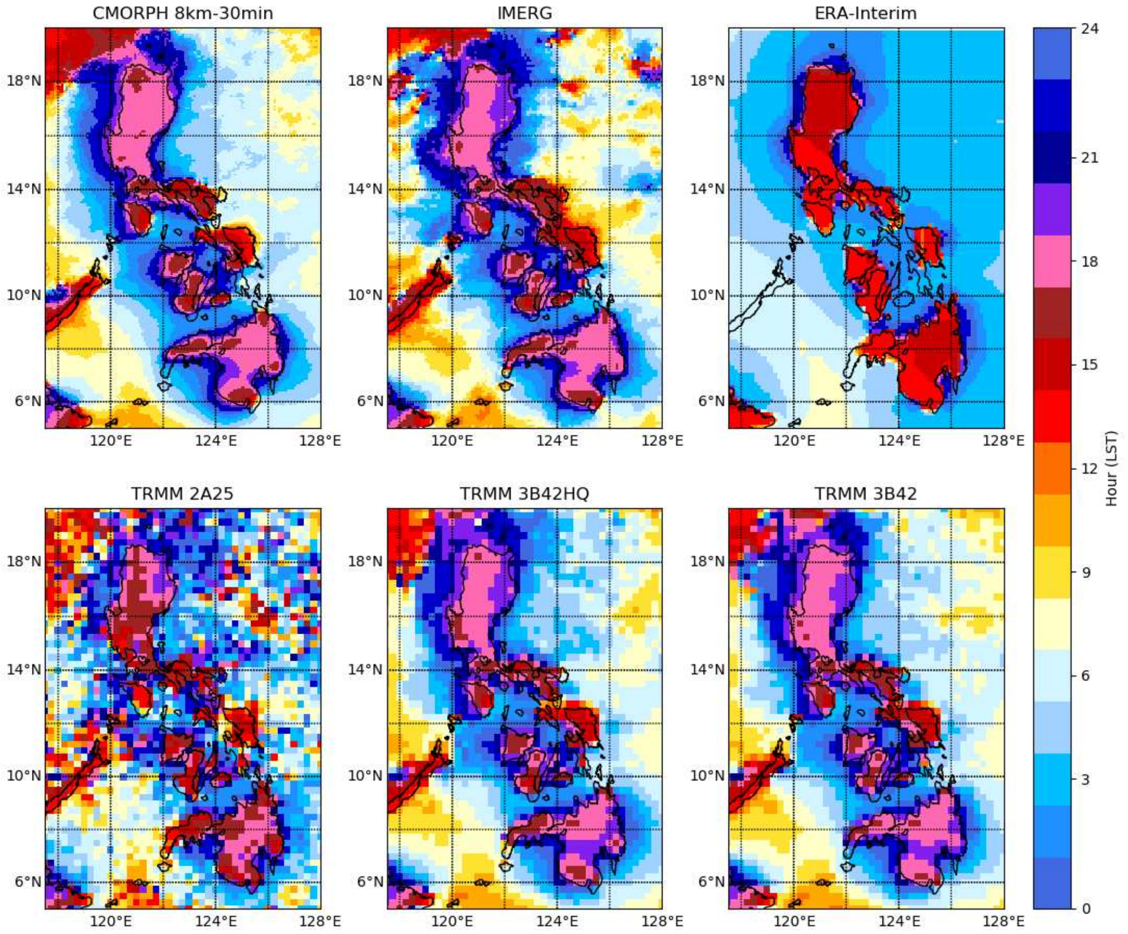

Figure 2.14: Hour of peak precipitation rate in Local Solar Time (LST) as estimated by the first diurnal harmonic of the May-October composite diurnal cycle, from CMORPH (top-left), IMERG (top-middle), ERA-Interim (top-right), TRMM 2A25 (bottom-left), TRMM 3B42 High Quality (bottom-middle) and TRMM 3B42 with Infrared (bottom-right).

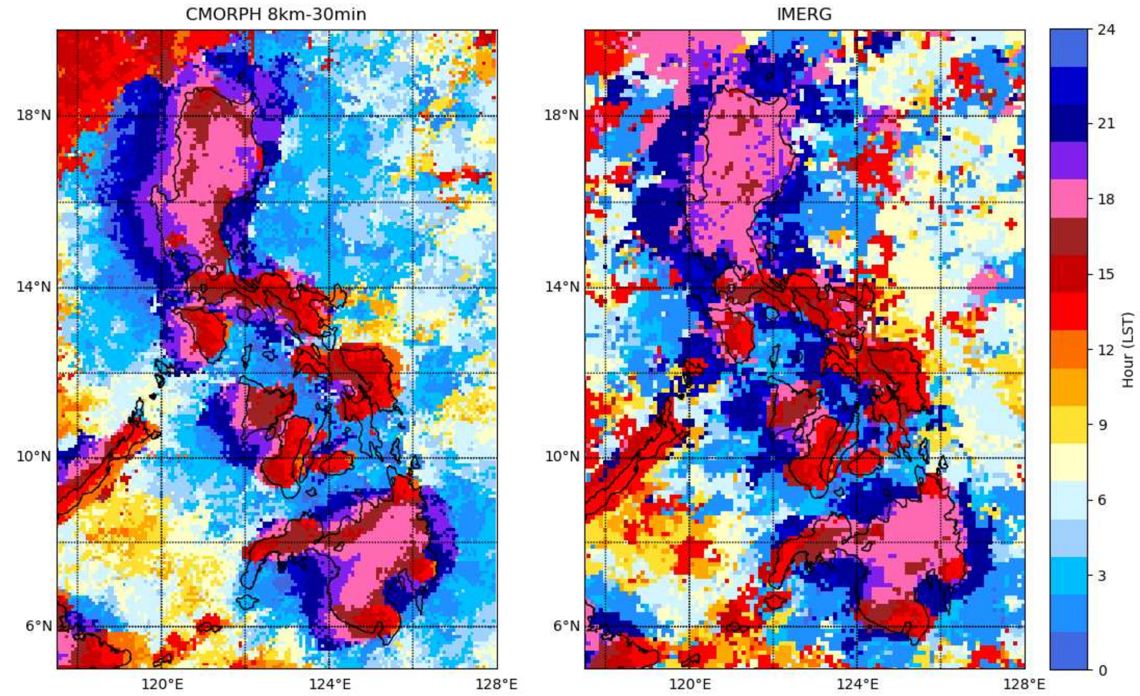

Figure 2.15: Hour of peak precipitation rate in Local Solar Time (LST) from May-October composite diurnal cycle, from CMORPH (left) and IMERG (right).

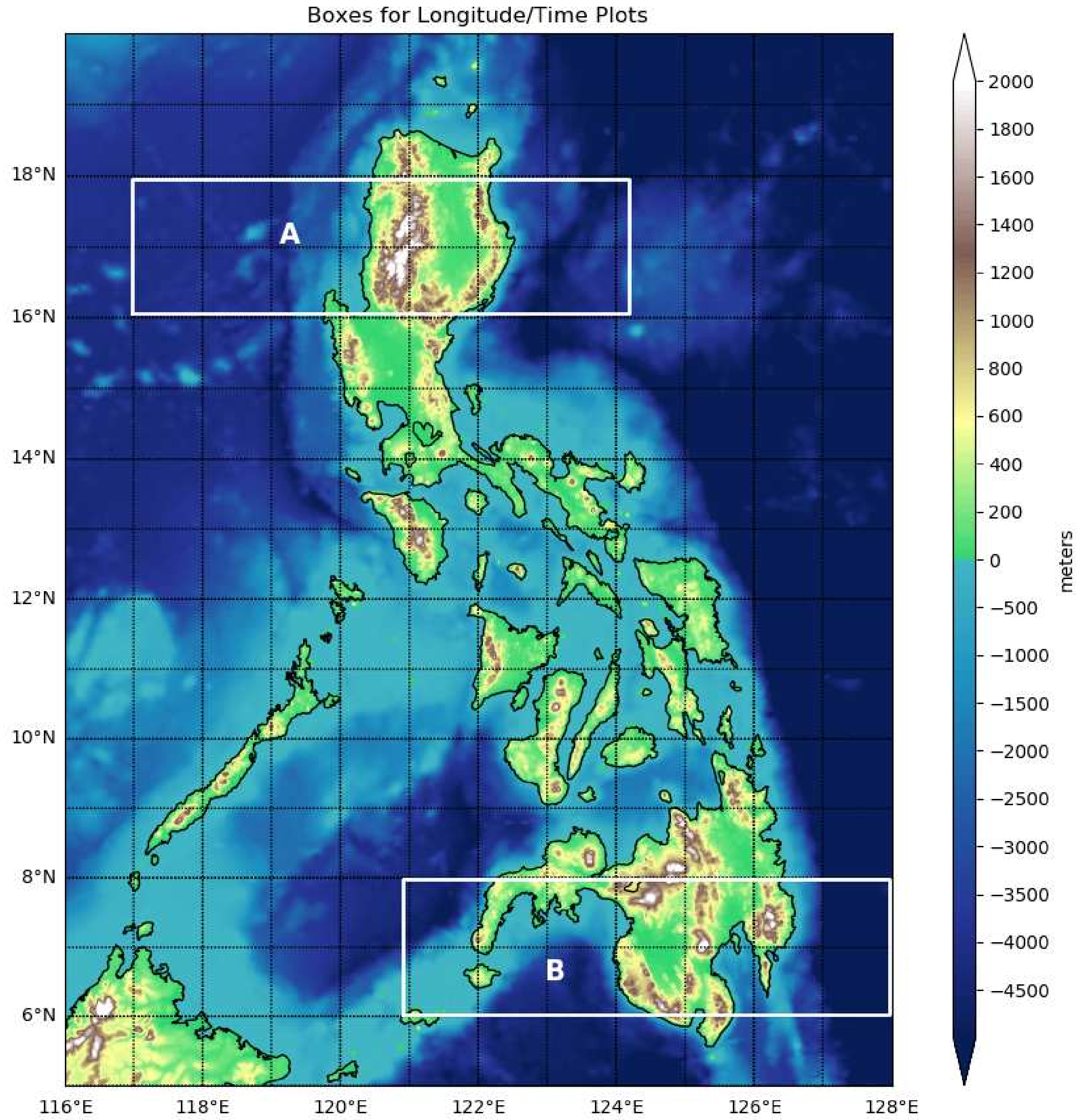

Figure 2.16: ETOPO2 topography and bathymetry (in meters) with boxes indicating the averaging latitudes for longitude versus time of day plots shown in this and successive chapters.

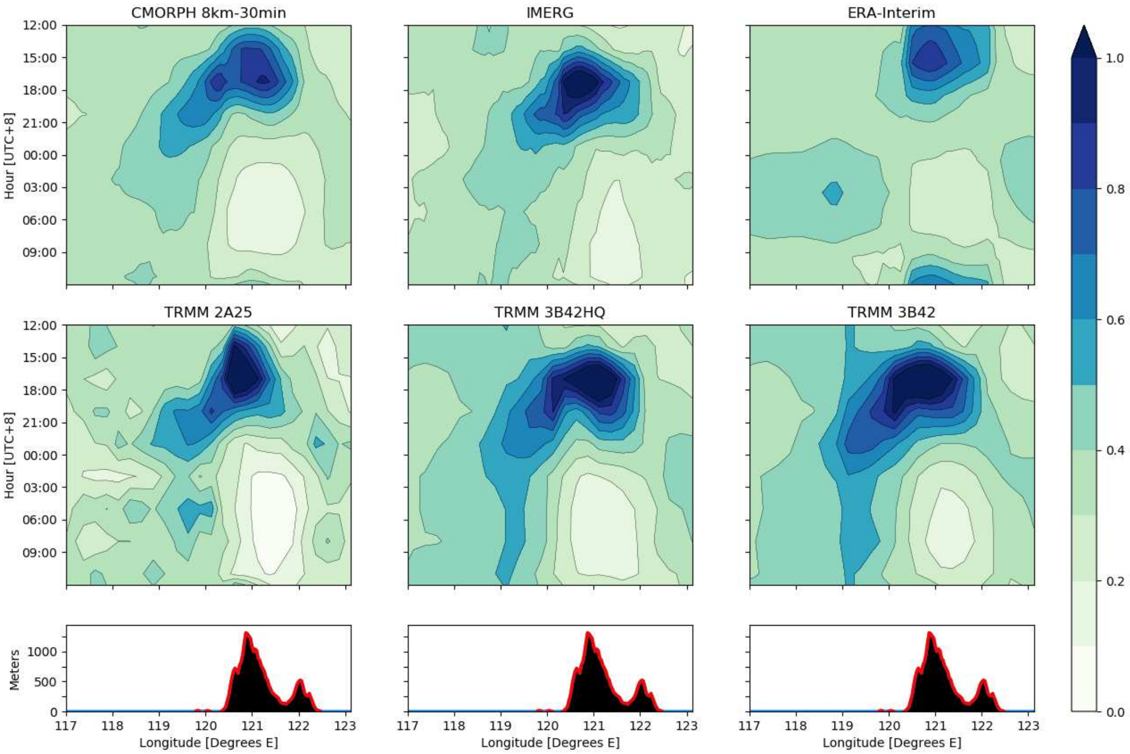

Figure 2.17: Latitudinally averaged (16°-18°N; box "A" shown in Figure 2.16) precipitation in mm hr^{-1} as a function of longitude (x-axis) and time of day in Manila, Philippines (y-axis, increasing downward) from CMORPH (top-left), IMERG (top-middle), ERA-Interim (top-right), TRMM 2A25 (bottom-left), TRMM 3B42 High Quality (bottom-middle) and TRMM 3B42 with Infrared (bottom-right), with average topography plotted below.

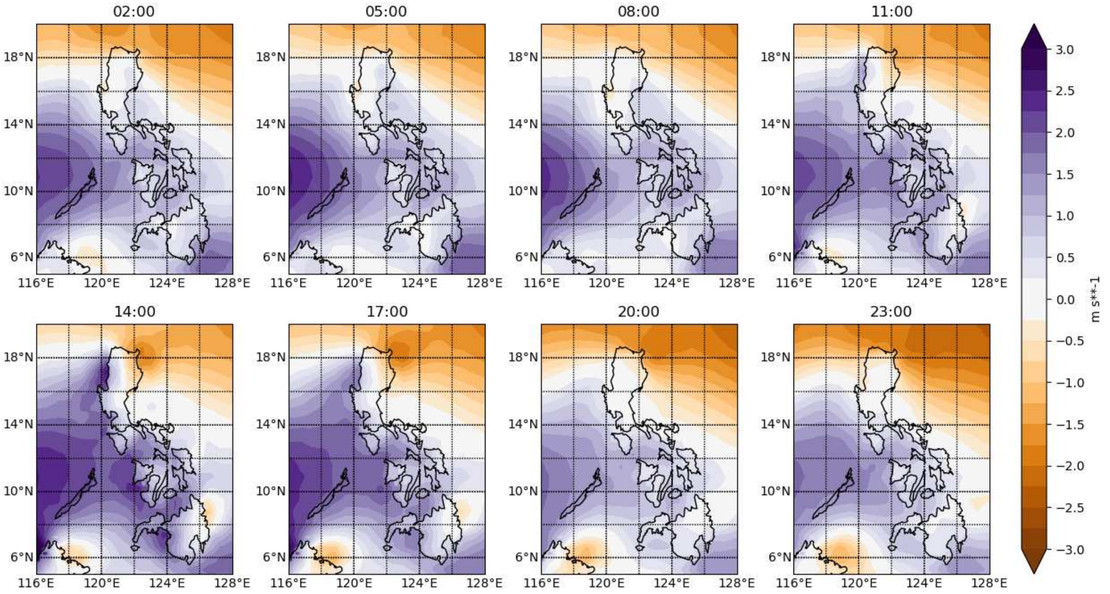

(a) ERA-Interim

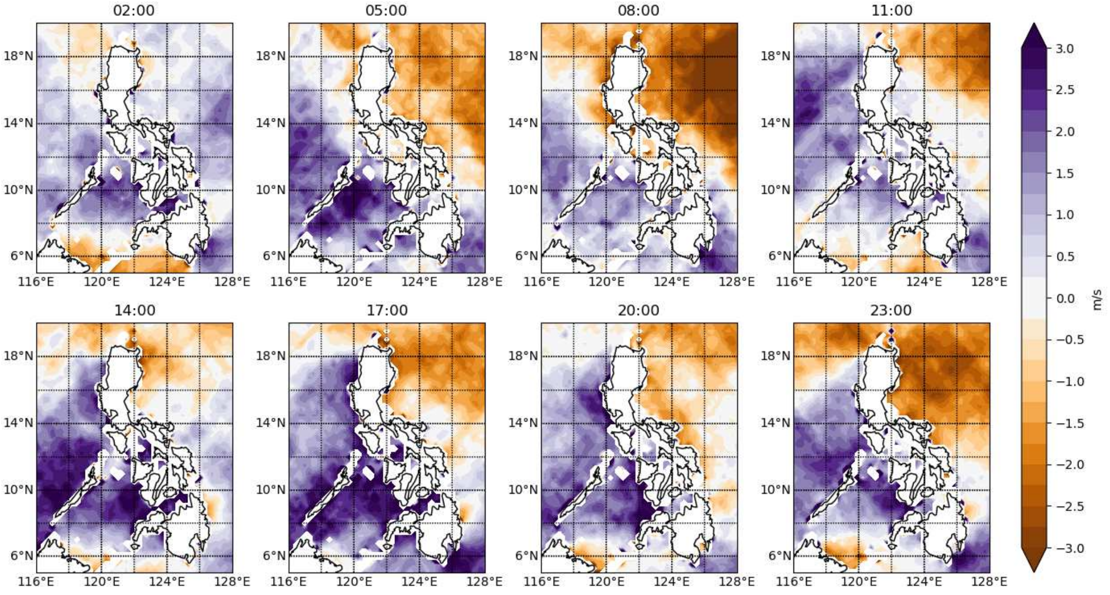

(b) RapidScat

Figure 2.18: The composite May-October diurnal cycle of zonal wind in m s^{-1} by time in PHT, from ERA-Interim (top), and RapidScat (bottom).

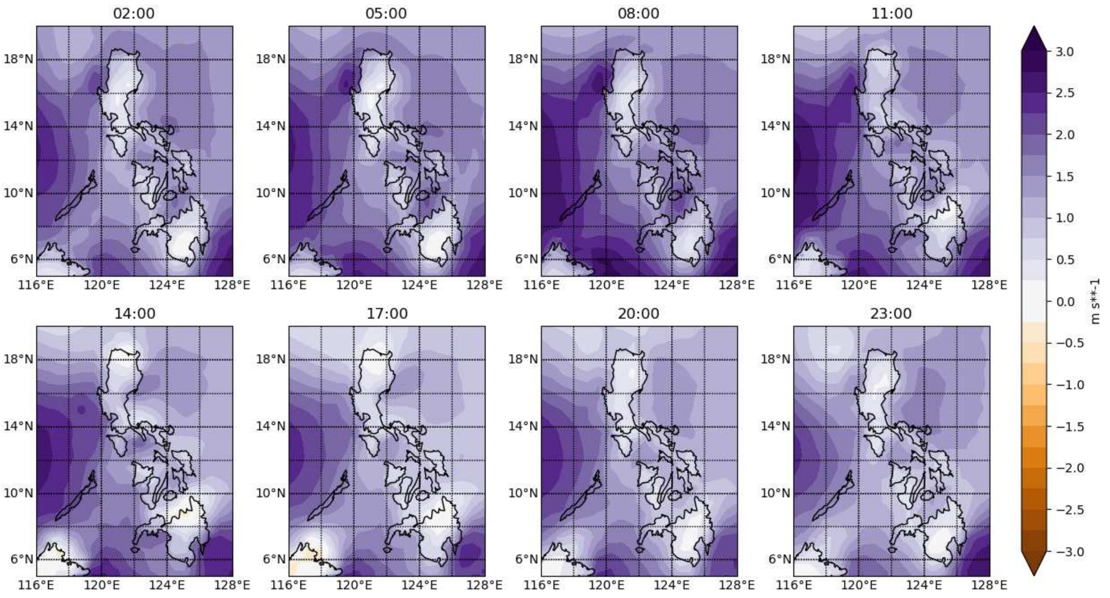

(a) ERA-Interim

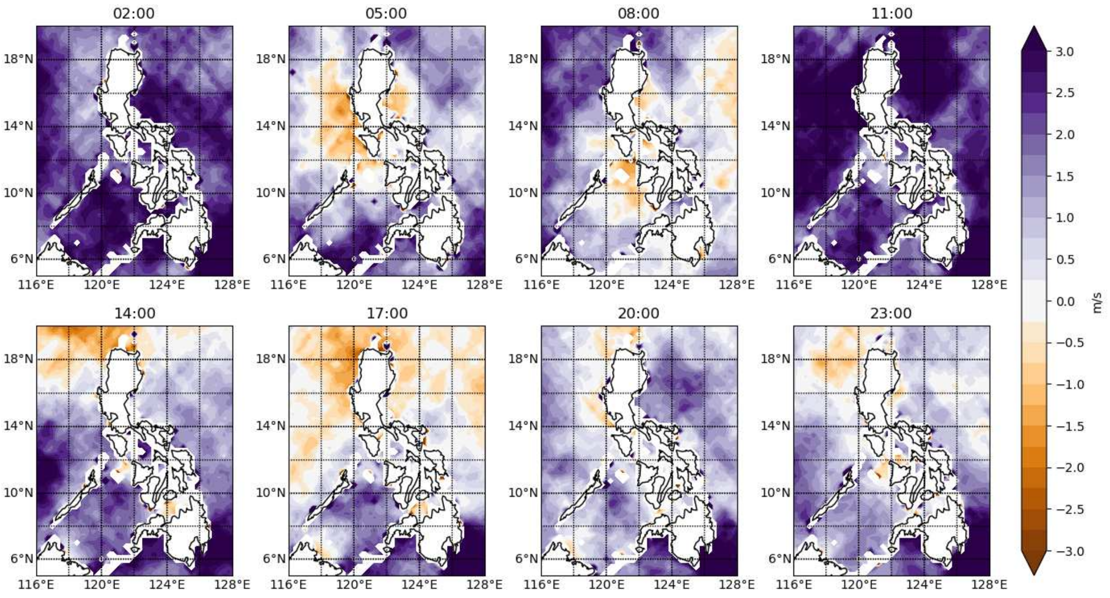

(b) RapidScat

Figure 2.19: The composite May-October diurnal cycle of meridional wind in m s^{-1} by time in PHT, from ERA-Interim (top), and RapidScat (bottom).

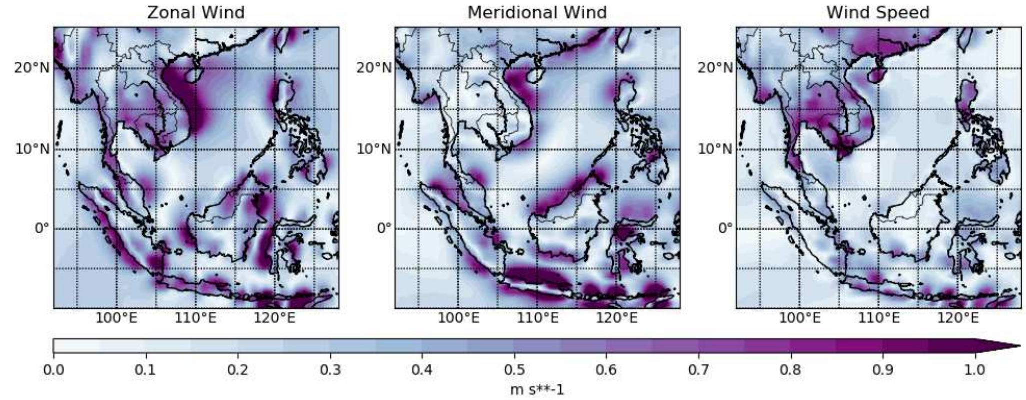

(a) ERA-Interim

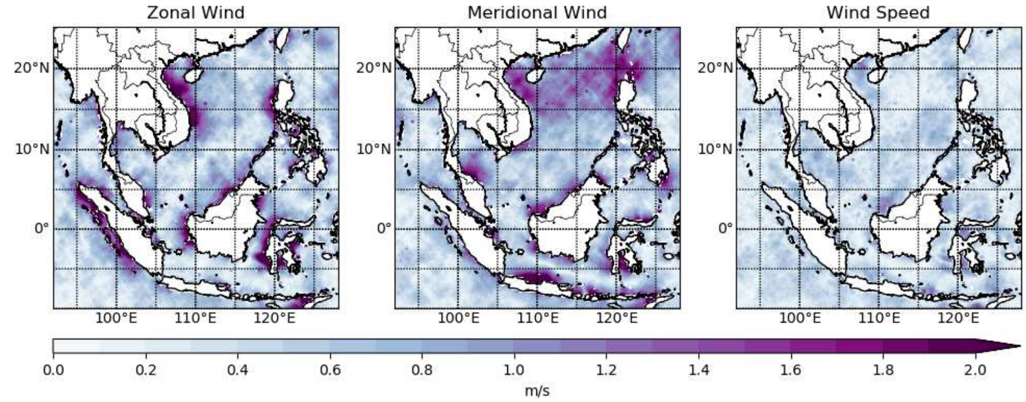

(b) RapidScat

Figure 2.20: The amplitude of the first diurnal harmonic of the May-October composite diurnal cycle in m s^{-1} from ERA-Interim (top) and RapidScat (bottom).

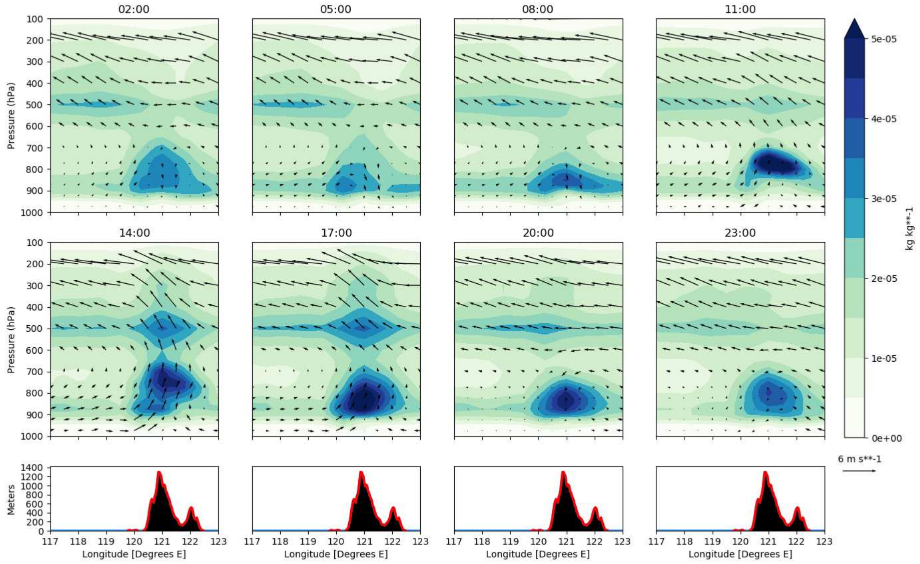

(a) Composite Diurnal Cycle

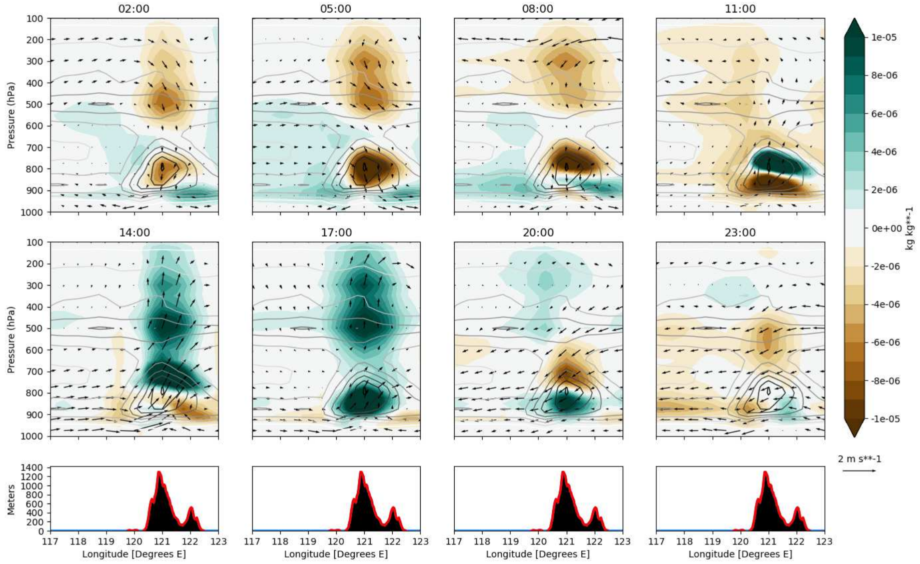

(b) Anomalies from Daily Mean

Figure 2.21: Latitudinally averaged (16°-18°N; box "A" shown in Figure 2.16) cloud total water content in kg cloud water per kg atmosphere, as a function of longitude (x-axis) and pressure (y-axis, hPa) from ERA-Interim Re-forecasts. Averages at each hour of the day (in PHT) from May-October are shown in (a), and anomalies from the daily mean are shown in (b) in colors, with the daily mean shown in contours at intervals of 5×10^{-6} kg kg^{-1}, with average topography over the same latitude band (in m) plotted below for convenience.

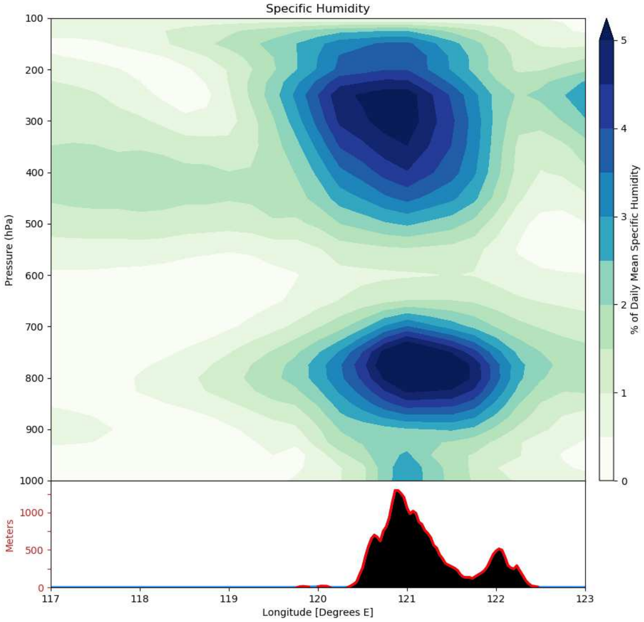

(a) Amplitude

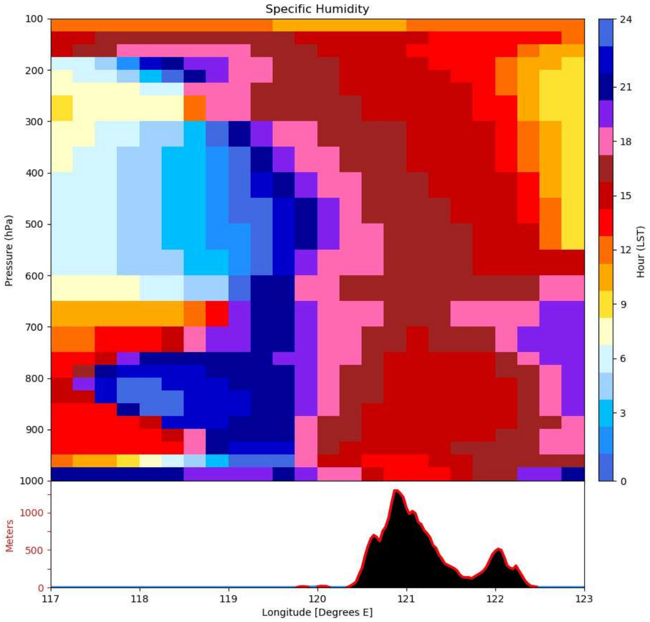

(b) Peak Hour

Figure 2.22: The amplitude (a) in units of percent of daily mean specific humidity of, and hour of peak (b), in Local Solar Time, of the first diurnal harmonic of the boreal summer composite diurnal cycle of latitudinally averaged (16°-18°N; box "A" shown in Figure 2.16) specific humidity, as a function of longitude (x-axis) and pressure (y-axis, hPa) from ERA-Interim Re-forecasts, average topography over the same latitude band (in m) plotted below for convenience.

Chapter 3

BSISO Diurnal Cycle

3.1 Data and Methods

In this chapter, the impact of the BSISO on precipitation near the Philippines and SCS will be examined with a particular focus on the diurnal cycle. While many of the datasets and methods used in this chapter have already been described in Section 2.1, one new dataset and several new methods must be introduced here. Outgoing longwave radiation (OLR) will be used as a proxy for the large-scale BSISO convection, obtained at daily temporal and 2.5° spatial resolution (Liebmann and Smith 1996). This dataset was derived from the Advanced Very High Resolution Radiometer (AVHRR) and gaps were interpolated in space and time by Liebmann and Smith (1996). In this chapter, composites created for each phase of the BSISO are extensively relied upon. The BSISO indices considered are described in Section 1.3.5. One average diurnal cycle for the variable in consideration is constructed for each numbered BSISO phase, 1-8. Days included must have an index amplitude of greater than or equal to 1.0. Index amplitude for all indices is defined as:

$$Amp = \sqrt{PC_1^2 + PC_2^2}$$

where PC_i refers to the first to the ith principal component of the EOF used to calculate the index. This effectively eliminates "weak" BSISO days, that might not really be an event, but get dumped in that phase bin by projection onto the EOFs. Additionally, only boreal summer days, defined again as May-October are considered unless otherwise stated. All days are given the same weight regardless of how long the "event" lasted. The "phases" are defined by the sign and relative amplitude of PC1 and PC2 of the index. In this thesis, the Lee et al. (2013) BSISO index (henceforth, L13 index) will primarily be used, but other indices will occasionally be invoked to show consistency of results. This index is selected because of its ability to capture maximum variance in the region of interest, the South China Sea and Philippines. While the L13 index may not capture northward propagation well (S. Wang et al. 2018), results presented here are consistent across all four BSISO indices considered, so showing the index with the highest variance explained is attractive.

In order to isolate the intraseasonal signal, bandpass filters were applied on some variables in this chapter and the next when the daily mean value was of sole interest. The same bandpass filter is used in all cases, unless otherwise noted. After removing the seasonal cycle, a Lanczos filter (Duchon 1979) with 93 weights and cutoffs at 30 and 90 days was applied to the variable of interest. The end points of the time series where the full convolution could not be performed were disregarded. Figure 3.1 shows May-October composites of bandpass filtered OLR and 850-hPa wind anomalies from ERA-Interim (see Section 2.1 for dataset description). The elongated band of enhanced convection (indicated by negative OLR anomalies) can be clearly seen propagating northeastward in later phases, consistent with previous studies (e.g. Lau and Chan 1986, Lee et al. 2013). There is evidence of a cyclonic Rossby gyre at 850-hPa forced north of enhanced convection and an anti-cyclonic gyre north of suppressed convection, again in agreement with prior modeling and observational work (Gill 1980, Kemball-Cook and B. Wang 2001, Lawrence and Webster 2002).

When the diurnal cycle was of interest for a given variable (i.e. precipitation, humidity, boundary layer wind), no filtering was done. Instead, composite diurnal cycles were created for each of the eight BSISO phases and compared to the full boreal summer composite diurnal cycle. Statistics can be calculated from these composite diurnal cycles as in the prior chapter to elucidate how the diurnal cycle varies with the BSISO in comparison to the full boreal summer composite diurnal cycle.

Statistical significance is also presented for a number of these precipitation anomalies. A bootstrap was used to attempt to compare the BSISO composite diurnal cycle to an equivalent composite diurnal selected entirely at random. The number of independent BSISO events in the period of record was calculated first where an independent event refers to a period where the index goes into one phase and stays there for any number of days. For example, if the BSISO index in question goes into phase 1 today, and remains there for 5 days, that counts as one event for phase 1. It would still count as one event even if it lasted only 1 day before dissipating or moving into another phase. If the amplitude of the index drops below 1.0 or moves into another phase, the event is considered complete. Events that occurred only partially within boreal summer were still included. The total number of independent events was calculated for all 8 phases. The phase with the *smallest* number of independent events was selected for the bootstrap, providing a lower bound for a random sample size. For the L13 index in boreal summers 1998-2017, for example, phase 6 had the smallest number of independent events with 79.

A Poisson distribution was used to simulate the randomness of the length of an event. The λ selected was equal to the average number of *additional* days beyond the first, in all events. All events from all phases had an average length of 2.92 days in the L13 index, so in this case λ was equal to 1.92 days in the Poisson distribution. This yielded one random integer x for each of the 79 events, equal to the number of additional days to sample after the first. To construct the random composite, 79 start days within boreal summer were selected at random, as well as the x days following, without replacement. The events were permitted to run outside of May-October provided that they either start or end within the season. All of these randomly selected days then were averaged together to create one composite diurnal cycle. This was done 1000 times for each BSISO index considered.

The null hypothesis in this case is that the difference between the BSISO composite diurnal cycle and the full boreal summer mean composite diurnal cycle is simply due to random chance. In this thesis unless otherwise stated, "statistically significant" means that at the 95% confidence level, the null hypothesis can be rejected. The same analysis (e.g. daily mean, diurnal amplitude, etc.) is performed on each of the 1000 random diurnal cycles and compared to the eight BSISO composites to find when and where the values from the BSISO composites are outside of 95% of the values from random composites. When considering significance of any spatial averages, the same spatial averaging is done to the 1000 random composites before comparing them to the BSISO composite.

3.2 Modulation of Philippine Precipitation

3.2.1 Daily Mean Precipitation

Before discussing the influence of the BSISO on the diurnal cycle, the modulation of precipitation in the daily mean sense over the broader MC region will be considered in this section. Figure 3.2 shows the anomalies in daily mean CMORPH precipitation rate by BSISO phase. On the large scale, precipitation appears to track OLR (as shown in Figure 3.1) very closely, particularly over the ocean. Anomalies are also statistically significant at the 95% confidence level over much of the map. Over land, anomalies are generally weaker compared to surrounding ocean but still present. Additionally, there is some evidence of an enhancement of precipitation over Sumatra, Borneo, and Mindanao prior to the arrival of the main BSISO convective envelope (tracked with OLR), consistent with previous work (Peatman et al. 2014, Sakaeda et al. 2017, Xu and Rutledge 2018).

While this gives an overview of precipitation behavior, more interesting features can be highlighted with a focus on a smaller region. Figure 3.3 shows the same information shown in Figure 3.2, but zoomed in on the Philippines to get a better look at some small scale features. It can be seen that Luzon does not follow its surrounding ocean. Statistically significant anomalies in daily mean precipitation are only found in one phase over the island. Further south, Mindanao does see some signal with enhanced precipitation in phases 1, 3, and 4, and suppressed precipitation in phases 6-8, generally out of phase with the OLR anomalies in Figure 3.1. However, this signal is weak compared the surrounding ocean. Results for Luzon differ somewhat what has been found in the boreal winter season over Sumatra, Borneo, and New Guinea (Peatman et al. 2014, Birch 2016, Vincent and Lane 2016), which generally showed elevated daily mean precipitation in the lead-up to the active phase. For Luzon, this lead-up corresponds to phases 3-4, while the lead up is phases 2-3 for Mindanao, where there is evidence of elevated daily mean precipitation. Over ocean, results are consistent with what has been established in boreal winter season near the equator, with precipitation in phase with the large-scale feature. In the enhanced phases, the SCS and Philippine Sea observe precipitation rates increased by as much as 10 mm day^{-1}, which is large considering the average precipitation rates from Figure 2.4 are only around 10-15 mm day^{-1} for the SCS, and 5-10 mm day^{-1}in the Philippine sea. In the suppressed phases, these regions see precipitation rates suppressed by 50% to nearly 100% indicating a robust modulation of precipitation over the ocean.

3.2.2 Precipitation Probability

The question of exactly how these anomalies in precipitation are manifest will now be addressed. How often and how hard does it rain in each phase? How likely are extreme precipitation events? How consistent is this pattern from one event to the next? This section will discuss the first question. Figure 3.4 and Figure 3.5 show the average frequency and intensity of CMORPH precipitation in all 3-hour periods on days when the L13 index amplitude was greater than 1.0. The BSISO signal in precipitation frequency is striking. Only 20-30% of all three hour periods in the suppressed phases observe precipitation. However, precipitation probabilities in the enhanced phases exceed 50% for the Sulu Sea and SCS, and hover around 40-50% for the Philippine Sea. Landmasses, on the other hand, experience a more modest intraseasonal modulation of precipitation frequency. Luzon typically observes precipitation in about 30-40% of all 3-hour periods, with a slight bump to near 45% for the enhanced phases, and a drop to a bit over 25% at its minimum in the suppressed phases. A similar signal is seen over Mindanao, with precipitation becoming more likely about one phase earlier than Luzon, and precipitation probabilities generally slightly higher than for Luzon overall.

Conditional precipitation rate is shown by BSISO phase in Figure 3.5. The largest signal in precipitation intensity appears to be over the Philippine sea, oscillating from about 0.5-0.8 mm hr^{-1} in the suppressed phases, to near 1.5 mm hr^{-1} in phases 6 and 7. The SCS also observes a notable increase in precipitation intensity in the active phases, but the amplitude is smaller than the Philippine Sea. This pattern is likely related to an increased preference for deep convection and MCSs in the active phase over ocean (Chen and Houze 1997, Xu and Rutledge 2014, 2018, Powell and Houze 2015). Conversely, the suppressed period is more dominated by shallow convection and thus weaker precipitation rates. Over land, a different pattern emerges. Upon close examination of

Luzon and Mindanao, it appears that the highest precipitation intensities are actually found in the suppressed phases, especially noticeable for Mindanao. However, the amplitude of this modulation is fairly small, consistent with results from Borneo by Kanamori et al. (2013). To summarize, the frequency and intensity of precipitation over open ocean both increase with the active BSISO phase with an increased frequency of deep convection and MCSs that both cover a larger area and feature heavier precipitation (Yuan and Houze 2013). The signal over land is weaker with a slight preference for less (more) frequent, more (less) intense rainfall in the suppressed (enhanced) phases.

3.2.3 Probability of Extreme Events

Figure 3.6 shows the relative change in probability from the full boreal summer probability, of high magnitude precipitation events, defined as in section 2.1 as an average precipitation rate of greater than 5 mm hr^{-1} for a 3-hour period. A value of 50% in phase 1 means that a 3-hour period with extreme precipitation on a given day classified as BSISO phase 1 is 50% more likely than it is on any random boreal summer day. Over ocean, the behavior appears as expected. During the suppressed phases (1-3), extreme events over the SCS and Philippine Sea are about half as likely. Similarly, in the enhanced phases, extreme precipitation events occur with about two times the frequency as on any random day. Thus, these high magnitude events over the ocean are about four times as likely in the enhanced phases compared to the suppressed phases.

Landmasses, particularly Mindanao, behave differently. Extreme precipitation events are most likely over the island of Mindanao in phases 1 and 3, with slight enhancement in 2 and 4. Furthermore, extreme precipitation is less likely over the island when the envelope of enhance convection is strongest, in phases 5-7. In chapter 2 it was shown that for landmasses, these types of events are significantly more likely during the afternoon and evening peak of the diurnal cycle with almost zero probability of occurrence outside of those hours. It is argued below that for the islands of the Philippines, the diurnal cycle is enhanced prior to the arrival of enhanced convection, which leads to the increased probability of extreme precipitation in these BSISO phases. Similarly, when large-scale BSISO convection is present, the diurnal cycle begins to be suppressed, thus making these events less likely. This point will be supported in later sections of this chapter.

3.2.4 Consistency Across Events

While composite anomalies have been shown to be present and statistically significant, composites don't address the consistency of results from event to event. This question will be addressed in this section. A pattern in precipitation has been established, but how often does this actually occur? Are these results being biased by a few highly significant events, or is this something seen consistently from one event to the next? Figure 3.7 shows the probability of any given day having a daily mean precipitation greater than or equal to the average daily mean precipitation rate in all of May-October, conditional on L13 BSISO phase. In other words, all days in L13 phase 1 were extracted to calculate the fraction of those days with a daily mean precipitation rate greater than or equal to the daily mean precipitation rate from all boreal summer days. Since precipitation is highly skewed, it is expected that most points will see probabilities of under 50%. Figure 3.7b shows these values as a relative change in probability from the probability on all boreal summer days.

Strong modulation of this field indicates relatively good consistency across events. Over the SCS, the suppressed BSISO phases see generally less than a 10% chance of above average daily mean precipitation rates, while this jumps to 30-50% of all days when the BSISO is in phases 5-7. Thus, the oceanic regions are nearly 4 times as likely to see elevated daily mean precipitation rates compared to a day in the suppressed phases. Over land, a similar pattern to that observed in the prior subsections emerges. Generally, the odds of increased daily mean precipitation (likely largely due to an elevated diurnal cycle) are highest in the suppressed phases, and decline in the enhanced phases. While this signal is quite minimal for Luzon in this field, it is more robust for Mindanao. Mindanao sees probabilities of 30-50% for above average precipitation rates in phases 1-2, but this drops to 10-20% in phases 6-7, indicating about 2-3 times higher probability of a rainier than normal day in the suppressed phases. This plot suggests that precipitation modulation by the BSISO is much more consistent from one event to the next over Mindanao compared to Luzon. However, in the following sections, it will be shown that a signal is present over Luzon as well. These results are consistent with those of Sakaeda et al. (2017) in that the modulation over land is less systematic than over ocean.

3.2.5 Diurnal Cycle Amplitude

We have claimed that the increased probability of extreme events over land during the suppressed phases is due to the BSISO modulation of the diurnal cycle, which is not in phase with the large-scale convection. Thus, the BSISO modulation of the amplitude of the diurnal cycle will now be considered. As described in section 3.1, the amplitude of the first diurnal harmonic of the eight composite diurnal cycles constructed from each L13 phase is shown in Figure 3.8. While all phases generally still show a strong diurnal cycle over land and coastal waters, and a much weaker diurnal cycle over open ocean, closer examination at the anomalies reveal that there is significant modulation by the BSISO.

There is a strong signal in the amplitude of the diurnal cycle over the Philippines, particularly over Mindanao. Most of the island and nearby coastal waters see a robust diurnal cycle in the BSISO suppressed phases, 1-2, and in the transition phases (3-4) with amplitudes of well over 10 mm day^{-1}. Furthermore, the enhanced phases, particular the ones towards the end of the cycle (phases 6-7), have almost no diurnal cycle. In the anomalies shown in Figure 3.8b, there is a strong, statistically significant enhancement of the diurnal cycle over Mindanao in phases 1-4. Conversely, suppression of the diurnal cycle is strongly evident in phases 5-8. Interestingly, the far eastern coast of Mindanao behaves differently from the rest of the island. The eastern shore of the island behaves differently, actually observing a(n) suppressed (enhanced) diurnal cycle in phases 2-4 (6-8).

Luzon exhibits behavior very similar to Mindanao, but perhaps not quite as robust. Statistically significant enhancement of the diurnal cycle amplitude occurs on the western side of Luzon and near coastal waters, reaching a little over an amplitude of 10 mm day^{-1}, in phases 3-4. These phases make up the tail end of the suppressed period and transition towards enhanced for Luzon. Conversely, in phases 7-8 (the tail end of the enhanced period) this same region sees a significant decline in the amplitude of the diurnal cycle. Similar to Mindanao, the east side of Luzon behaves very differently compared to the west side. On the eastern shore, phases (3-5) have a suppressed diurnal cycle, concurrent with the peak amplitude on the west side. The eastern coast's strongest diurnal cycles are present at the tail end of the enhanced phases in phase 8, but modulation of the amplitude is not as strong as on the west side. It appears that the eastern and western sides of the Philippines are out of phase in terms of when each coast sees its strongest diurnal cycle. The general enhancement of the diurnal cycle over land during the suppressed and transition phase of the ISO has also been documented in many previous studies (Sui and Lau 1992, Rauniyar and Walsh 2011, Oh et al. 2012, Peatman et al. 2014, Sakaeda et al. 2017, Xu and Rutledge 2018). However, the finding of a statistically significant modulation of the diurnal amplitude is may conflict with that of Sakaeda et al. (2017), who found that this signal was statistically insignificant in boreal winter over the equatorial MC islands. Furthermore, distinct shifts in the position of the strongest diurnal cycle within MC islands was typically not considered in these studies. Ichiwaka and Yasunari (2008) did note that the strongest diurnal cycle shifts from one coast of New Guinea to the other in association with the low-level daily mean winds.

This dipole feature is especially interesting considering how the larger scale features in the daily mean sense behave. It might be expected that the eastern side of the Philippines is generally drier in the transition from suppressed to enhanced, and wetter in the transition back to suppressed. However, looking back at Figure 3.3 and Figure 3.4, the opposite holds. Elevated precipitation rates and higher probability of precipitation have a more rapid onset on the eastern side of the Philippines, with a delayed response in the SCS on the west side of the islands. This suggests that the mechanism driving the BSISO modulation of the diurnal cycle is distinct from what is driving the increase in precipitation rate and precipitation frequency over the ocean. Statistically significant modulations of the diurnal cycle are also observed in coastal waters of the South China and Sulu Seas on the west side of the Philippines. A large amplitude diurnal cycle, nearing 10 mm day^{-1}, is observed in this region in phases 3-4. In contrast, phases 7-8 see almost no diurnal cycle. In the next section, it will be shown that this pattern is related to a modulation of diurnally generated convection propagating offshore. While the focus will be on Luzon and Mindanao, it is worth noting that this pattern is seen in between as well.

While these results will not be discussed in all other products, it is noteworthy that they are remarkably consistent across all satellite-derived precipitation datasets considered in this thesis (figures not shown). Figure 3.9 shows the same results for daily mean precipitation and diurnal amplitude anomalies by BSISO phase, but derived from TRMM 3B42HQ (see section 2.1 for description). The similarities are striking between CMORPH and TRMM, indicating that the results are not unique to one precipitation dataset. Further, the results are not unique to the choice of BSISO index. Figures 3.10 and 3.11 show the CMORPH anomalies in daily mean and diurnal amplitude composited by the Kikuchi et al. 2012 index and the Kiladis et al. 2014 OLR MJO index (OMI), respectively. It is important to note that the phase numbers between indices do not correspond to exactly the same time in an intraseasonal event lifecycle. For example, OMI captures the same pattern about one phase behind L13, with OMI phase 2 most closely corresponding to L13 phase 1. The Kikuchi index runs about one half phase behind Lee's index, meaning Kikuchi phase 2 is generally halfway between L13 phase 1 and L13 phase 2.

Keeping this distinction in mind, it is evident that daily mean precipitation tracks reasonably well in all indices used. An exception is that both new indices do not see the same signal in precipitation arriving on the east side of the Philippines before the west side. Even in the signal in diurnal amplitude, the conclusions derived above are supported with different indices. The dipole of elevated and suppressed diurnal amplitudes on the west and east sides of both Luzon and Mindanao is again apparent. Furthermore, the western coastlines and much of the interior of the islands see the highest amplitudes in the suppressed phases, and in the transition to enhanced. The smallest amplitude diurnal cycles are generally found in the enhanced phases, and the transition to suppressed. The signal in coastal waters suggesting offshore propagation in specific phases is also present.

In this section, it was shown argued that the diurnal cycle of precipitation is enhanced over the large islands of the Philippines at the tail end of the suppressed phase, leading the envelope of BSISO convection. Some evidence was also presented that there is enhanced offshore propagation of convection as the transition occurs from suppressed to enhanced phases. Both of these points will be explored more below.

3.3 Modulation of Offshore Propagation

In the last section, a signal in BSISO modulation of offshore propagating convection was suggested. While a statistically significant enhancement of the amplitude of the diurnal cycle west of Luzon and Mindanao during the transition to enhanced phases was demonstrated, it was not yet sufficiently shown that this is actually due to increased offshore propagation from storms that originate over land. This section aims to show that the end of the suppressed period and transition to the enhanced period is characterized by convection propagating further and longer than in the mean state.

To make Figure 3.12, the L13 BSISO composite diurnal cycles from CMORPH were averaged latitudinally over the northern half of Luzon (16°-18°N; box "A" shown in Figure 2.16) and displayed as a function of longitude and time. This type of plot clearly highlights some interesting features. As noted in Chapter 2, precipitation initiates over the higher terrain in the early-afternoon hours, and then propagate offshore during the evening and overnight hours during boreal summer. Figure 3.12 shows that this pattern is evident at least to some extent in all BSISO phases. However, there are some noteworthy differences. In phases 1 and 2, the mountain ranges see a robust diurnal cycle, with some evidence of weak offshore propagation both east and west. In this period, convection weakens rapidly after leaving land, dissipating before midnight within about 100-km from shore. Precipitation is generally weak over ocean at all times of the day. In the transition to the active BSISO (phases 3-5), things start to change. The precipitation maximum over Luzon is further enhanced, and propagating convection maintains strength longer and further offshore. Average precipitation rates are over 1 mm hr^{-1} well offshore during the late evening hours in phases

4 and 5. Furthermore, there is evidence that convection continues to propagate out to nearly 117°E at sunrise the next day. The offshore propagation signal becomes more muddled in phase 6. Precipitation rates are high at all times of day over the Luzon and the SCS, dwarfing the offshore propagation signal. As the active phase begins to wind down (phases 7-8), there is little to no evidence of offshore propagation on the west side of Luzon. Precipitation rates remain generally constant throughout the day. There is some evidence of offshore propagation to the east of Luzon, but it is weaker than that during earlier phases on the west shore.

The anomalies from the full May-October composite diurnal cycle, shown in Figure 3.13, reveals further detail. The boreal summer composite is shown in black and white contours with BSISO anomalies superimposed in color. Additionally, statistical significance of these anomalies is shown with dots corresponding to the bootstrap test described in section 3.1. For the SCS (west of 120°E) and the Philippine sea (east of 123°E), the early suppressed phases (1 and 2) tend to be accompanied by anomalously low precipitation rates at most times of the day. Similarly, the active BSISO period exhibits elevated precipitation rates at all hours of the day. Over land, dry anomalies are found at all times, with the exception of the eastern side of Luzon right before and during the average peak of precipitation at around 15:00-18:00. Statistically significant increases in precipitation rate during the afternoon peak with dry anomalies at other times indicate a strong diurnal cycle on the eastern side of the Cordillera Central. In phase 2, this elevated diurnal cycle shifts slightly westward to the peak of the mountain range.

The westward shift continues in phase 3, when precipitation is enhanced from the Cordillera Central to the west coast during the afternoon peak, and lower than average at all other times of day, again indicating an elevated diurnal cycle. The dipole pattern mentioned before is evident here, with peak precipitation on the eastern side of the island now well below average. In phase 4, the peak precipitation anomaly over the western side of Luzon appears to propagate out to sea, elevating precipitation rates in the late evening hours up to about 50-km offshore. Further out to sea (118°-119.5°E), precipitation is anomalously low at all times of the day, *except* the times of the late evening and overnight hours when those points are affected by offshore propagating systems. In the transition to the active BSISO period in phase 5, there is robust evidence of statistically significant increases in precipitation rates during the typical peak hour over the Cordillera Central and offshore to nearly 300-km. The anomalies propagate westward with the average diurnal cycle, indicating an increased tendency toward stronger diurnally generated convective systems that propagate further offshore until later into the night.

As the active phase becomes established and then begins to wane in phases 6-8, elevated precipitation rates initially occur all longitudes and all times of day. There is a notable exception over the island during its peak time frame where wet anomalies are not found. In fact, even though the surrounding seas are still recording predominantly higher precipitation rates at all times of day in phase 7, a statistically significant dry anomaly is found during the afternoon peak over land. This indicates a weakened diurnal cycle, but not necessarily lower daily mean precipitation values since precipitation is elevated at all other times of day. Phase 8 looks similar, with an interesting increase in precipitation rates on the east side of Luzon, and even some evidence of increased offshore propagation to the east. However, in addition to a suppression of the diurnal cycle over land on the west side of Luzon, there is evidence of the same in the SCS waters.

The diurnal cycle over Luzon has been thoroughly described and now it will be examined whether similar behavior exists in other regions, i.e. Mindanao. Figure 3.14 shows the same analysis as Figure 3.12 for Mindanao, latitudinally averaged from 6°-8°N (see box "B" in Figure 2.16). It is important to note that the topography shown is the average topography, and the geography of Mindanao is slightly more complex than Luzon. Even though non-zero topography is shown from 122°-124°E, this corresponds to the Moro Gulf with a section of the narrow Zamboanga peninsula included. Exclusion of this small section of land does not significantly affect the results (not shown). The SCS is then west of 122°E and the Philippine Sea is east of 126.5°E. The large-scale BSISO convection impacts Mindanao about 1 phase earlier than Luzon in terms of its large-scale pattern, due to its location further south. Phases 1-2 see generally weakly suppressed precipitation over the ocean, while the afternoon peak is slightly enhanced over the island, indicating a modestly enhanced diurnal cycle. However, by phases 3-4, a robust increase in peak afternoon precipitation over land occurs, followed by consistent and coherent propagation into the Moro Gulf. This behavior in phases 2-4 over the Moro Gulf and west side of Mindanao is similar to what was observed over the west side of Luzon and eastern SCS in phases 3-5.

One difference is that the diurnal cycle over Mindanao appears to be even more dominant than it is over Luzon. While phases 5-6 are the peak of BSISO activity in this region, only moderate enhancement of oceanic precipitation occurs outside of the Moro Gulf (west of 122°E) and on the east side of the island. In phases 6-7, towards the end of the active period, Mindanao sees almost no diurnal cycle. Precipitation rates are strongly suppressed during the afternoon peak in the diurnal cycle, and thus also suppressed overnight in the Moro Gulf when offshore propagation from the diurnally generated convection is expected. The diurnal cycle amplitude increases slightly in phase 8, but is still highly suppressed. It appears to return to normal in phase 1 during the middle of the inactive BSISO period. While not shown, these results for both islands are consistent in all satellite-derived precipitation datasets, as well as in each of the four BSISO indices considered in this thesis.

In this section, it has been shown that in addition to the diurnal cycle of precipitation over land leading BSISO convection, there is a more prominent offshore propagation. Furthermore, when large-scale BSISO activity is in the vicinity, the diurnal cycle, and its influence to the west of both islands, is much weaker. These results are consistent with much of the previous work on the ISO impact on the diurnal cycle (Ichiwaka and Yasunari 2008, Peatman et al. 2014, Sakaeda et al. 2017), but also extend their analysis to study offshore propagation. More nuance is also added, regarding the disparity seen between the east and west sides of the Philippines. While there is evidence from prior work that a similar pattern occurs over Borneo and New Guinea (Ichiwaka and Yasunari 2006, 2008), this has not been as extensively documented. In the final sections of this chapter, these findings will be summarized and synthesized with an emphasis on certain regions of the Philippines. After that, a mechanism to explain these results will be proposed in Chapter 4.

3.4 Summary of the Diurnal Cycle over Luzon

In this section, the particular differences from west to east in the diurnal cycle over Luzon will be considered using the composite BSISO diurnal cycles. Figure 3.16 shows the composite diurnal cycle spatially averaged inside boxes shown in Figure 3.15. Spatial averaging was performed rather than showing a single point because satellite precipitation products tend to be more reliable when considered over a larger area (Tan et al. 2017). Figure 3.16(a) shows composites by BSISO phase for box "A" just offshore of Luzon, including only oceanic grid points. (b) shows the composite over land on the west side of topography inside box "B" (northwest Luzon), while (c) shows the east side of topography inside box "C" (northeast Luzon), both of which only included grid points over land.

The dotted black lines in each plot shows the composite diurnal cycle for all of boreal summer, while the gray bounds show the 95% confidence bounds for the bootstraps. To avoid clutter, consecutive phases are composited together. Statistical significance is calculated to account for two phases averaged together by averaging two separate random composite diurnal cycles from the bootstrap. Figure 3.17 shows the daily mean and diurnal range of each phase's composite diurnal cycle against the 95% confidence bounds. Diurnal range is shown in place of diurnal amplitude since the composite diurnal cycles (particularly in the suppressed phases over land) have a narrow peak that may not be well represented by the first diurnal harmonic. However, with spatial averaging, these diurnal cycles are sufficiently smooth to warrant use of the diurnal range.

The BSISO composites of the composite diurnal cycle over northwest Luzon shown in Figure 3.16 (b) are quite interesting. At most times of the day, precipitation is strongly suppressed in phases 1-4. However, in phases 1-2, average precipitation rates reach nearly to the May-October mean during the peak rainfall period of 15:00-21:00. Even more interesting is that phases 3-4 have precipitation rates at the high end of the 95% confidence interval, matching it between 15:00 and 18:00. In phases 5-6, precipitation rates are enhanced somewhat evenly at all hours of the day. At the tail end of the BSISO active phase, precipitation rates are significantly higher off the diurnal peak, from 21:00-15:00, but actually below the boreal summer mean during the peak. In

Figure 3.17, northwest Luzon exhibits a statistically significant increase in diurnal range in phase 3, and a significant decrease in phases 7-8. However, this behavior generally opposite the pattern seen in daily mean, which is suppressed in phases 1-3, and enhanced in phases 6-8. Daily mean precipitation tracks OLR anomalies well, enhanced when negative OLR anomalies are present, but the diurnal range is almost exactly out of phase. This result is similar to the results of Peatman et al. (2014), indicating an enhancement of the diurnal cycle in the transition to the active BSISO over Luzon. However, the diurnal cycle also determined the daily mean precipitation rate over the islands considered by Peatman, whereas these results suggest that the diurnal range and daily mean are out of phase. The major difference is an enhancement of nocturnal and morning precipitation over Luzon during the active ISO phase that was not seen over larger MC islands during boreal winter.

The same pattern is seen offshore of northwest Luzon (shown in Figure 3.16(a)), with a strong diurnal cycle in phases 3-4 peaking around 21:00. This suggests that the diurnal cycle over coastal waters is enhanced offshore concurrently with an enhancement on the west side of the Cordillera Central. While this region records elevated precipitation rates at all hours at the beginning of the active phase, it occurs such that the diurnal cycle remains relatively unchanged. The end of the active period (phases 7-8) observes almost no diurnal cycle, with constantly elevated precipitation rates at all hours. Thus, a statistically significant increase (suppression) in the diurnal cycle over coastal waters is present in phase 4 (8), as seen in Figure 3.17. Similar to the island, the daily mean precipitation over coastal waters is out of phase with the diurnal range, maximizing (minimizing) with statistically significant anomalies in phases 6-8 (1-4). Another very interesting feature observed over both land and water on the west side of Luzon (Figure 3.16(a) and (b)) is a slight modulation of the hour of peak precipitation. The inactive phases tend to see a slightly earlier peak, just 30 minutes to 1 hour earlier, while phases 7-8 see a peak delayed by about 1-2 hours over land. These results are consistent with prior studies that have indicated a preference for an earlier peak in the diurnal cycle during the ISO suppressed period (e.g. Rauniyar and Walsh 2011).

Figure 3.16(c) shows the altered pattern over eastern Luzon quite clearly. In phases 3-4, a robust, propagating diurnal cycle on the west side, a precipitation rates are dramatically suppressed during the normal afternoon peak (15:00-21:00). In fact, Figure 3.17 shows that there is a statistically significant decrease in the diurnal range on the eastern side of Luzon in phases 3-5. The strongest diurnal cycle is actually present in phases 7-8, but the change in the diurnal range is statistically insignificant. The change in timing of peak precipitation is less noticeable on this side of the island. For eastern Luzon, the diurnal range and daily mean precipitation are nearly in phase with one another, with a delay of about 1-2 phases for the diurnal range, markedly different than what was observed for western Luzon. Daily mean precipitation however, generally follows the same pattern as western Luzon, and is suppressed when large scale convection is suppressed.

3.5 Summary of the Diurnal Cycle over Mindanao

The diurnal cycle around Mindanao exhibits a behavior similar to that over Luzon, but with some important distinctions. Figure 3.18 shows the composite diurnal cycles by BSISO phase for the Moro Gulf, on the west side of the island, the central portion of the island, and the eastern portion of the island. The domains over which spatial averaging was performed for Mindanao are also shown in Figure 3.15 as boxes "D", "E", and "F" referred to as the Moro Gulf, central Mindanao, and eastern Mindanao respectively. As shown in previous sections, the diurnal cycle over the Moro Gulf is often connected to convection that initiated on the island, and propagated westward offshore. Over both of these regions, a modulation of the diurnal cycle even more robust than over Luzon is apparent.

Examination of Figure 3.18(a) and (b) indicates a strong diurnal cycle over Mindanao and the Moro Gulf in the peak of the suppressed BSISO period (phases 1-2). In the transition and beginning of the active period (phases 3-4), both regions observe a strong diurnal cycle that is well outside of the 95% confidence interval. Figure 3.19(a) and (b) show that a statistically significant increase in the diurnal range *and* the daily mean precipitation rate occur in these phases. In the late active phases and transition to suppressed (phases 5-8), the diurnal cycle is strongly suppressed, which leads to a lower daily mean precipitation rate as well. Phases 6-8 all exhibit statistically significant decreases in both the diurnal range and daily mean precipitation rate for both the Moro Gulf and central Mindanao. This is more in line with what was observed by Peatman et al. (2014) over the equatorial MC, that the diurnal cycle determines the daily mean precipitation. Contrary to Luzon though, there appears to be little evidence of any change in the timing of the diurnal cycle for these domains.

Eastern Mindanao looks dramatically different. Interestingly, there is some evidence of a change in the timing of the diurnal cycle, with earlier peaks favored in phases 1-4, and later peaks in phases 5-8, again consistent with Rauniyar and Walsh (2011). In addition, a suppressed diurnal cycle occurs in the inactive period, with the highest amplitude actually found in phases 7-8, when the central part of the island and the Moro Gulf see almost no diurnal cycle. These patterns are noisier than the other portions of the island with less statistical significance present. However, eastern Mindanao sees a statistically significant increase in the diurnal range in only phase 8, with statistically significant increases (decreases) in daily mean precipitation present in phases 3-5 (6-8).

Furthermore, differences are noted in the random variability, as indicated by the width of the 95% confidence bounds in Figure 3.18. For central Mindanao and the Moro Gulf, most of the variability is present during the afternoon peak, while the overnight and morning minimum in precipitation rate has relatively little variability. This is seen by a wider spread between the confidence bounds during the afternoon peak, and a comparatively small spread at other times. Thus, for this island, the amplitude of the diurnal cycle is the key factor in determining daily mean precipitation rate. This is different from Luzon, where the amplitude of the diurnal cycle could behave differently than the daily mean precipitation rate due to increased variability in nocturnal precipitation. Over Luzon (Figure 3.17), the spread between the confidence bounds is fairly constant throughout the day, indicating potential for more variability in nocturnal and morning precipitation. The same pattern is observed over eastern Mindanao, where the diurnal range and daily mean precipitation rate are also out of phase. These results suggest that when significant nocturnal variability is absent over land, the modulation of the diurnal cycle entirely determines daily mean precipitation. However, when precipitation rates overnight and into the morning are more highly variable, the two can be out of phase with one another. This explains the discrepancy between Luzon, Mindanao, and the equatorial MC islands observed by Peatman et al. (2014).

While not shown, compositing by any of the other BSISO indices, and use of any other satellite-derived precipitation dataset discussed in this thesis with sufficient data coverage supports the same conclusions drawn from CMORPH data composited by L13 BSISO phase. With an understanding of the BSISO modulation of the diurnal cycle established for two major islands of the Philippines in this chapter, a physical mechanism is required to explain these results. Such possible mechanisms are presented with supporting evidence in Chapter 4.

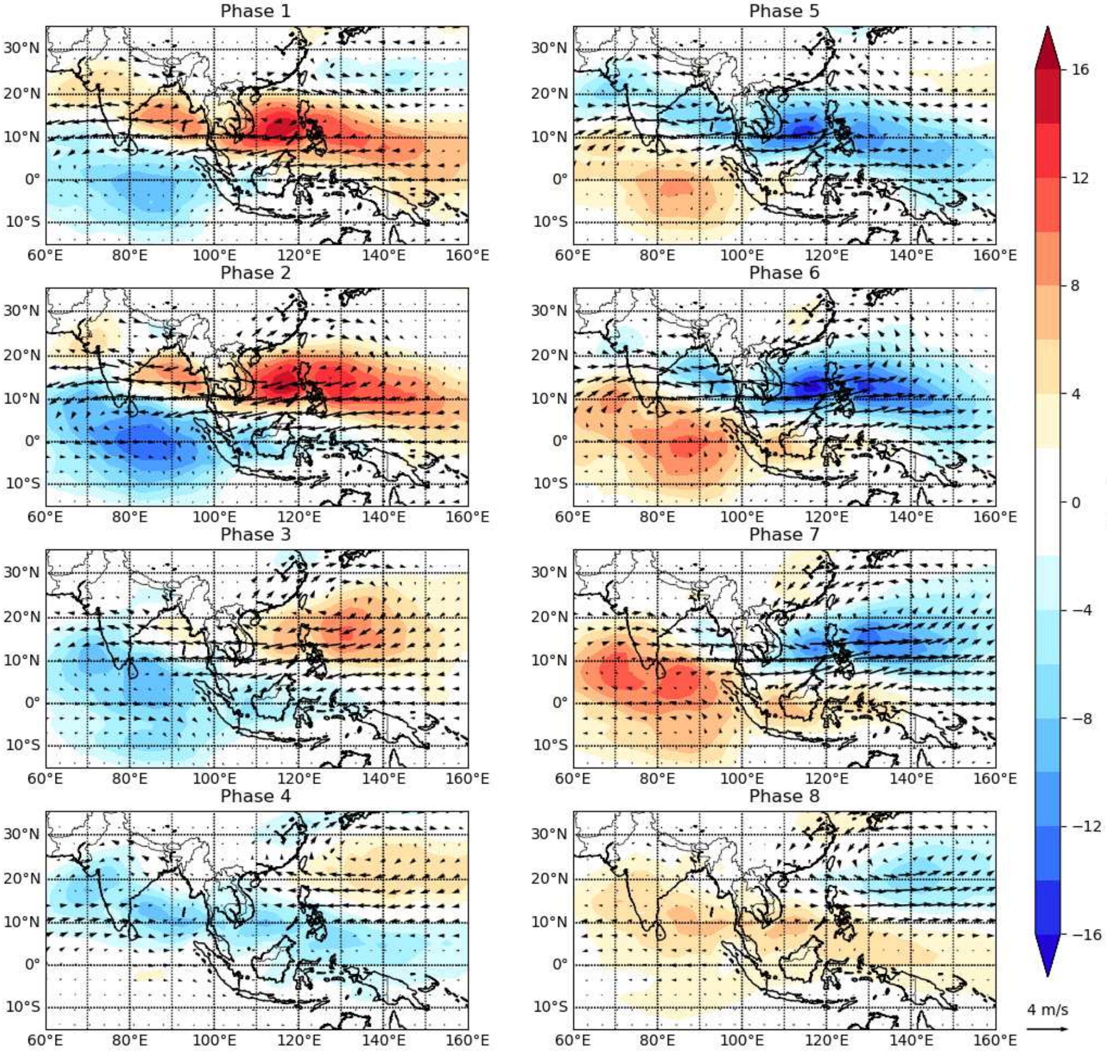

Figure 3.1: Bandpass filtered (30-90 day) anomalies in AVHRR OLR (in W m^{-2}) and ERA-Interim 850-hPa winds (vectors, ms^{-1}) by Lee et al. 2013 BSISO phase in May-October.

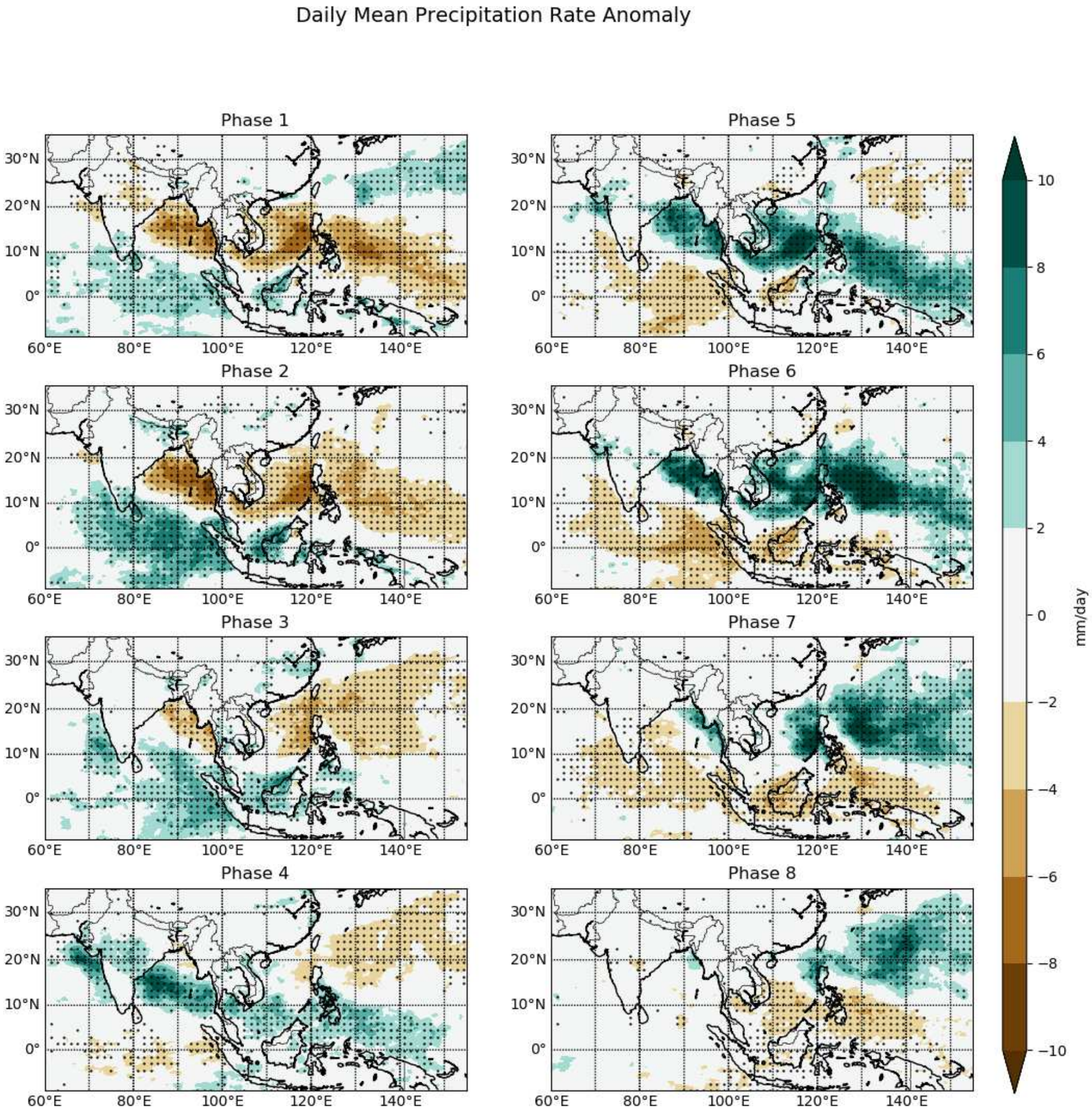

Figure 3.2: Anomalies in May-October daily mean precipitation rate (in mm day^{-1}) from CMORPH by Lee et al. 2013 BSISO phase in colors, with statistical significance at the 95% level shown in black dots.

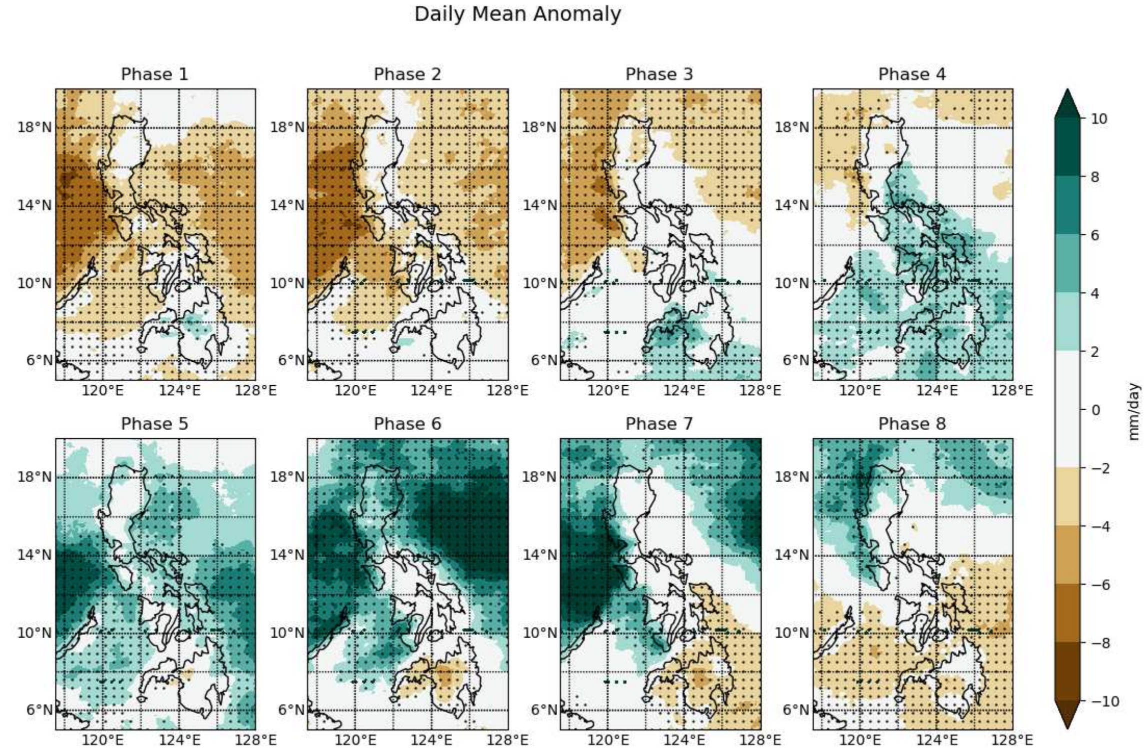

Figure 3.3: Same as Figure 3.2 but for the Philippines only, from high-resolution CMORPH.

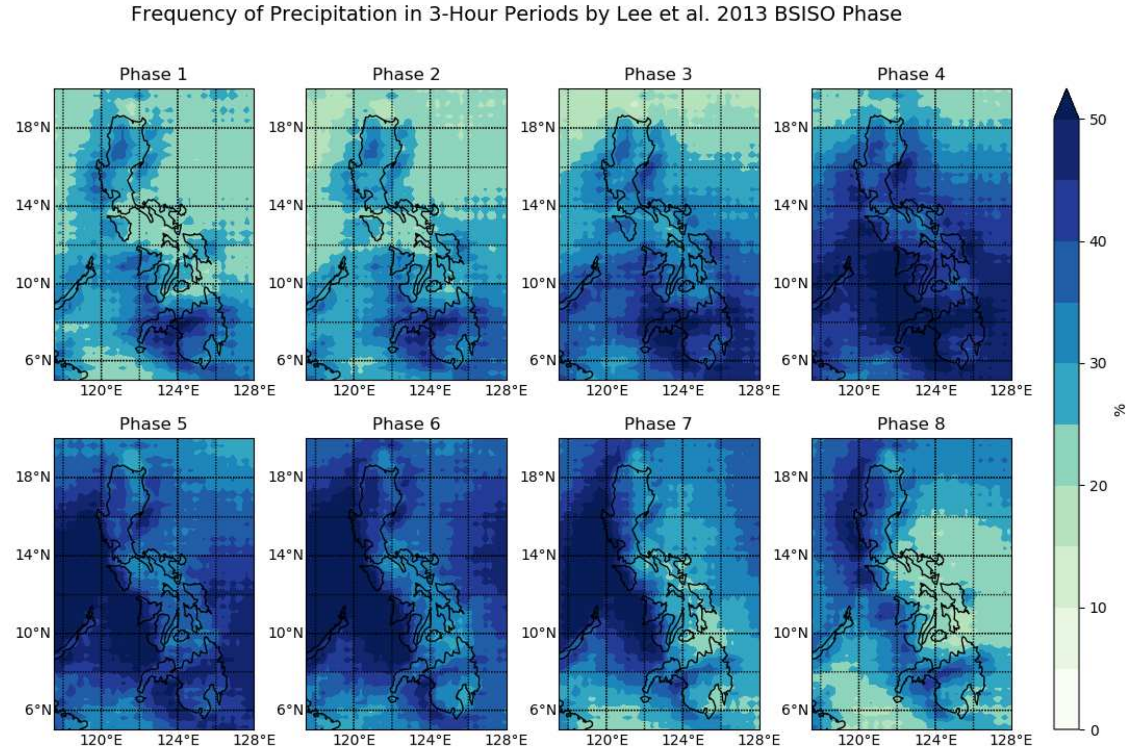

Figure 3.4: Probability of non-zero average precipitation during any 3-hour period in each BSISO phase from May-October CMORPH record.

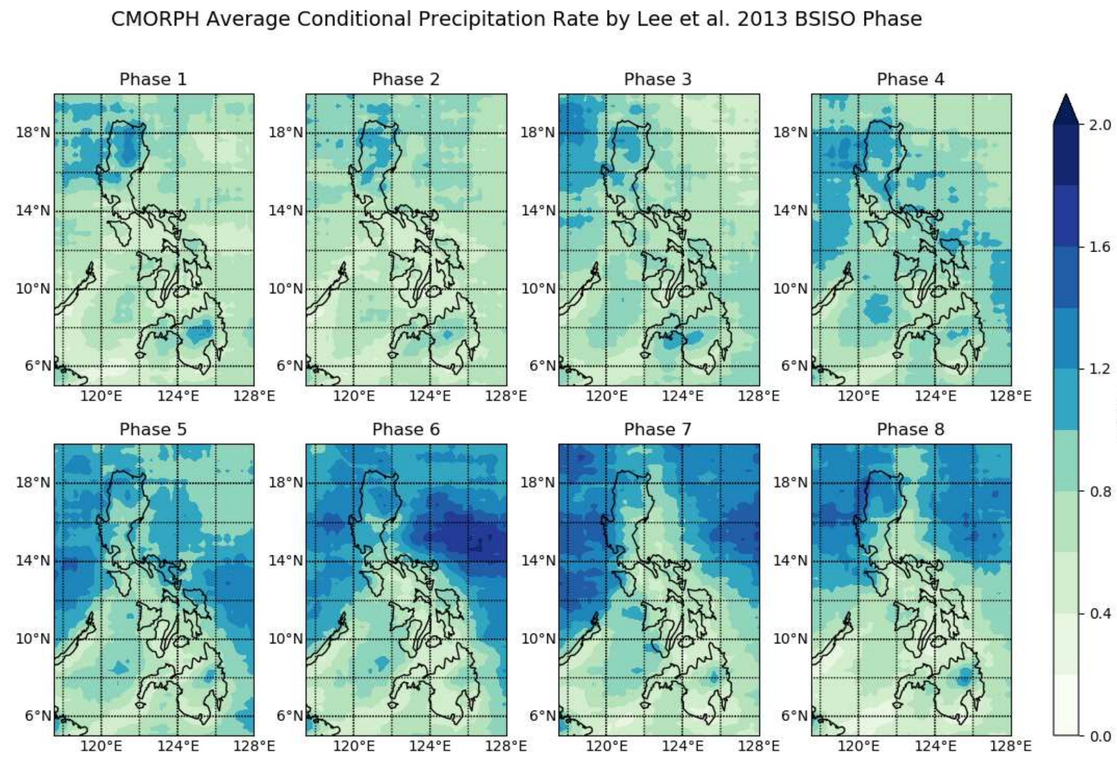

Figure 3.5: Average precipitation rate from CMORPH during 3-hour periods that have rain recorded, by BSISO phase.

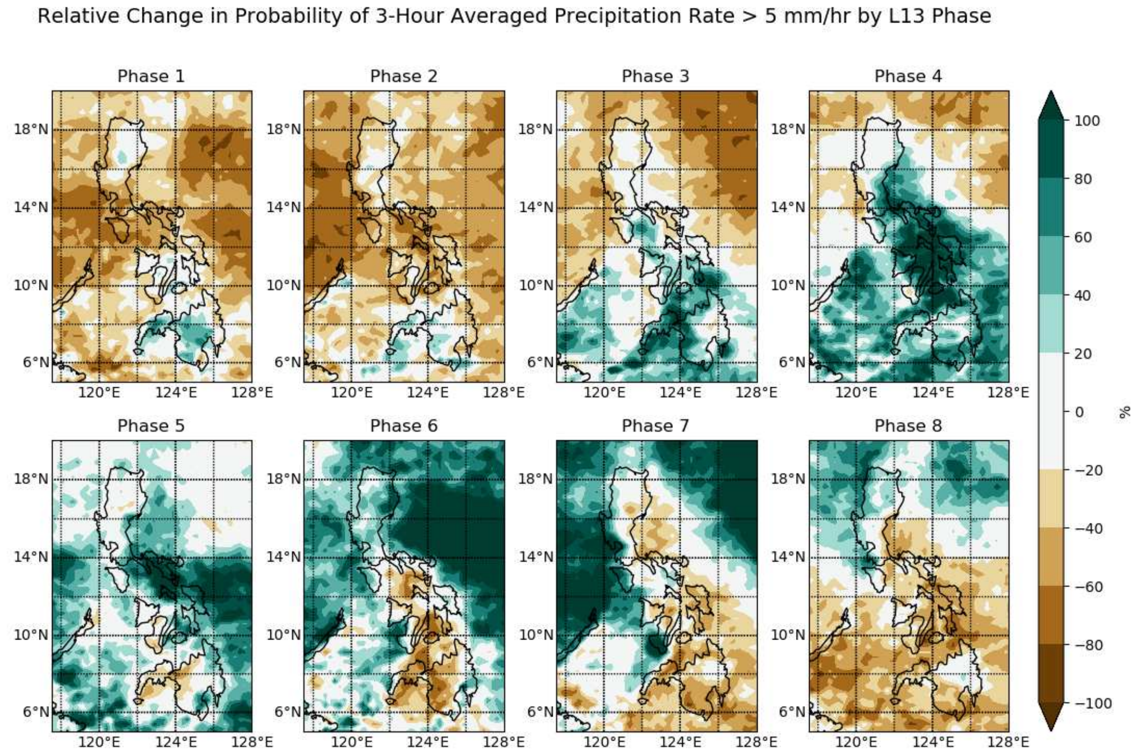

Figure 3.6: Change in probability of any given May-October 3-hour period observing an average precipitation rate of greater than 5 mm hr^{-1} (i.e. greater than 15 mm per 3 hr) by Lee et al. 2013 BSISO phase, from CMORPH.

(a) Probability of Above Average Daily Mean

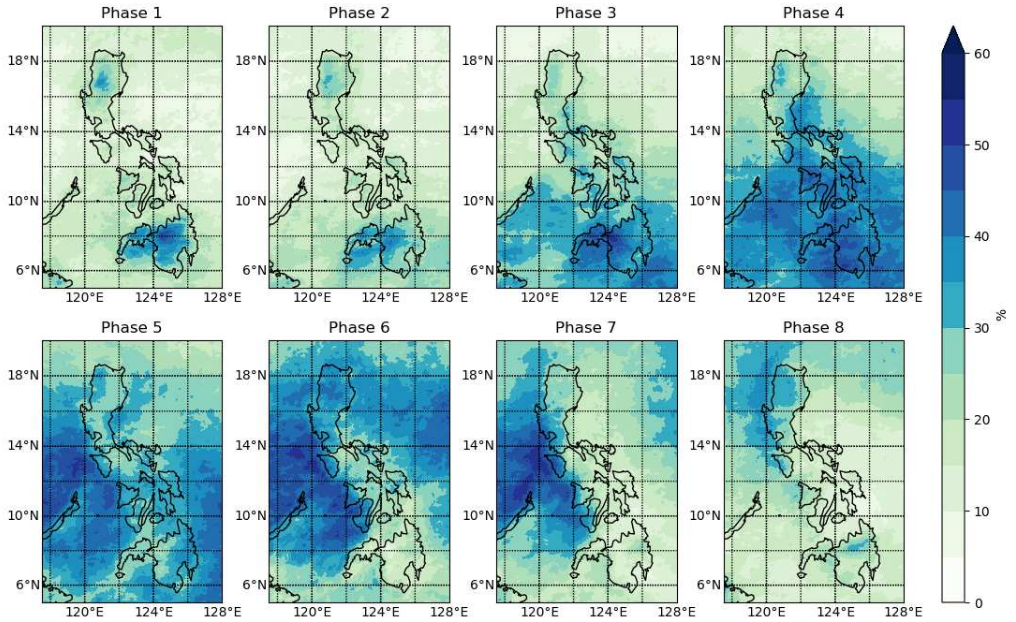

(b) Relative Change in Probability of Above Average Daily Mean

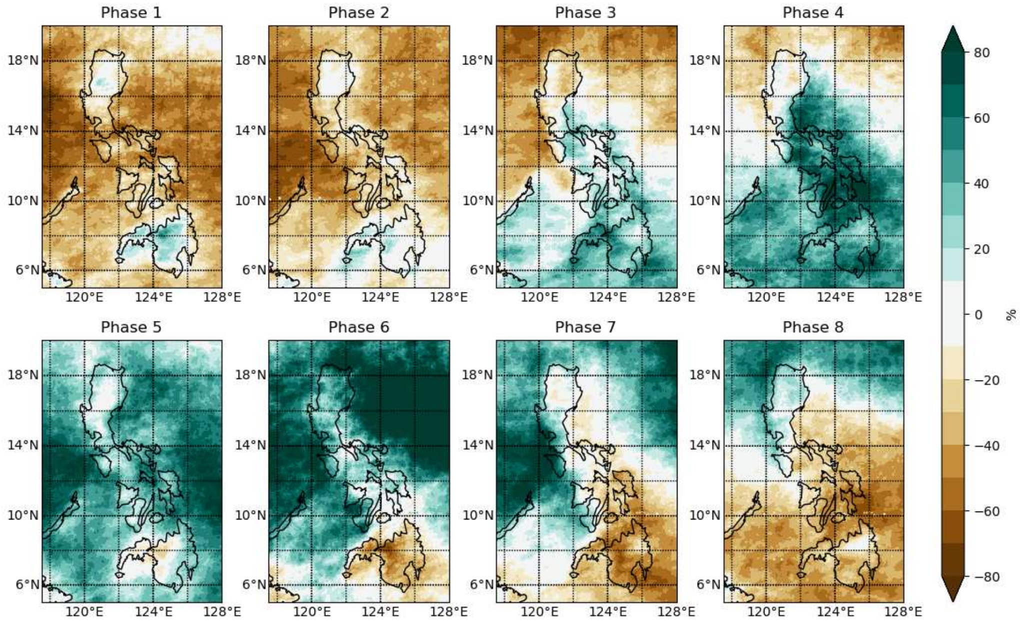

Figure 3.7: Given that the BSISO is active and within phase noted, the probability that the CMORPH daily mean precipitation rate is greater than or equal to the full boreal summer average precipitation rate in (a), and relative change in this probability compared to the probability of any day in boreal summer being above this average in (b).

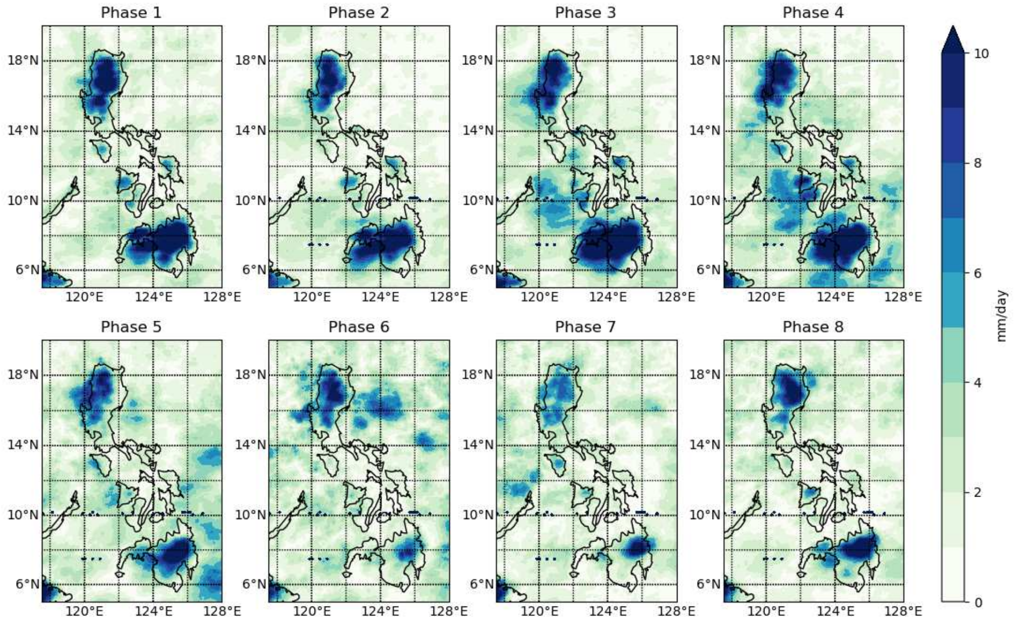
(a) Composite Diurnal Cycle Amplitude

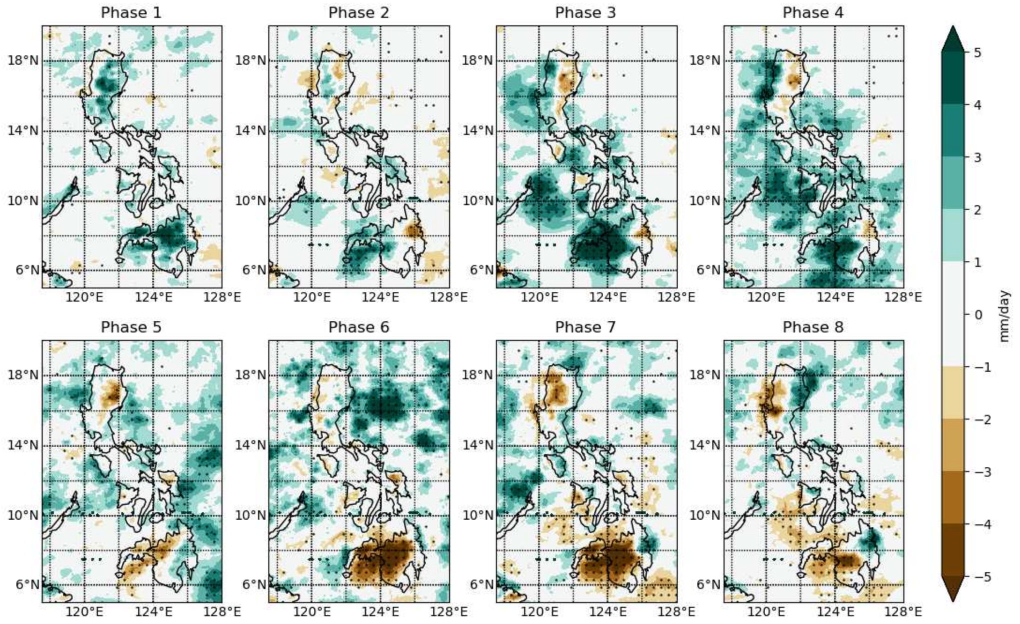
(b) Amplitude Anomaly

Figure 3.8: The amplitude of the first diurnal harmonic of the composite diurnal cycle in each Lee et al. 2013 BSISO phase (a) and its anomaly from the amplitude of the full boreal summer composite diurnal cycle (b) in mm day^{-1}, with statistical significance at the 95% level shown in (b) as black dots.

(a) Daily Mean Anomaly

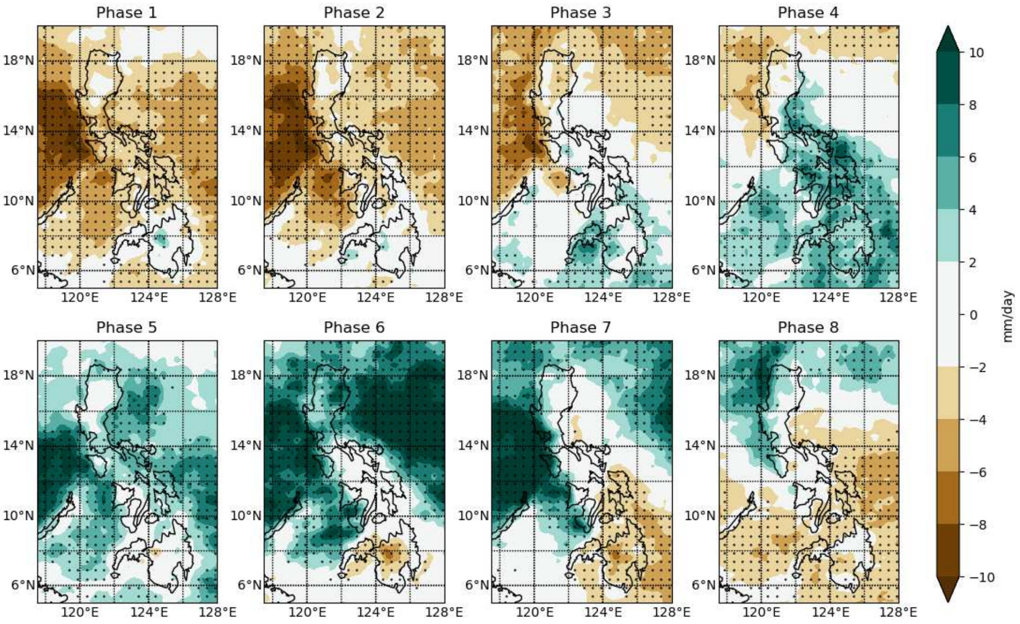

(b) Amplitude Anomaly

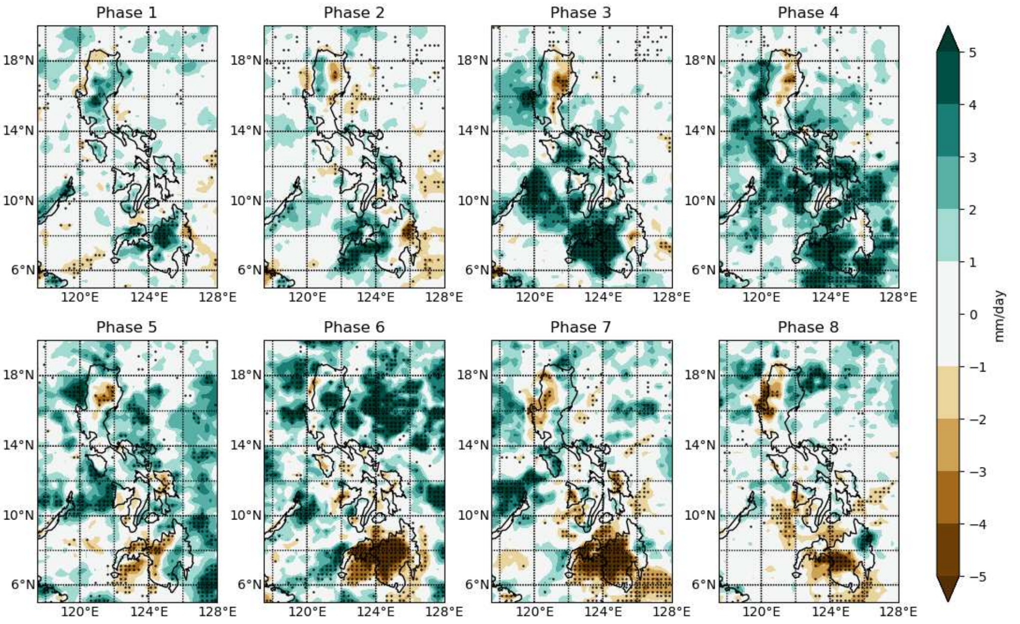

Figure 3.9: TRMM 3B42HQ anomalies in daily mean precipitation (a) and amplitude of the composite diurnal cycle (b), in mm day^{-1}, from May-October by Lee et al. 2013 BSISO phase. Same as Figure 3.3 and Figure 3.8b respectively, but from TRMM.

(a) Daily Mean Anomaly

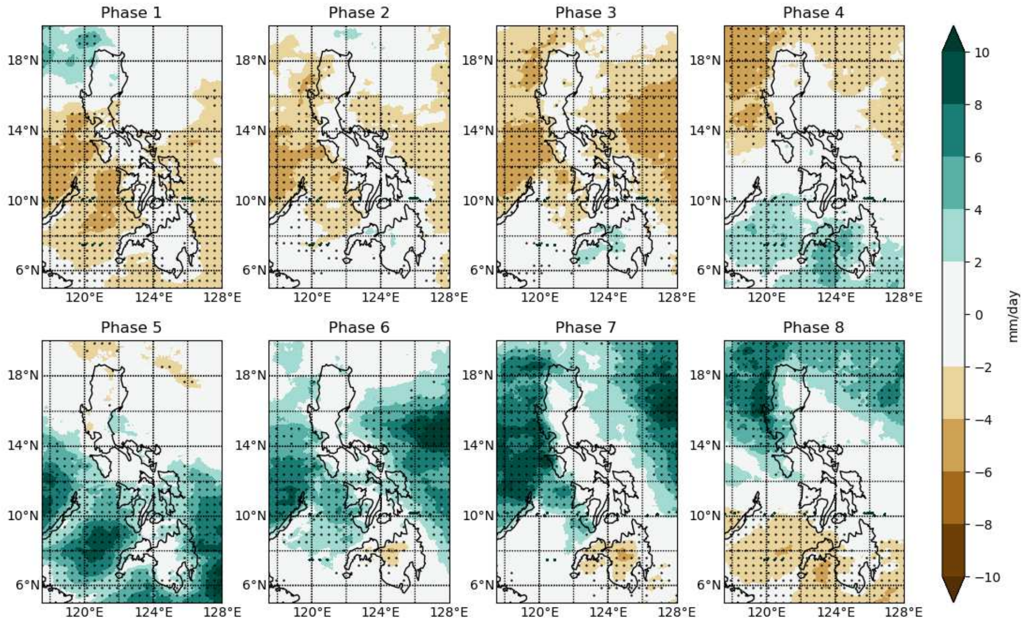

(b) Amplitude Anomaly

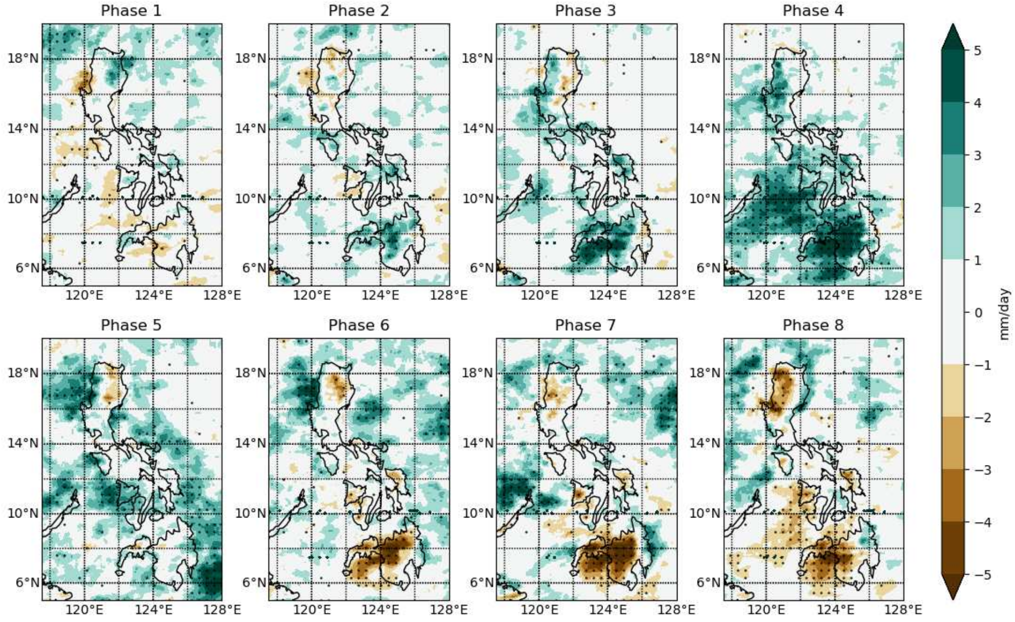

Figure 3.10: CMORPH anomalies in daily mean precipitation (a) and amplitude of the composite diurnal cycle (b), in mm day^{-1}, from May-October by Kikuchi et al. 2012 BSISO phase. Same as Figure 3.3 and Figure 3.8b respectively, but a different index.

(a) Daily Mean Anomaly

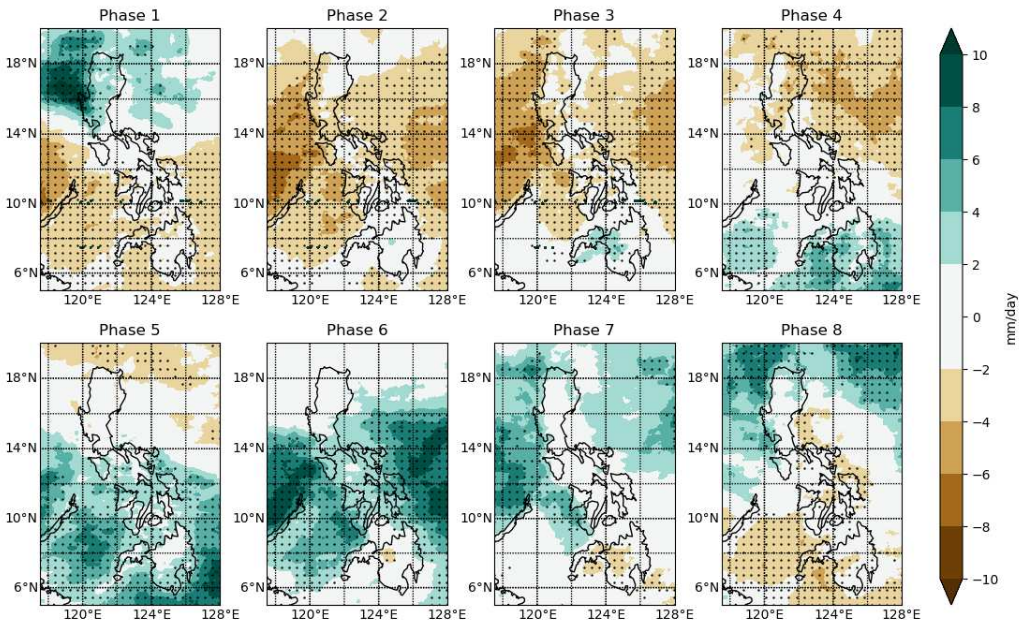

(b) Amplitude Anomaly

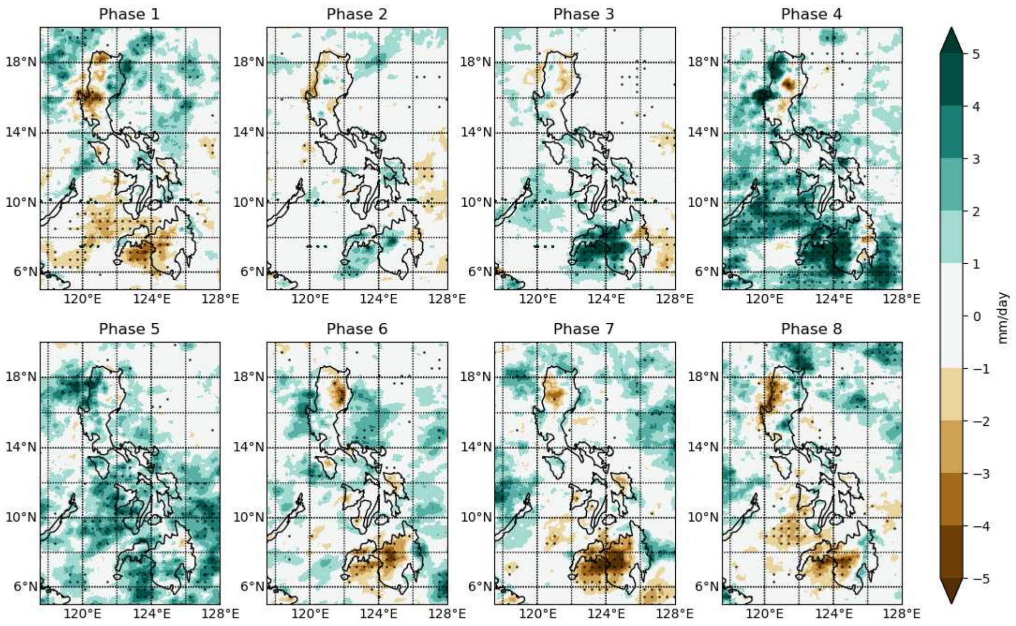

Figure 3.11: CMORPH anomalies in daily mean precipitation (a) and amplitude of the composite diurnal cycle (b), in mm day^{-1}, from May-October by Kiladis et al. 2014 OMI phase. Same as Figure 3.3 and Figure 3.8b respectively, but a different index.

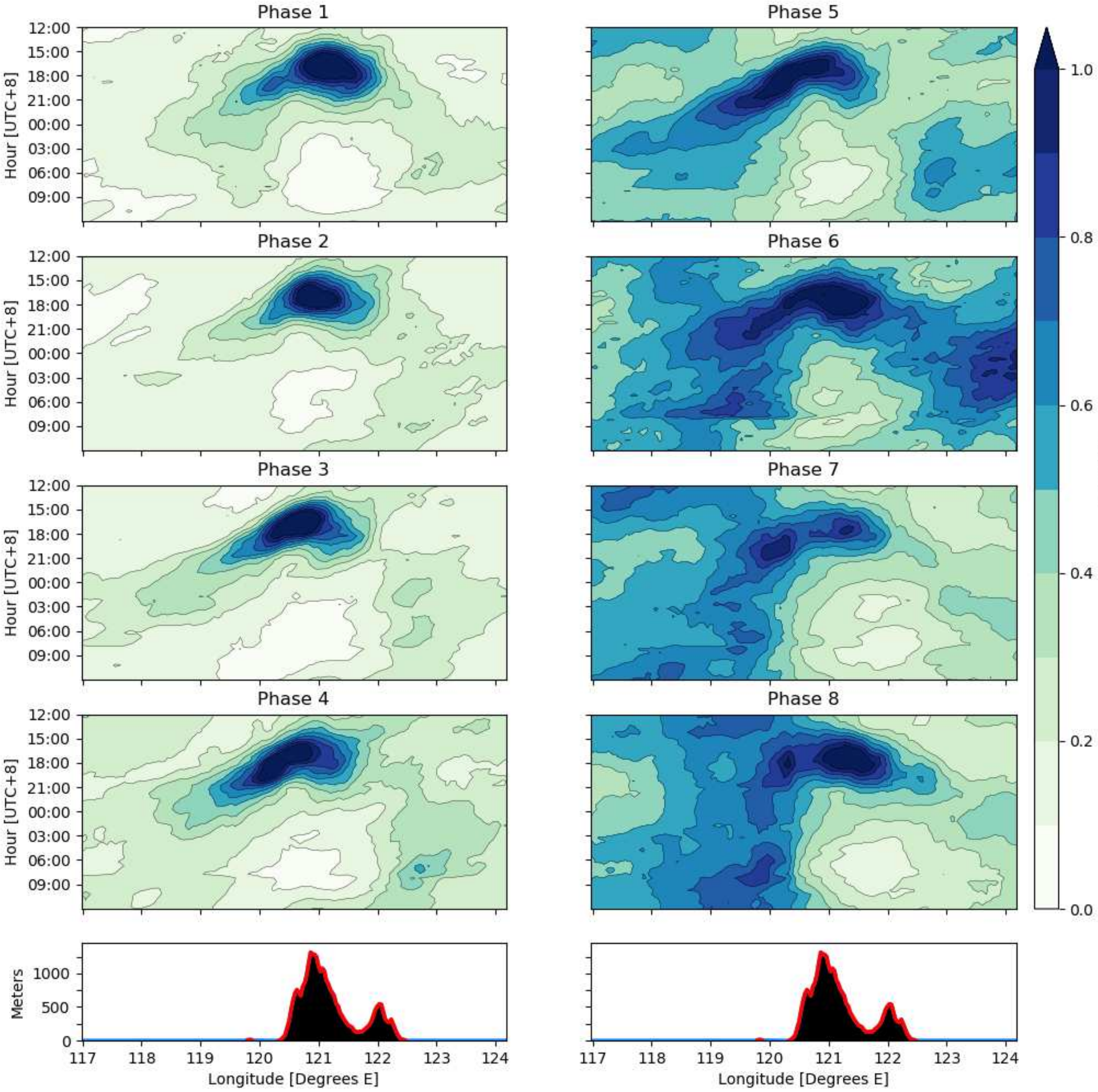

Figure 3.12: CMORPH May-October BSISO composite diurnal cycles, latitudinally averaged precipitation over northern Luzon (16°-18°N; box "A" shown in Figure 2.16) in mm hr^{-1} as a function of longitude (x-axis) and time of day in Manila, Philippines (y-axis, increasing downward), with average topography plotted below, and statistical significance at the 95% level shown in black dots.

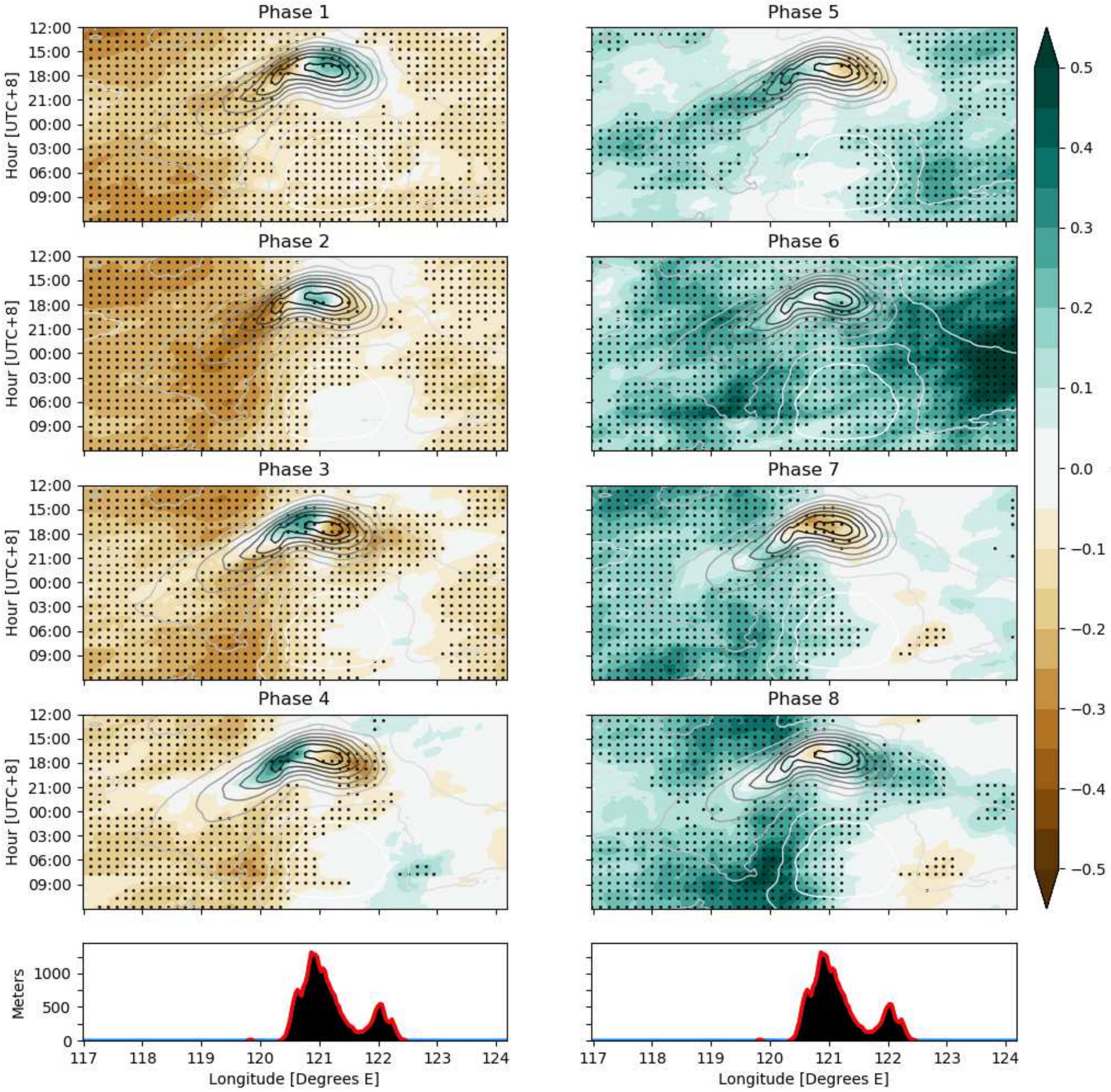

Figure 3.13: CMORPH May-October composite diurnal cycle, latitudinally averaged precipitation over northern Luzon (16°-18°N; box "A" shown in Figure 2.16) in mm hr^{-1}as a function of longitude (x-axis) and time of day in Manila, Philippines (y-axis, increasing downward) shown in contours, every 0.1 mm hr^{-1}, with white indicating lower precipitation rates, and black indicating higher precipitation rates. Then, BSISO composite diurnal cycle anomalies from the black and white contours shown in colors, with average topography plotted below, and statistical significance at the 95% level shown in black dots.

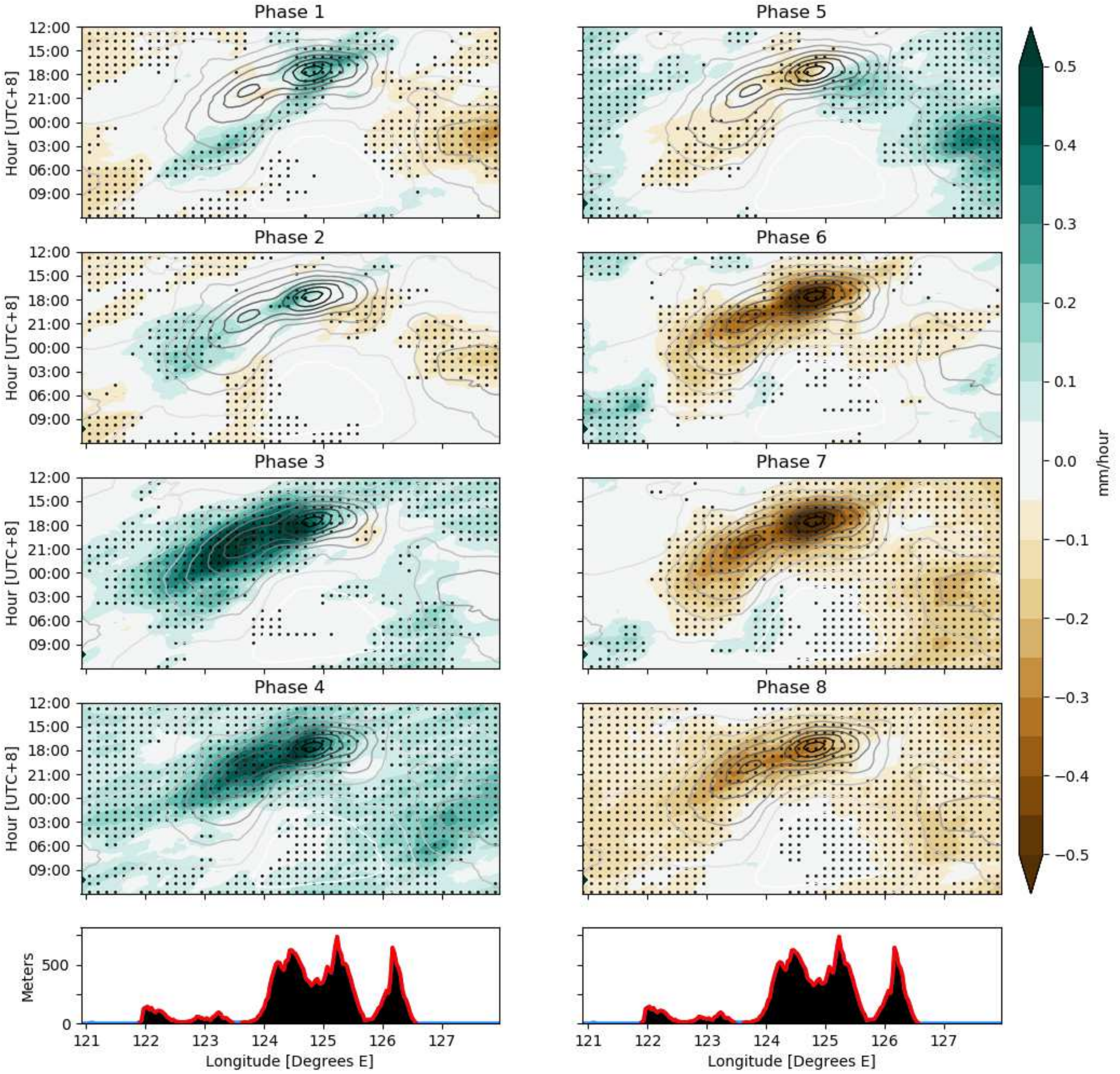

Figure 3.14: CMORPH May-October composite diurnal cycle, latitudinally averaged precipitation over Mindanao (6°-8°N; box "B" shown in Figure 2.16) in mm hr^{-1} as a function of longitude (x-axis) and time of day in Manila, Philippines (y-axis, increasing downward) shown in contours, every 0.1 mm hr^{-1} with white indicating lower precipitation rates, and black indicating higher precipitation rates. Then, BSISO composite diurnal cycle anomalies from the black and white contours shown in colors, with average topography plotted below, and statistical significance at the 95% level shown in black dots.

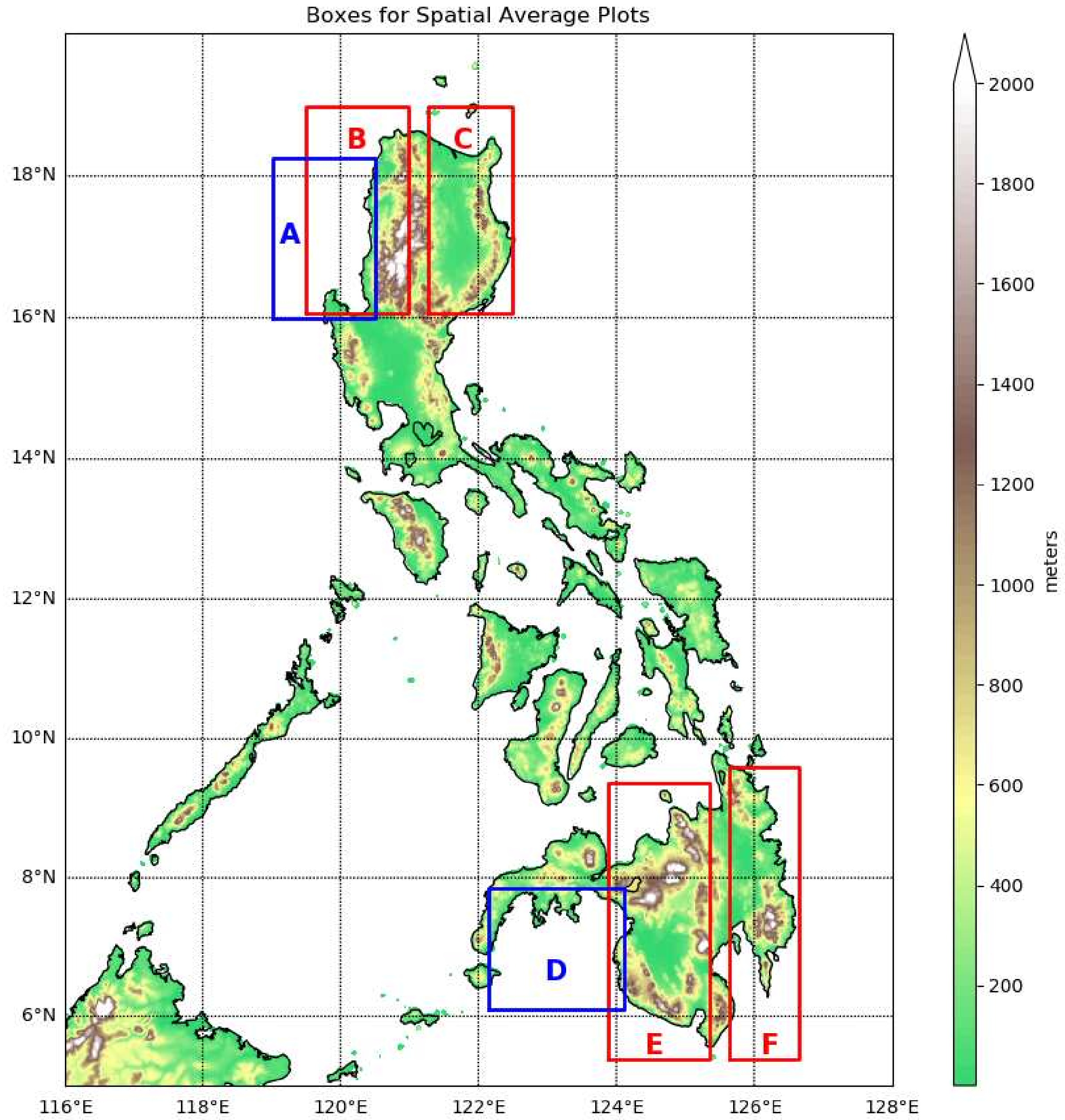

Figure 3.15: ETOPO2 topography and bathymetry (in meters) with boxes indicating the domain for spatial averaging the composite diurnal cycle. Blue boxes indicate regions in which only oceanic points were considered, and red boxes indicate where only land points were considered.

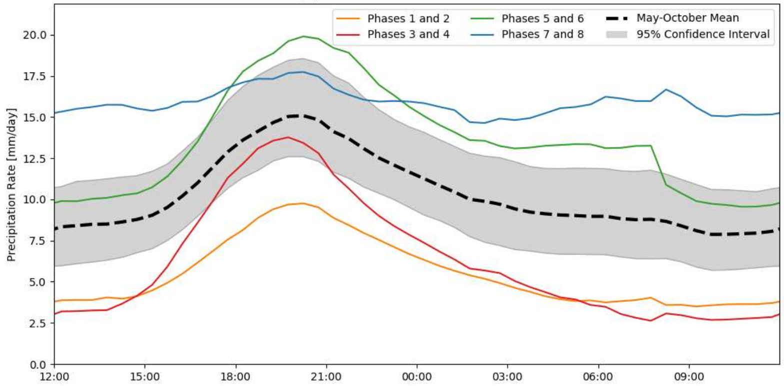
(a) Coastal Waters Northwest Luzon

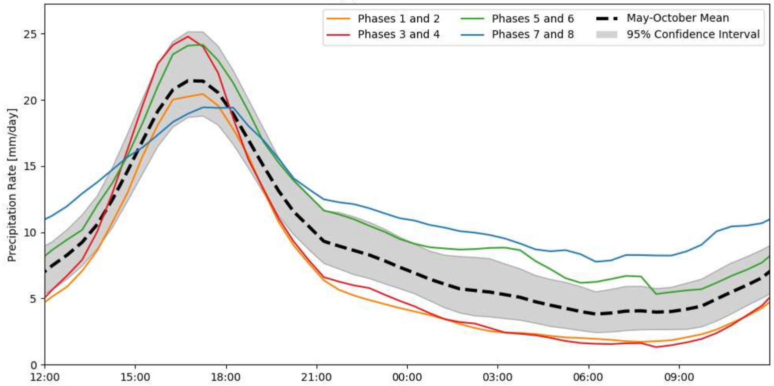
(b) Northwest Luzon

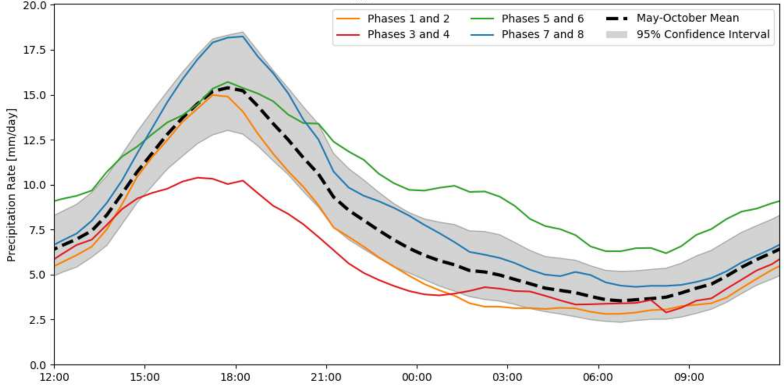
(c) Northeast Luzon

Figure 3.16: BSISO composite diurnal cycles of CMORPH precipitation spatially averaged over (a) Ocean points only west of Luzon (Box "A" in Figure 3.15), (b) Land points only over northwest Luzon (Box "B" in Figure 3.15), and (c) Land points only over northeast Luzon (Box "C" in Figure 3.15). The May-October composite diurnal cycle in these boxes are showed in the dotted black line. 95% of all random composite diurnal cycles fall inside the gray bounds when averaged over this box.

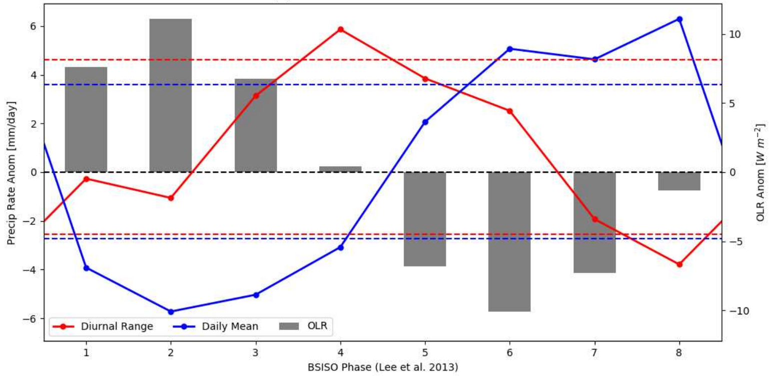
(a) Coastal Waters Northwest Luzon

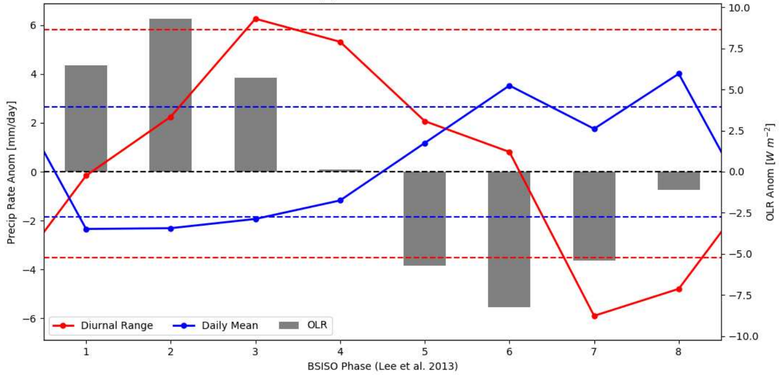
(b) Northwest Luzon

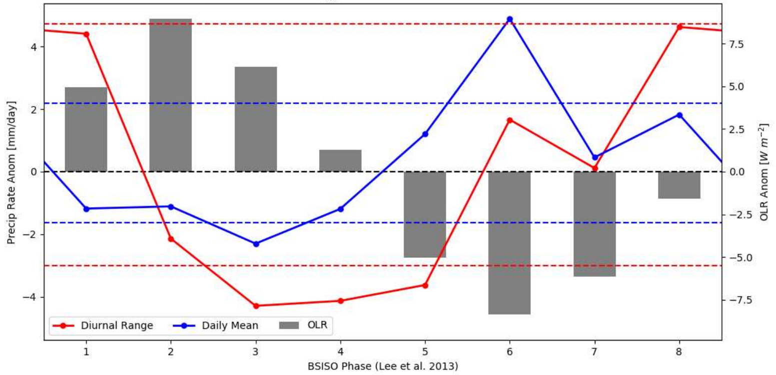
(c) Northeast Luzon

Figure 3.17: Anomalies in CMORPH daily mean precipitation rate, and diurnal amplitude of precipitation rate of BSISO composite diurnal cycles plotted in Figure 3.16, spatially averaged over (a) Ocean points only west of Luzon (Box "A" in Figure 3.15), (b) Land points only over northwest Luzon (Box "B" in Figure 3.15), and (c) Land points only over northeast Luzon (Box "C" in Figure 3.15). The 95% confidence bounds for the daily mean and diurnal amplitude are plotted in dotted blue and red lines respectively. Composite OLR anomalies over the entire island are shown in gray boxes, by Lee et al. 2013 BSISO phase on the x-axis.

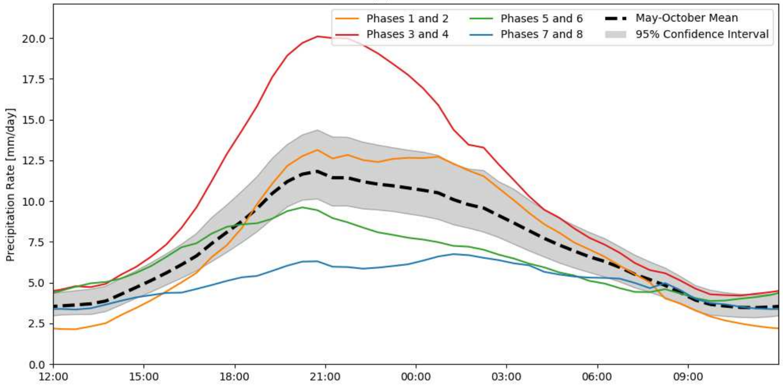
(a) Moro Gulf

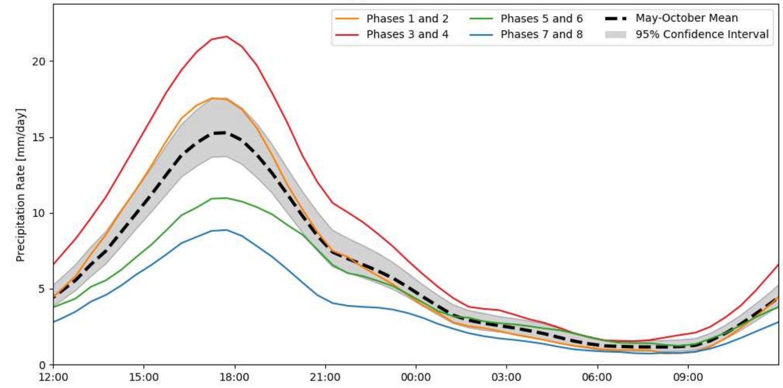
(b) Central Mindinao

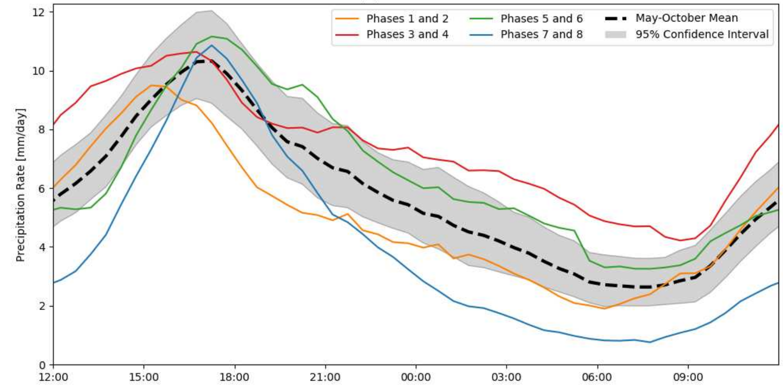
(c) East Mindinao

Figure 3.18: BSISO composite diurnal cycles of CMORPH precipitation spatially averaged over (a) Ocean points only in the Moro Gulf (Box "D" in Figure 3.15), (b) Land points only over central Mindanao (Box "E" in Figure 3.15), and (c) Land points only over eastern Mindanao (Box "F" in Figure 3.15). The May-October composite diurnal cycle in these boxes are showed in the dotted black line. 95% of all random composite diurnal cycles fall inside the gray bounds when averaged over this box.

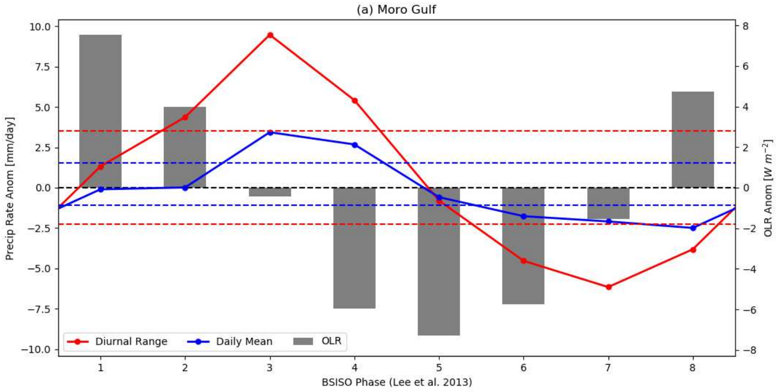

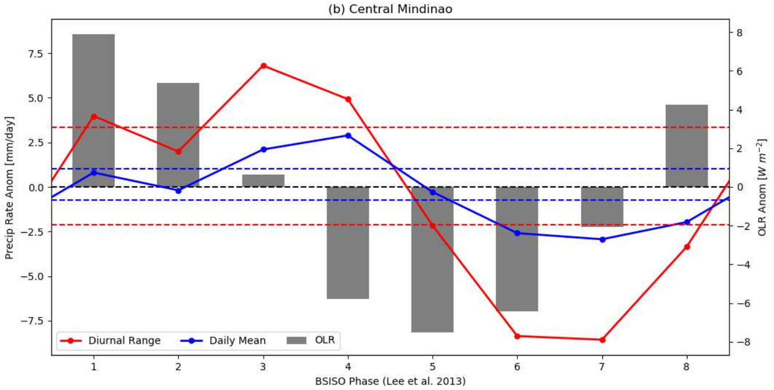

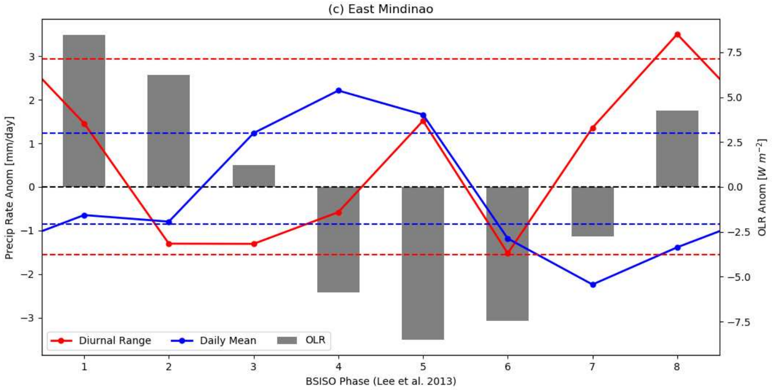

Figure 3.19: Anomalies in CMORPH daily mean precipitation rate, and diurnal amplitude of precipitation rate of BSISO composite diurnal cycles plotted in Figure 3.16, spatially averaged over (a) Ocean points only in the Moro Gulf (Box "D" in Figure 3.15), (b) Land points only over central Mindanao (Box "E" in Figure 3.15), and (c) Land points only over eastern Mindanao (Box "F" in Figure 3.15). The 95% confidence bounds for the daily mean and diurnal amplitude are plotted in dotted blue and red lines respectively. Composite OLR anomalies over the entire island are shown in gray boxes, by Lee et al. 2013 BSISO phase on the x-axis.

Chapter 4

Mechanisms

The last chapter focused on the impact of the BSISO on the diurnal cycle of precipitation over the Philippines and SCS. An elevated diurnal cycle over high topography was observed during the inactive period of the BSISO, with enhanced precipitation in the afternoon peak, and suppressed precipitation at all other times of day. In addition, there was an increased preference for westward offshore propagation during BSISO onset. In this chapter, some mechanisms to help explain this behavior will be presented.

It will be shown that the observed enhancement of the diurnal cycle is collocated with decreased prevailing winds in the lower-troposphere, leading to a strong sea-breeze circulation in the suppressed phases when combined with the increased insolation present. Furthermore, as the transition into the active phase begins, mid-level moisture begins to increase, which then allows the convection that developed over land to propagate further offshore. Evidence will be presented in this chapter that shows a collocation between wind, moisture, insolation, and precipitation anomalies, but this will not address which pattern leads and which follows. In this thesis, these mechanisms are hypothesized as a possible explanation derived from observations, but future modeling studies are needed to establish cause and effect.

4.1 Prevailing Winds

In addition to its modulation of convection, the BSISO also impacts wind patterns over the MC. The change in wind patterns is one potential factor that could promote the enhancement of the diurnal cycle in the BSISO inactive period. The mean state boreal summer winds in the SCS are characterized by broad southwesterly flow at low levels associated with the monsoonal trough (recall Figure 2.3). The BSISO is superimposed on this background state, altering the background monsoon pattern on intraseasonal timescales.

Surface wind anomalies from ASCAT and ERA-Interim are shown in Figures 4.1 and 4.2 respectively. In addition, bandpassed anomalies of ERA-Interim daily mean sea level pressure are shown in Figure 4.3, which indicate the anomalous positioning of the monsoon trough. In the beginning of the suppressed BSISO phases (1-2) winds are generally quite weak near the Philippines, indicative of a "break" period in the climatological monsoon flow (Maloney and Hartmann 1998, Sengupta et al. 2001). As the anomalous pressure trough nears in phases 3-4, easterlies in the Philippine Sea strengthen, while weak southerlies emerge in the SCS. When the pressure trough passes through the region of interest in phases 5-6, the strong southwesterly monsoon flow returns to the South China sea, converging with the trade winds just east of the Philippines. Wind speeds of 6-8 m s^{-1} are common during the active BSISO period, compared to 2-5 m s^{-1} in phases 1-4. Towards the end of the active BSISO period (phases 7-8), strong southwesterly winds are present across the entire domain, including the Philippine Sea. This is analogous to the westerly wind bursts seen in the active wintertime MJO.

On land, the active BSISO brings strong onshore flow to the western side of every major Philippine island. For Luzon, this is particularly true in phases 7-8, since the monsoon trough is still located over the northern part of the island in phases 5-6. It is proposed that this burst of southwesterly wind in the active phase overwhelms the sea-breeze circulation, and thus limits the diurnal cycle, consistent with a mechanism discussed in prior studies (Houze et al. 1981, Saito et al. 2001, Fujita et al. 2011, Oh et al. 2012). When strong onshore flow is present in the lower-troposphere due to large-scale features such as the monsoon trough, convergence over land is diminished, thus weakening the diurnal cycle. This mechanism also provides a possible explanation for the disparity in diurnal cycle strength on the western and eastern sides of the Philippines. In phases 1-4, the large-scale monsoonal flow promotes strengthening easterlies impinging on the eastern side of the Philippines (onshore), with weak intraseasonal winds in the SCS. On the eastern side, this reduces convergence during the day and increases it at night offshore (due to the land breeze). Thus, the weakest diurnal cycle over the eastern Philippines occurs when the trades are strongest (phases 3-4). Conversely, winds are weakly offshore over the western side of the archipelago during these phases, which increases (decreases) convergence during the day (at night), leading to more (less) precipitation, and thus a higher amplitude diurnal cycle. When strong southwesterly winds flow over the Philippines (phases 5-8), convergence due to the sea-breeze over land is diminished, suppressing the diurnal cycle in the west, but enhancing it in the east. This mechanism does not consider an increase in convergence associated with intraseasonal winds hitting high topography. Understanding the relative contributions of the sea-breeze related convergence and topographic convergence will be important in establishing the applicability of this proposed mechanism. The change in the sea-breeze will be shown in the next section.

Also notable from Figures 4.1 and 4.2 is that this pattern is consistent in both ASCAT and ERA-Interim (as well as QuikSCAT, which is not shown), showing that ERA-Interim winds can be reliable for BSISO studies. ERA-Interim has the advantage of 3-hourly temporal resolution, which allows for a more detailed interpretation of the diurnal cycle, something that ASCAT and QuikSCAT cannot provide. Furthermore, Rapidscat does not have the temporal coverage for adequate BSISO statistics, with less than two full boreal summers in the record. ERA-Interim also captures the diurnal cycle of surface wind quite well when compared to RapidScat, as established in section 2.4. However, it is worth noting that parameterized convection in ERA-Interim could bias precipitation to peak early, thus shutting down the sea-breeze earlier than expected (Birch et al. 2015). Thus, ERA-Interim appears suitable to analyze BSISO modulations of the diurnal cycle of surface wind, which will be the subject of the next section.

4.2 Sea-Breeze Circulation

It has been well established (R. Johnson et al. 1999, Myers and Waliser 2003, Sakaeda et al. 2017) that the active phase of the BSISO is accompanied by increased cloudiness, which results in decreased insolation over land. As a result, a decrease in the strength of the sea-breeze circulation is expected during the active phase. Figure 4.4 shows anomalies in surface downwelling shortwave radiation by BSISO phase, while Figure 4.5 shows the amplitude of the first diurnal harmonic of the composite diurnal cycle in surface zonal wind, a proxy for the strength of the sea-breeze circulation on meridionally oriented coastlines. The discussion will focus on oceanic winds, since surface winds over complex topography may be untrustworthy and not indicative of the sea-breeze circulation. In phases 1-2, a moderately enhanced diurnal cycle in surface zonal wind is observed concurrent with strongly positive insolation anomalies. In phases 3-4, this pattern weakens over the southern Philippines, but remains present near Luzon. After the onset of the active phase (5-6), the diurnal cycle amplitude of zonal wind weakens over coastal waters west of all of the major Philippine islands. This continues to the end of the active period, in phases 7-8, with suppressed diurnal amplitudes. Negative insolation anomalies are present throughout this period, although positive anomalies emerge over Mindanao by phase 8. This mechanism has been hypothesized in many prior studies (Peatman et al. 2014, Birch et al. 2016).

On the east side of the archipelago, there is not a strong signal in the modulation of the sea-breeze circulation by BSISO phase, with the exception of a weak suppression (enhancement) east of Mindanao in phases 3-4 (7-8), concurrent with the weakest (strongest) diurnal cycles in precipitation over eastern Luzon and Mindanao. While consistent with expectations, the pattern is modest, suggesting insolation driven changes in the sea-breeze circulation are not the only important feature. Another possibility, discussed in the prior section, is that the lack of strong onshore flow in the enhanced phases (on the eastern side) allows a strong diurnal cycle in precipitation to continue, even when insolation is diminished (Fujita et al. 2011, Oh et al. 2012). Insolation changes alone appear insufficient to explain the observed changes in the diurnal cycle of precipitation, consistent with prior work (Peatman et al. 2014).

The sea-breeze circulation is indeed strongest in the suppressed periods, corresponding to a strong diurnal cycle exclusively over land on the western side of the islands. However this does not explain why the transition period from inactive to active shows a strong diurnal cycle that then is able to propagate well offshore. This does not occur during the beginning of the suppressed BSISO period, only towards the end. The established BSISO modulation of surface wind and insolation do not distinguish strongly between the early suppressed phases, and the later phases (L13 3-4 for Luzon). For Mindanao, insolation appears to in fact favor phases 1-2, while the strongest propagating diurnal cycle occurs in phases 3-4. For Luzon, the highest insolation is found in phases 2-3, while the strongest propagating diurnal cycle appears in phases 4-5.

4.3 Mid-Level Moisture

In this section, evidence will be presented suggesting that mid-level moisture is an important factor that drives cell longevity as the diurnal storms propagate offshore. Convection has been closely tied to column water vapor in prior studies (Raymond et al. 2000, Bretherton et al. 2004). Others have suggested that lower- to mid-tropospheric moisture in particular precedes deep convection (Holloway and Neelin 2009, 2010, Barnes and Houze 2013, Yuan and Houze 2013). This pattern has also been observed prior to large-scale deep convective onset in ISO events (Hsu et al. 2004, Jiang et al. 2004, R. Johnson and Ciesielski 2013, Adames and Wallace 2015, Ruppert and R. Johnson 2015). An increase in moisture in the lower free-troposphere also appears to emerge in the area of interest just before BSISO onset.

Figure 4.6 shows BSISO composites of daily mean wind zonal and vertical wind vectors, with anomalies from the boreal summer mean of specific humidity latitudinally averaged over Luzon. Figure 4.7 shows the same thing for a latitudinal average over Mindanao. At first glance, the same general pattern of dry air at all levels is evident in the suppressed phases, and the reverse in the enhanced. However, closer examination reveals an interesting change in the lower free troposphere, from 700 to 900-hPa, and at 850-hPa in particular. In phases 1-3, a strong diurnal cycle is present over the Luzon and Mindanao, but it does not propagate strongly offshore until phase 2 for Mindanao and phase 3 for Luzon. In Figure 4.7, there is evidence of a positive anomaly in specific humidity centered at 850-hPa over the Moro Gulf. Similarly, on the west side of Luzon, dry anomalies in the free-troposphere weaken in phase 3 before actually becoming weakly positive in phase 4 at 850-hPa. Interestingly, dry anomalies are still present over the eastern side of Luzon, which could be a contributing factor that assists in the propagation of the diurnal cycle to the west, but not to the east. This moister west side is also seen for Mindanao in phases 2-3.

In phase 4 for Mindanao and phase 5 for Luzon, moist anomalies spread through the entire troposphere, corresponding to the onset of widespread deep convection. However, these anomalies are still stronger on the west side of the islands, where continued elevated offshore propagation still occurs. One phase later, moisture anomalies are spread evenly across all longitudes, before concentrating on the east side of the islands in the later active phases. In phase 8, there is some evidence of diurnally generated convection propagating east into the Philippine Sea from Luzon. As expected, a positive moisture anomaly is present in the low- to mid-free troposphere on the east side of the island at this time. The mid levels are less dry on the eastern side of Mindanao compared to the western side during these phase (7-8), but Mindanao did not observe a similar tendency for eastward propagation. In summary, while a diurnal cycle is present over land to some extent in all phases of the BSISO, it appears most likely to propagate offshore during the transition from suppressed to active BSISO conditions when moisture is slightly elevated at 850-hPa on the west side of the Philippines.

However, this does not establish if mid-level moisture allows convection to propagate offshore, or if convection propagating offshore increases mid-level moisture. While this study only presents a collocation between the two, other studies have argued that column water vapor, in particular in the mid-troposphere, increases prior to convection (Holloway and Neelin 2010). Furthermore, Holloway and Neelin (2009) suggested that it is unlikely that the increase in mid-tropospheric water vapor is a result of evaporating precipitation alone. Other studies have shown that mid-tropospheric water vapor increases in the region ahead of ISO-related convection (Hsu et al. 2004, R. Johnson and Ciesielski 2013, Adames and Wallace 2015). Collectively, these works add evidence that perhaps it is a mid-level moisture increase promoting storm propagation offshore, not the other way around. While it is hypothesized that this is the case, it is still possible that another mechanism allows the diurnal cycle to propagate further in the transition from inactive to active BSISO in the Philippines and SCS, and this propagation in turn increases mid-level moisture. In either case, a feedback mechanism similar to the moisture mode feedback is likely, where increased specific humidity permits more active convection, which further increases specific humidity.

Prior studies (Peatman et al. 2014, Birch et al. 2016) have hypothesized the importance of frictional moisture convergence in driving the observed peak in the diurnal cycle prior to the onset of ISO convection. Figure 4.8 suggests that this factor could be of secondary importance to prevailing winds, insolation, and mid-level moisture. This figure shows bandpass filtered moisture convergence anomalies at 1000-hPa from ERA-Interim with OLR superimposed. Even though sea level pressure clearly leads BSISO convection (Figure 4.3), near-surface moisture convergence appears more closely in phase with the OLR anomalies rather than the sea level pressure anomalies, despite a slight lead to the north and east. Due to notable spectral ringing in this field near the islands, the reliability of this product is called into question. Furthermore, a consistent lead to the northeast of BSISO convection is not seen in either surface dewpoint or 1000-hPa specific humidity (not shown). However, with the products available at this time, it appears that frictional moisture convergence is of less importance compared to free-tropospheric moisture (Hsu et al. 2004). Figure 4.9 shows bandpass filtered 850-hPa specific humidity anomalies by L13 BSISO phase. Here, there does appear to be a slightly larger lead in humidity anomalies compared to 1000-hPa. This is also seen in fields of moisture convergence at 850-hPa (not shown), but it is much noisier.

In summary, it is hypothesized that the diurnal cycle over land and coastal waters is modulated by the BSISO through three important mechanisms, prevailing low-level winds, surface insolation, and mid-level moisture. The speed and direction of the BSISO winds appears to be related to the diurnal cycle shifting from east to west across the Philippines. When onshore winds are strong, convergence of the sea-breeze circulation over land is weakened, suppressing the diurnal cycle. Thus, the strongest diurnal cycles are expected in coastal areas when intraseasonal onshore flow is weak, which typically occurs in the late-suppressed period over the Philippines. Furthermore, diminished cloud cover in the suppressed period increases surface insolation, which promotes a strong diurnal cycle over land. However, in the early suppressed period when the mid-levels are very dry, diurnally generated convection deteriorates quickly offshore. As the large-scale BSISO convection nears, mid-level moisture increases and convection propagates further offshore, longer into the night. After BSISO onset, onshore flow is strong and insolation decreases, which weakens the diurnal cycle over land, but what is generated still is able to propagate offshore. Late in the active period, the diurnal cycle over land is minimized as dry anomalies start to emerge again in the mid-levels, and precipitation offshore is nearly constant throughout the day.

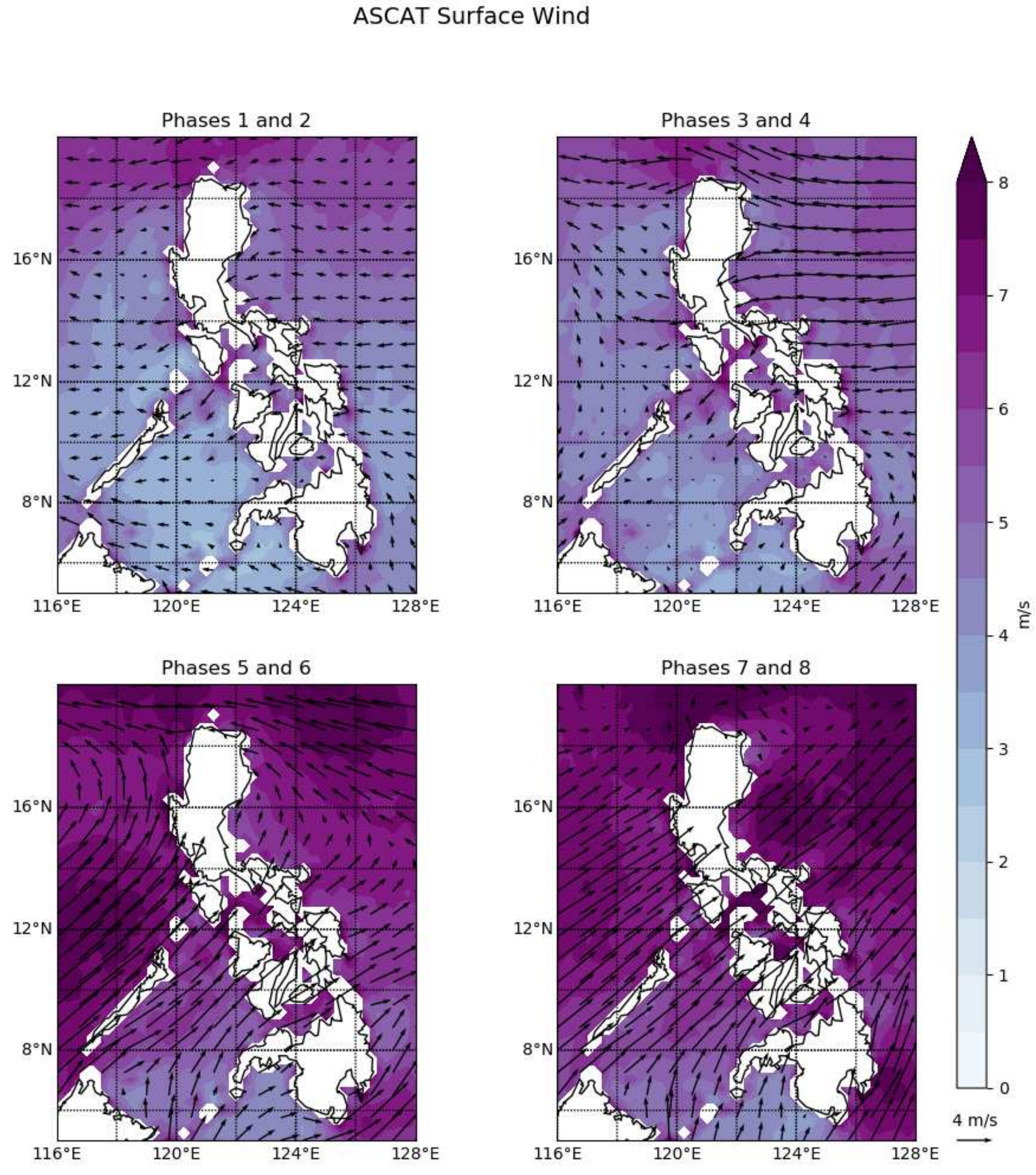

Figure 4.1: ASCAT May-October BSISO composite vector winds, with wind speed shown in contours.

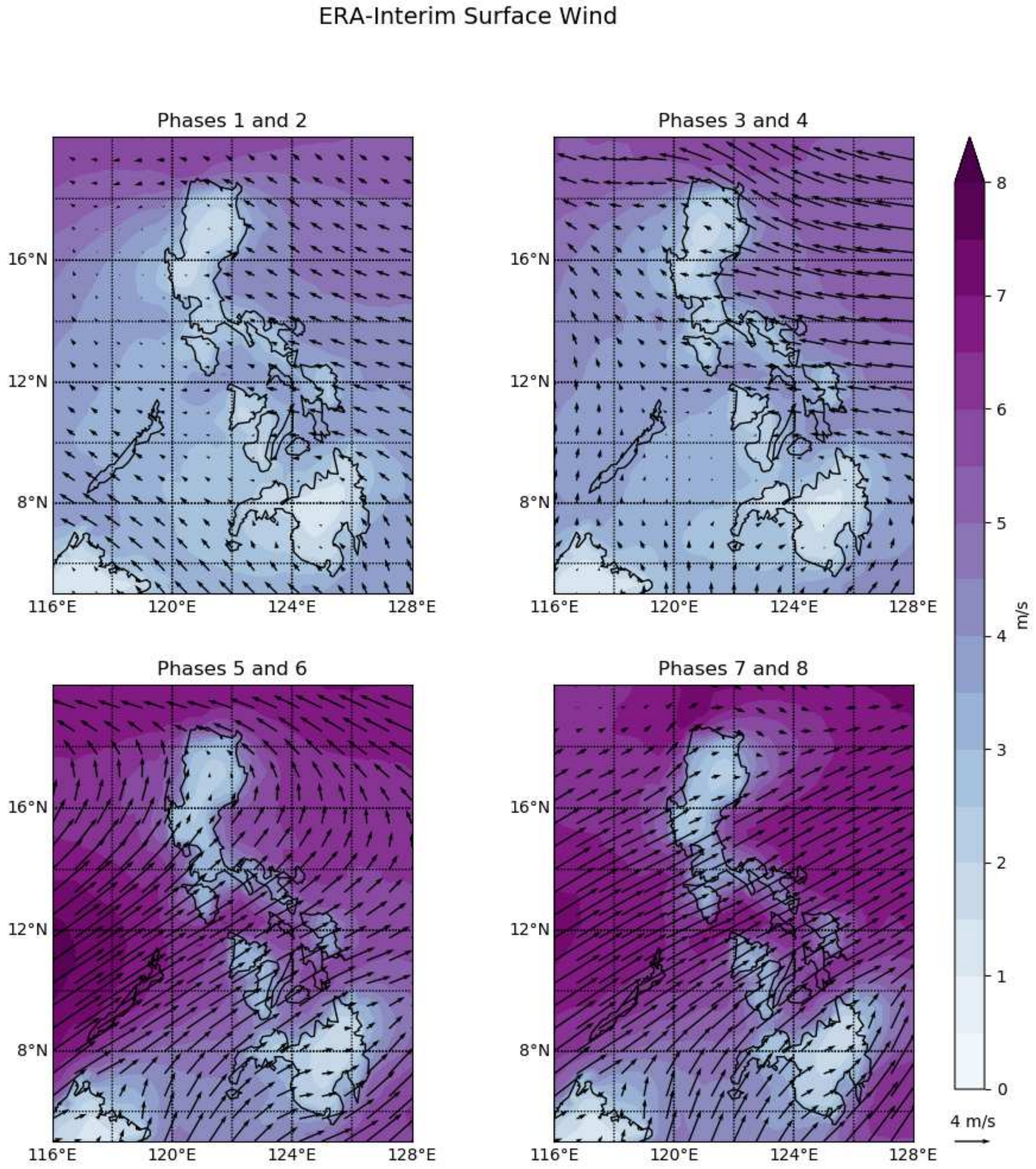

Figure 4.2: ERA-Interim May-October BSISO composite vector winds, with wind speed shown in contours.

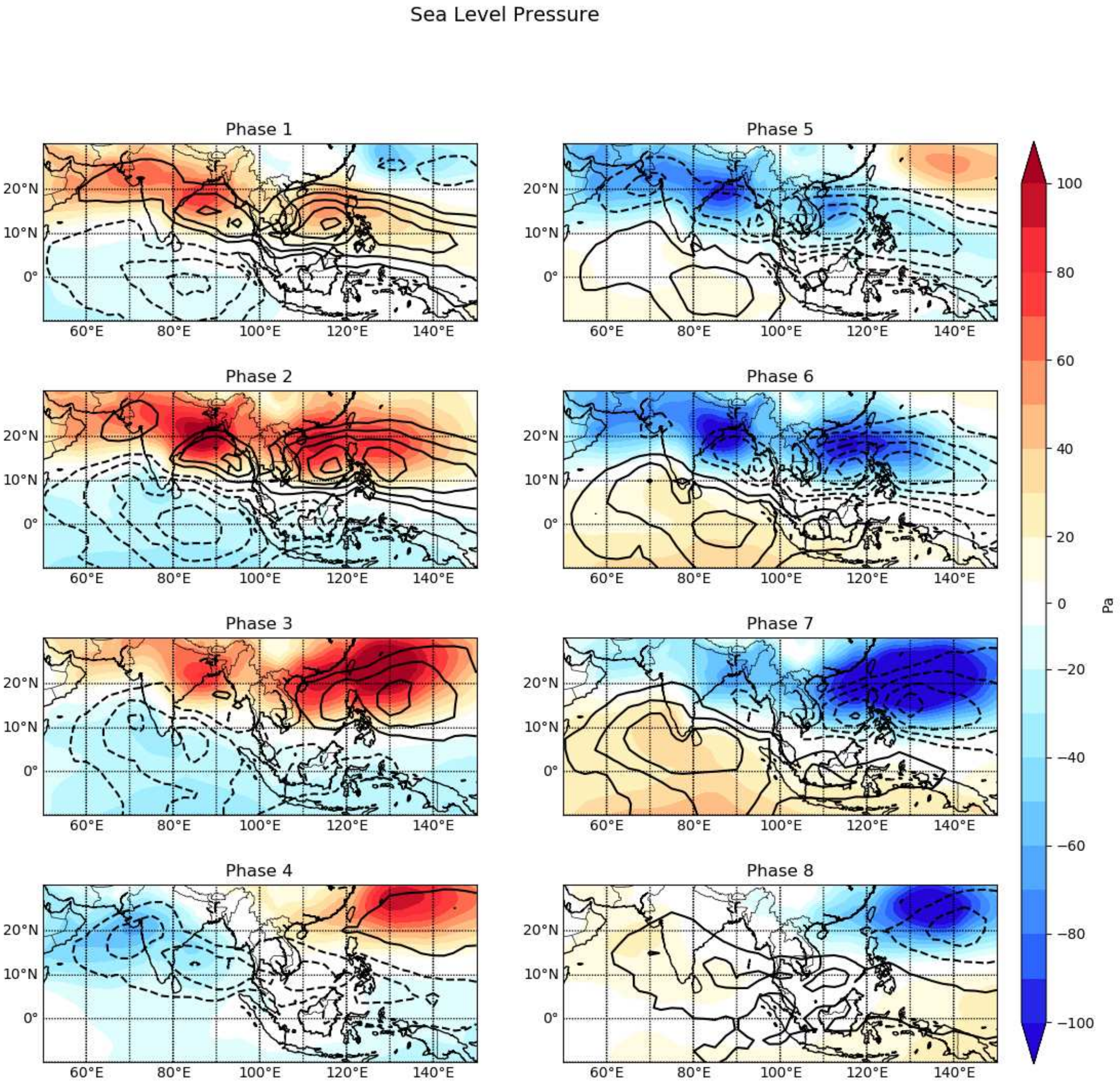

Figure 4.3: Bandpass filtered (30-90 Day) anomalies of daily mean sea level pressure (in colors, Pa) and OLR (in contours; every 3 W m^{-2}) by L13 BSISO phase.

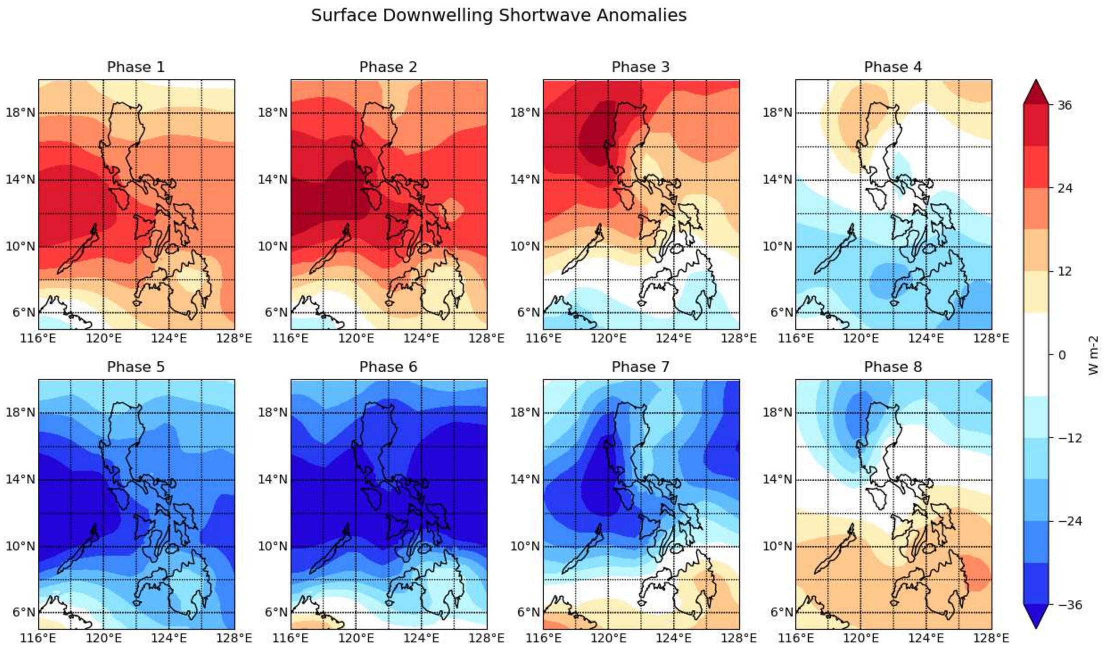

Figure 4.4: Anomaly from May-October full composite of daily mean surface downwelling shortwave radiation (in W m^{-2}) by L13 BSISO phase.

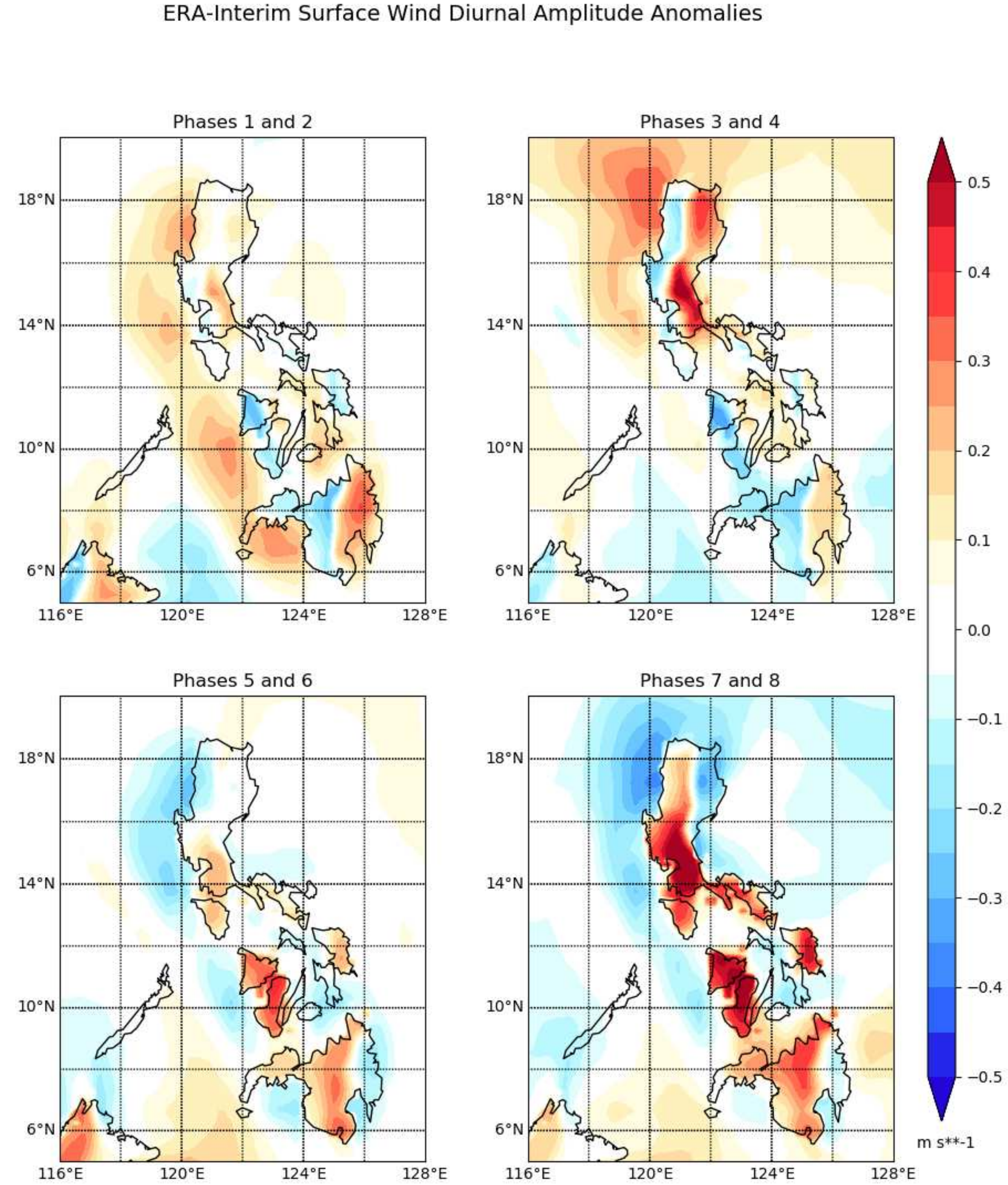

Figure 4.5: Anomaly from May-October full composite of the first diurnal harmonic amplitude of ERA-Interim May-October BSISO composite zonal winds.

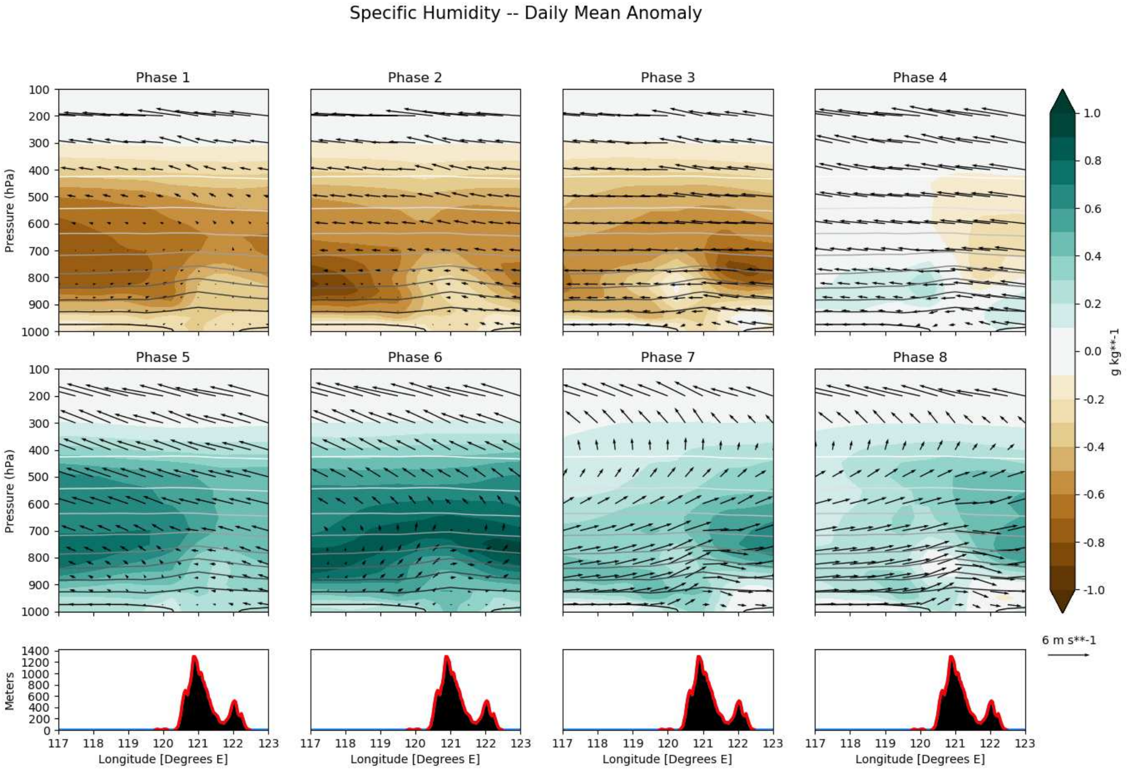

Figure 4.6: Anomalies in daily mean ERA-Interim Specific Humidity (in colors; g kg^{-1}) from May-October Mean (in contours, every 2 g kg^{-1}), and composite daily mean wind vectors (zonal and vertical only, not anomalies), averaged over Luzon from 16°-18°N (box "A" shown in Figure 2.16), by L13 BSISO phase.

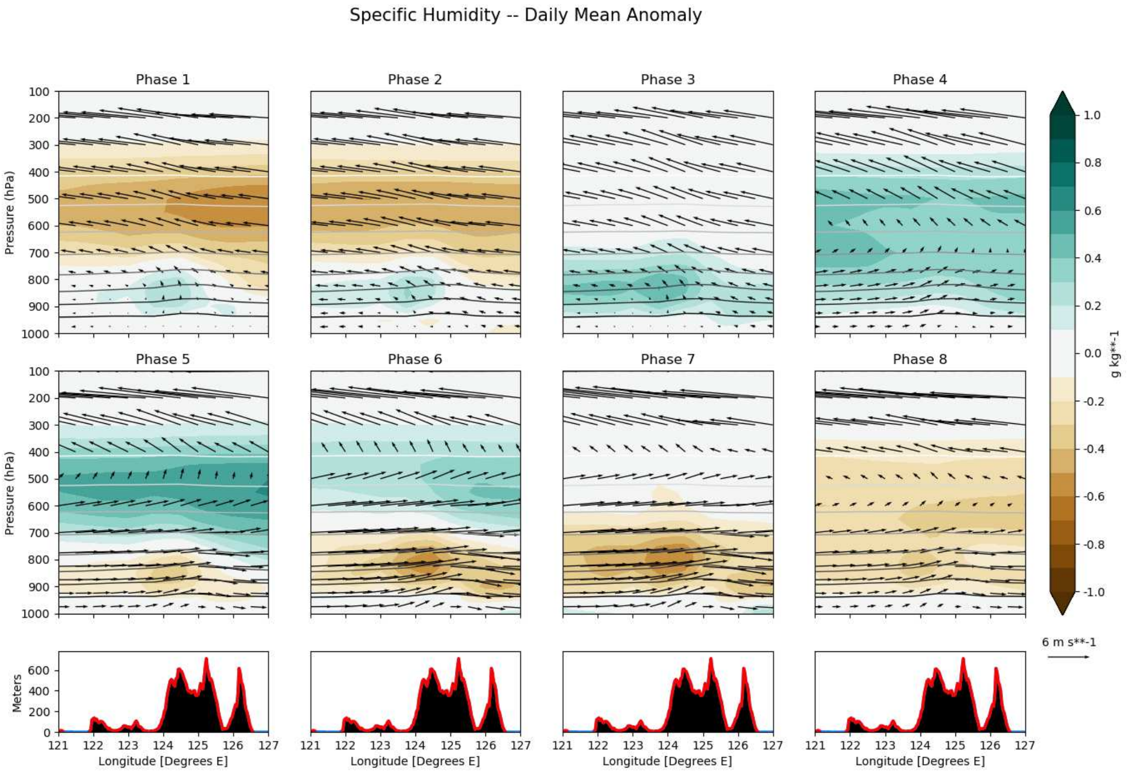

Figure 4.7: Anomalies in daily mean ERA-Interim Specific Humidity (in colors; g kg^{-1}) from May-October Mean (in contours, every 2 g kg^{-1}), and composite daily mean wind vectors (zonal and vertical only, not anomalies), averaged over Mindanao from 6°-8°N (box "B" shown in Figure 2.16), by L13 BSISO phase.

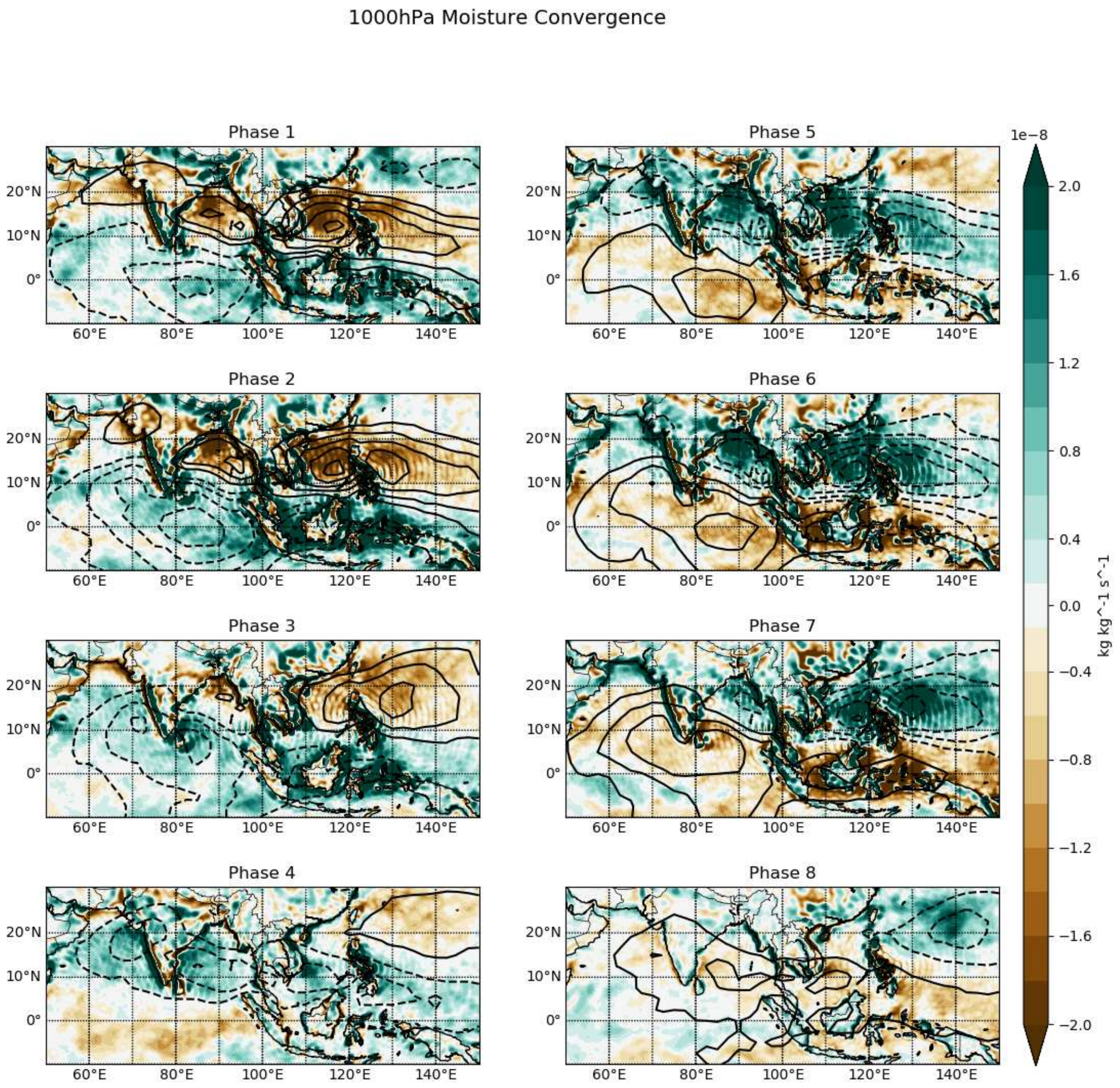

Figure 4.8: Bandpass filtered (30-90 Day) anomalies of daily mean 1000-hPa moisture convergence ($-\nabla \cdot (qv)$; in colors, kg (kg s)$^{-1}$) and OLR (in contours; every 3 W m^{-2}) by L13 BSISO phase.

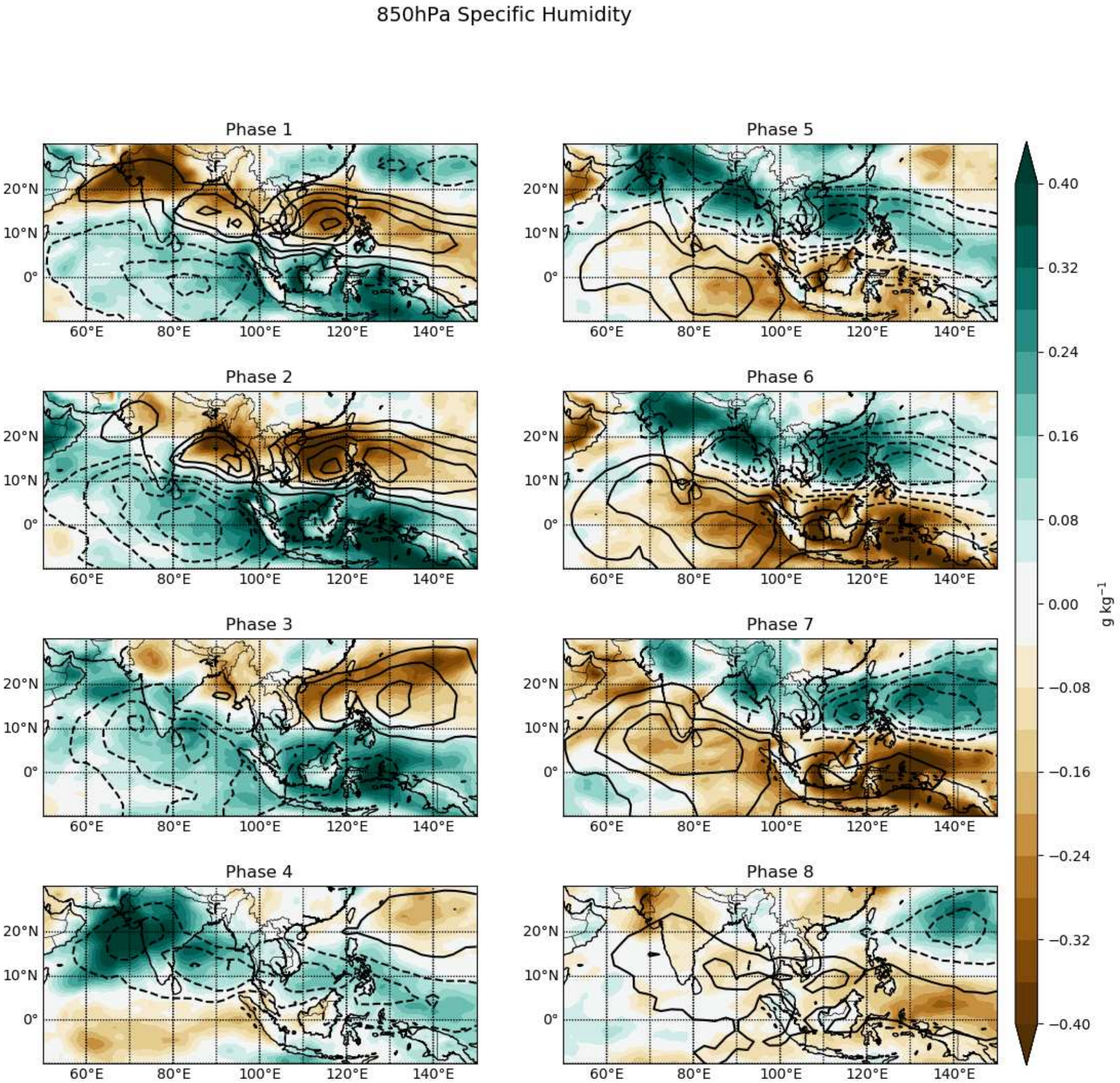

Figure 4.9: Bandpass filtered (30-90 Day) anomalies of 850-hPa specific humidity (colors; g kg^{-1}) and OLR (contours, every 3 W m^2) by L13 BSISO phase.

Chapter 5

Conclusions

5.1 Summary

In this thesis, a thorough analysis of the diurnal cycle over the Philippines and South China Sea (SCS) and its interaction with the Boreal Summer Intraseasonal Oscillation (BSISO) has been presented. The body of literature related to the diurnal cycle, intraseasonal variability, and interactions between the two was extensively reviewed in Chapter 1. In Chapter 2, it was shown that a strong diurnal cycle is present over the large islands of the Philippines that propagates westward in the mean state with a focus on the islands of Luzon and Mindanao. The average diurnal cycle of precipitation in this region looks similar to a sine wave, and peaks in the mid afternoon over small islands, and the late afternoon and evening for the large islands driven by the sea-breeze circulation. Convective precipitation propagates several hundred kilometers offshore, mostly to the west, during the overnight hours and on occasion into the next morning, likely related to advection by the mean flow as well as diurnally generated gravity waves (Love et al. 2011). The amplitude of the diurnal cycle decreases further from shore. While its representation is flawed in reanalysis (Birch et al. 2015), this pattern is well represented across a variety of satellite based retrievals, even those that rely on infrared retrievals. However, a consistent bias towards a later peak in the diurnal cycle is found in all precipitation products based on passive microwave or infrared retrievals when compared to the TRMM Precipitation Radar, which is based on active microwave retrievals (Yanase et al. 2017).

Next, in Chapter 3, the applicability of the Peatman et al. (2014) hypothesis to a general theory ubiquitous to all seasons and all large islands over which the ISO is active was tested. Peatman et al. (2014) proposed that the diurnal cycle and the daily mean precipitation rate are maximized over large MC islands several days before the onset of large-scale ISO convection. They hypothesized that this was due to high insolation present throughout the suppressed phase, combined with frictional moisture convergence associated with the forced Kelvin wave response to tropical heating. This thesis extends these results to the boreal summer season and explores a new region. Results suggest that while some patterns behave similarly in the boreal summer season in the Philippines, there are several important additions and revisions to the Peatman hypothesis proposed here that may improve its generalization to all seasons and all MC islands.

The diurnal cycle of precipitation over the high topography of Luzon and Mindanao reaches its largest amplitude about 1/8 to 1/4 cycle before BSISO onset. However, for Luzon, the diurnal amplitude does not determine the daily mean precipitation rate. During the suppressed BSISO period, precipitation rates are elevated during the afternoon peak, and reduced at all other times of the day, resulting in lower daily mean precipitation rates despite the strong diurnal cycle. The opposite occurs in the BSISO active period, when increased precipitation is found at all times of the day, except the afternoon peak. Thus, the diurnal amplitude still peaks before BSISO onset, similar to studies of the boreal winter season (Peatman et al. 2014, Sakaeda et al. 2017). Mindanao on the other hand, sees much stronger dominance of the diurnal cycle, and the amplitude and daily mean are roughly in phase. Many prior studies did not consider statistical significance, or found that this pattern over land was statistically insignificant (Sakaeda et al. 2017). However, at least over the domain considered here, a statistically significant modulation of both the diurnal cycle and the daily mean precipitation rate by the BSISO is found from spatial averages over the landmasses.

Intraseasonal variability was also found in the diurnal cycle over the coastal regions of the SCS and Moro Gulf affected by westward propagation of diurnal convection from the major islands. Offshore propagation is most favored in the transition from inactive to the active phase, and into the early part of the active phase, while the latter part of the active phase sees a suppressed diurnal cycle and significantly diminished propagation offshore. Additionally, this study has identified a disparity in the impact of the BSISO on the diurnal cycle between eastern and western aspects of Philippine islands in the presence of topography. While the diurnal cycle over and west of the high topography of Luzon and Mindanao peaks in the expected pre-onset BSISO period, the eastern side of the islands concurrently observe their weakest diurnal cycles. This cautions against spatially averaging over an entire island in future studies, because two different signals could be blended together. Here, the least active diurnal cycle is found in the transition to active phase, and the highest amplitude at the conclusion of the active phase. The modulation of the land-based and coastal diurnal cycles by the BSISO are consistent across several satellite derived precipitation datasets, do not depend on the BSISO index used, and are statistically significant.

In Chapter 4, it was shown that this strong diurnal cycle occurs in concert with increased surface insolation and weak onshore intraseasonal winds. Evidence relating this pattern to frictional moisture convergence was not found. The importance of the wind profile in driving diurnal propagation of convection has been explored in the past (Saito et al. 2001, Ichiwaka and Yasunari 2006, 2008, Tulich and Kiladis 2012). In the late-suppressed period (L13 phases 3-4), the easterly trades impinging on the eastern Philippines reach their peak, while intraseasonal winds are weakly offshore on the western shore. Concurrently, the diurnal cycle is maximized over and west of topography, and minimized on the east coast. Conversely, in the late-active period (L13 phases 7-8), the diurnal cycle over western Luzon and Mindanao and nearby coastal waters is at a minimum, concurrent with strong onshore low-level southwesterly winds associated with the BSISO and monsoon trough. It is proposed that strong onshore daily mean flow overwhelms the sea-breeze circulation over islands, and weakens the diurnal cycle (Fujita et al. 2011, Oh et al. 2012). However, more exploration of this hypothesis is required in order to differentiate the effects of prevailing wind from those of insolation, beyond showing that the strong diurnal cycles and weak onshore winds are collocated in time and space. Similarly, strong insolation due to suppressed cloudiness promotes a robust sea-breeze circulation during the BSISO suppressed period.

Many prior studies have shown that an increase in moisture in the lower-free troposphere to the mid-levels is an important precursor to convection (Bretherton et al. 2004, Holloway and Neelin 2009, 2010, Yuan and Houze 2013), and that such an increase is found leading ISO convection (Hsu et al. 2004, Jiang et al. 2004, R. Johnson and Ciesielski 2013, Adames and Wallace 2015, Jiang et al. 2018). This motivated an exploration of BSISO modulation of such moisture in the vicinity of Luzon in Mindanao. An increase in moisture around 700- to 900-hPa was found on the west side of the islands during phases in which convection is expected to propagate offshore (the transition from suppressed to active BSISO state). Furthermore, this was shown to lead BSISO convection over the entire warm pool, not just in these regions. Thus, prevailing winds, insolation, and moisture near 850-hPa all contribute to a strong diurnal cycle during the suppressed period of the BSISO that then propagates offshore to the west just prior to onset. The existence of a feedback mechanism related to offshore propagation of the diurnal cycle that helps moisten the SCS for large-scale convection at all hours of the day is also hypothesized. This could assist in northward propagation of the BSISO if its physics are described by a moisture mode, but this question is again left for future research.

5.2 Future Work

The results presented here build on those established by Peatman et al. (2014) for the wintertime MJO near Sumatra and Borneo. A possible mechanism is proposed, but future work will be needed to clarify if indeed the weak prevailing winds, strong insolation, and neutral moisture anomalies in the transition phases leads to a strong, propagating diurnal cycle. Furthermore, if that is the case, the question of how and why the BSISO influences mid-level moisture must also be answered. The potential 2019 followup to the PISTON field campaign as well as CAMP3Ex may be able to address the question of whether increasing moisture permits a propagating diurnal cycle, or a propagating diurnal cycle increases mid-level moisture. This data on the ground would also help to establish how surface winds, mid-level moisture, and insolation all interact with the diurnal cycle over land and its offshore propagation.

Future work could attack these questions even without measurements on the ground. Following this project, lag-correlations could be performed between moisture anomalies, wind anomalies, and diurnal cycle amplitude to see if a lead-lag relationship can be extracted. Additionally, when ERA5 is completely released in the next few months, a follow-up with the new and improved reanalysis dataset would be beneficial, to see if a better product with higher resolution can reveal any more information.

A potential modeling study is proposed to address the causes of the observed modulation of the diurnal cycle. Using a regional model like WRF over the Philippines, one or multiple BSISO events in which a propagating diurnal cycle was observed during the transition period could be simulated. The model could be run twice, first as a control run forced with reanalysis, and second as an experiment forced on the boundaries by reanalysis, but with all intraseasonal signals filtered out. Such an analysis would reveal the importance of intra-seasonal forcing on a propagating diurnal cycle. Furthermore, sensitivity tests could be done to explore the relative contributions of insolation and moisture by constraining one, while allowing the other to vary freely. The importance of topography in driving the disparity between eastern and western portions of the islands could be tested by flattening the mountains in the model, assuming that the model reproduces this disparity. This could illuminate whether upslope/downslope flow related to the intraseasonal flow is modulating insolation.

All of these proposed experiments still only address the question of how and why the BSISO influences the diurnal cycle. An interesting followup question comes from the reverse direction. Can the propagating diurnal cycle actually feedback onto the ISO and assist in its own propagation to the northeast? It is possible that enhanced offshore propagation of the diurnal cycle prior to and during BSISO onset helps to determine successful propagation through the MC through a feedback mechanism that further increases moisture content in the mid-levels. To test this hypothesis, a lead-lag relationship between observed offshore propagation from the islands of the MC, and a successful propagating ISO event through would be considered. One way to address this would be to create an index describing offshore propagation strength for each island of interest, or multiple islands together, and correlate it with the principal components of any of the BSISO indices discussed in this thesis. While this thesis has built on and revised hypotheses established in prior work as well as extended such results to the boreal summer season and the Philippines, much more work is required to develop a theory that works for all seasons and all MC islands.

References

Ackerman, S. A. and S. K. Cox, 1981: Comparison of satellite and all-sky camera estimates of cloud cover during GATE. *J. Appl. Meteor.*, **20**, 581-587.

Adames, Á. F., and J. M. Wallace, 2015: Three-dimensional structure and evolution of the moisture field in the MJO. *J. Atmos. Sci.*, **72**, 3733-3754.

Adames, Á. F. and D. Kim, 2016: The MJO as a dispersive, convectively coupled moisture wave: Theory and observations. *J. Atmos. Sci.*, **73**, 913-941.

Albright, M. D., E. E. Recker, and R. J. Reed, 1985: The diurnal variation of deep convection and inferred precipitation in the central tropical Pacific during January-February 1979. *Mon. Wea. Rev.*, **113**, 1663-1680.

Augustine, J. A., 1984: The diurnal variation of large-scale inferred rainfall over the tropical Pacific Ocean during August 1979. *Mon. Wea. Rev.*, **112**, 1745-1751.

Barnes, H. C., and R. A. Houze, 2013: The precipitating cloud population of the Madden-Julian oscillation over the Indian and west Pacific Oceans. *J. Geophys. Res. Atmos.*, **118**, 6996-7023.

Bernie, D. J., E. Guilyardi, G. Madec, J. M. Slingo, S. J. Woolnough, and J. Cole, 2008: Impact of resolving the diurnal cycle in an ocean-atmosphere GCM. Part 2: A diurnally coupled CGCM. *Climate Dyn.*, **31**, 909-925.

Biasutti, M., S. E. Yuter, C. D. Burleyson, and A. H. Sobel, 2012: Very high resolution rainfall patterns measured by TRMM Precipitation Radar: Seasonal and diurnal cycles. *Climate Dyn.*, **39**, 239-258.

Birch, C. E., M. J. Roberts, L. Garcia-Carreras, D. Ackerley, M. J. Reeder, A. P. Lock, and R. Schiemann, 2015: Sea-breeze dynamics and convection initiation: The influence of convective parameterization in weather and climate model biases. *J. Climate*, **28**, 8093-8108.

Birch, C. E., S. Webster, S. C. Peatman, D. J. Parker, A. J. Matthews, Y. Li, and M. E. E. Hassim, 2016: Scale interactions between the MJO and the western Maritime Continent. *J. Climate*, **29**, 2471-2492.

Bretherton, C. S., M. E. Peters, and L. E. Back, 2004: Relationships between water vapor path and precipitation over the tropical oceans. *J. Climate*, **17**, 1517-1528.

Brier, G. W., and J. Simpson, 1969: Tropical cloudiness and rainfall related to pressure and tidal variations. *Quart. J. Roy. Meteor. Soc.*, **95**, 120-147.

Cairns, B., 1995: Diurnal variations of cloud from ISCCP data. *Atmos. Res.*, **37**, 133-146.

Carbone, R. E. and J. D. Tuttle, 2008: Rainfall occurrence in the U.S. warm season: The diurnal cycle. *J. Climate*, **21**, 4132-4146.

Chen, S. S., and R. A. Houze Jr., 1997: Diurnal variation and lifecycle of deep convective systems over the tropical Pacific warm pool. *Quart. J. Roy. Meteor. Soc.*, **123**, 357-388.

Dai, A., 2001: Global precipitation and thunderstorm frequencies. Part II: Diurnal variations. *J. Climate*, **14**, 1112-1128

Dai, A., X. Lin, and K.-L. Hsu, 2007: The frequency, intensity, and diurnal cycle of precipitation in surface and satellite observations over low- and mid-latitudes. *Climate Dyn.*, **29**, 727-744.

Dee, D. P., and Coauthors, 2011: The ERA-Interim reanalysis: Configuration and performance of the data assimilation system. *Quart. J. Roy. Meteor. Soc.*, **137**, 553-597.

DeMott, C.A., C. Stan, and D.A. Randall, 2013: Northward propagation mechanisms of the Boreal Summer Intraseasonal Oscillation in the ERA-Interim and SP-CCSM. *J. Climate*, **26**, 1973-1992.

Deser, C. and C. A. Smith, 1998: Diurnal and semidiurnal variations of the surface wind field over the tropical Pacific Ocean. *J. Climate*, **11**, 1730-1748.

Dias, J., S. Leroux, S. N. Tulich, and G. N. Kiladis, 2013: How systematic is organized tropical convection within the MJO? *Geophys. Res. Lett.*, **40**, 1420-1425.

Dias, J., N. Sakaeda, G. N. Kiladis, and K. Kikuchi, 2017: Influences of the MJO on the space-time organization of tropical convection. *J. Geophys. Res. Atmos.*, **122**, 8012-8032.

Dinku, T., S. Chidzambwa, P. Ceccato, S. J. Connor, and C. F. Ropelewski, 2008: Validation of high-resolution satellite rainfall products over complex terrain, *Int. J. Remote Sens.*, **29**, 4097-4110.

Duchon, C. E., 1979: Lanczos filtering in one and two dimensions. *J. Appl. Meteor.*, **18**, 1016-1022.

EUMETSAT/OSI SAF, 2010: MetOp-A ASCAT Level 2 Ocean Surface Wind Vectors Optimized for Coastal Ocean. Ver. Operational/Near-Real-Time. PO.DAAC, CA, USA, accessed 6 June 2017 at ftp://podaac-ftp.jpl.nasa.gov/allData/ascat/preview/L2/metop_a/coastal_opt/

Feng, Z., S. Hagos, A. K. Rowe, C. D. Burleyson, M. N. Martini, and S. P. de Szoeke, 2015: Mechanisms of convective cloud organization by cold pools over tropical warm ocean during the AMIE/DYNAMO field campaign. *J. Adv. Model. Earth Syst.*, **7**, 357-381.

Foltz, G. S. and W. M. Gray, 1979: Diurnal variation in the troposphere's energy balance. *J. Atmos. Sci.*, **36**, 1450-1466

Fujita, M., K. Yoneyama, S. Mori, T. Nasuno, and M. Satoh, 2011: Diurnal convection peaks over the eastern Indian Ocean off Sumatra during different MJO phases. *J. Meteor. Soc. Japan*, **89A**, 317-330.

Gill, A. E., 1980: Some simple solutions for heat-induced tropical circulation. *Quart. J. Roy. Meteor. Soc.*, **106**, 447-462.

Gray, W. M. and R. W. Jacobson, 1977: Diurnal variation of deep cumulus convection. *Mon. Wea. Rev.*, **105**, 1171-1188.

Hagos, S. M., C. Zhang, Z. Feng, C. D. Burleyson, C. DeMott, B. Kerns, J. J. Benedict, and M. N. Martini, 2016: The impact of the diurnal cycle on the propagation of Madden-Julian oscillation convection across the maritime continent. *J. Adv. Model. Earth Syst.*, **8**, 1552-1564.

Hartmann, D. L., and E. E. Recker, 1986: Diurnal variation of outgoing longwave radiation in the tropics. *J. Climate Appl. Meteor.*, **25**, 800-812.

Hassim, M. E. E., T. P. Lane, and W. W. Grabowski, 2016: The diurnal cycle of rainfall over New Guinea in convection-permitting WRF simulations. *Atmos. Chem. Phys.*, **16**, 161-175.

Hayashi, M. and H. Itoh, 2017: A new mechanism of the slow eastward propagation of unstable disturbances with convection in the tropics: Implications for the MJO. *J. Atmos. Sci.*, **74**, 3749-3769.

Hendon, H. H., and B. Liebmann, 1994: Organization of convection within the Madden-Julian oscillation. *J. Geophys. Res.*, **99**, 8073-8083.

Hendon, H. H., and M. L. Salby, 1994: The life cycle of the Madden-Julian Oscillation. *J. Atmos. Sci.*, **51**, 2225-2237.

Holloway, C. E. and J. D. Neelin, 2009: Moisture vertical structure, column water vapor, and tropical deep convection. *J. Atmos. Sci.*, **66**, 1665-1683.

Holloway, C. E. and J. D. Neelin, 2010: Temporal relations of column water vapor and tropical precipitation. *J. Atmos. Sci.*, **67**, 1091-1105.

Houze, R. A., S. G. Geotis, F. D. Marks Jr, and A. K. West, 1981: Winter monsoon convection in the vicinity of north Borneo. Part I: Structure and time variation of the clouds and precipitation. *Mon. Wea. Rev.*, **109**, 1595-1614.

Hsu, H.-H., C. Weng, and C. Wu, 2004: Contrasting characteristics between the northward and eastward propagation of the Intraseasonal Oscillation during the boreal summer. *J. Climate*, **17**, 727-743.

Hsu, P.-C., and T. Li, 2012: Role of the boundary layer moisture asymmetry in causing the eastward propagation of the Madden-Julian oscillation. *J. Climate*, **25**, 4914-4931.

Hsu, P.-C., J. Lee, K. Ha, and C. Tsou, 2017: Influences of Boreal Summer Intraseasonal Oscillation on heat waves in monsoon Asia. *J. Climate*, **30**, 7191-7211.

Huffman, G. J., and Coauthors, 2007: The TRMM Multisatellite Precipitation Analysis (TMPA): Quasi-global, multiyear, combined-sensor precipitation estimates at fine scales. *J. Hydrometeor.*, **8**, 38-55.

Huffman, G. J., D. T. Bolvin, D. Braithwaite, K. Hsu, R. Joyce, C. Kidd, E. J. Nelkin, S. Sorooshian, J. Tan, P. Xie, 2014: Integrated Multi-satellitE Retrievals for GPM (IMERG), version 5.2. NASA's Precipitation Processing Center, accessed 31 January 2018 at ftp://arthurhou.pps.eosdis.nasa.gov/gpmdata/.

Hughes, M., A. Hall, and R. G. Fovell, 2007: Dynamic controls on the diurnal cycle of temperature in complex topography. *Climate Dyn.*, **29**, 277-292

Ichikawa, H., and T. Yasunari, 2006: Time-space characteristics of diurnal rainfall over Borneo and surrounding oceans as observed by TRMM-PR. *J. Climate*, **19**, 1238-1260.

Ichikawa, H., and T. Yasunari, 2008: Intraseasonal variability in diurnal rainfall over New Guinea and the surrounding oceans during austral summer. *J. Climate*, **21**, 2852-2868.

Iguchi, T., T. Kozu, R. Meneghini, J. Awaka, and K. Okamoto, 2000: Rain-profiling algorithm for the TRMM Precipitation Radar. *J. Appl. Meteor.*, **39**, 2038-2052.

Janowiak, J. E., P. A. Arkin, and M. Morrissey, 1994: An examination of the diurnal cycle in oceanic tropical rainfall using satellite and in situ data. *Mon. Wea. Rev.*, **122**, 2296-2311.

Jiang, X., T. Li, and B. Wang, 2004: Structures and mechanisms of the northward propagating boreal summer intraseasonal oscillation. *J. Climate*, **17**, 1022-1039.

Jiang, X., Á. F. Adames, M. Zhao, D. Waliser, and E. Maloney, 2018: A unified moisture mode framework for seasonality of the Madden-Julian Oscillation. *J. Climate*, **31**, 4215-4224.

Johnson, R. H., T. M. Rickenbach, S. A. Rutledge, P. E. Ciesielski, and W. H. Schubert, 1999: Trimodal characteristics of tropical convection. *J. Climate*, **12**, 2397-2418.

Johnson, R. H., and P. E. Ciesielski, 2013: Structure and properties of Madden-Julian oscillations deduced from DYNAMO sounding arrays. *J. Atmos. Sci.*, **70**, 3157-3179.

Johnson. S. J., R. C. Levine, A. G. Turner, G. M. Martin, S. J. Woolnough, R. Schiemann, M. S. Mizielinski, M. J. Roberts, P. L. Vidale, M.-E. Demory, J. Strachan, 2016 - The resolution sensitivity of the South Asian monsoon and Indo-Pacific in a global 0.35° AGCM. *Climate Dyn.*, **46**, 807-831.

Jones, C., L. M. V. Carvalho, R. W. Higgins, D. E. Waliser, and J.- K. E. Schemm, 2004: Climatology of tropical intraseasonal convective anomalies: 1979-2002. *J. Climate*, **17**, 523-539.

Joyce, R. J., J. E. Janowiak, P. A. Arkin, and P. Xie, 2004: CMORPH: A method that produces global precipitation estimates from passive microwave and infrared data at high spatial and temporal resolution. *J. Hydrometeor.*, **5**, 487-503.

Kanamori, H., T. Yasunari, and K. Kuraji, 2013: Modulation of the diurnal cycle of rainfall associated with the MJO observed by a dense hourly rain gauge network at Sarawak, Borneo. *J. Climate*, **26**, 4858-4875.

Keenan, T. D., and R. E. Carbone, 2008: Propagation and diurnal evolution of warm season cloudiness in the Australian and Maritime Continent region. *Mon. Wea. Rev.*, **136**, 973-994.

Kemball-Cook, S. R., and B. Wang, 2001: Equatorial waves and air-sea interaction in the boreal summer intraseasonal oscillation. *J. Climate*, **14**, 2923-2942.

Kikuchi, K., and B. Wang, 2008: Diurnal precipitation regimes in the global tropics. *J. Climate*, **21**, 2680-2696.

Kikuchi, K., B. Wang, and Y. Kajikawa, 2012: Bimodal representation of the tropical intraseasonal oscillation. *Climate Dyn.*, **38**, 1989-2000.

Kiladis, G. N., K. H. Straub, and P. T. Haertel, 2005: Zonal and vertical structure of the Madden-Julian Oscillation. *J. Atmos. Sci.*, **62**, 2790-2809.

Kiladis, G. N., J. Dias, K. H. Straub, M. C. Wheeler, S. N. Tulich, K. Kikuchi, K. M. Weickmann, and M. J. Ventrice, 2014: A comparison of OLR and circulation-based indices for tracking the MJO. *Mon. Wea. Rev.*, **142**, 1697-1715.

Kim, D., J.-S. Kug, and A. H. Sobel, 2014: Propagating versus nonpropagating Madden-Julian oscillation events. *J. Climate*, **27**, 111-125.

Kim, D., M.-S. Ahn, I.-S. Kang, and A. D. Del Genio, 2015: Role of longwave cloudrradiation feedback in the simulation of the Madden-Julian oscillation. *J. Climate*, **28**, 6979-6994.

Kim, H., D. Kim, F. Vitart, V. E. Toma, J. Kug, and P. J. Webster, 2016: MJO Propagation across the Maritime Continent in the ECMWF Ensemble Prediction System. *J. Climate*, **29**, 3973-3988.

Klotzbach, P. J., J. C. Chan, P. J. Fitzpatrick, W. M. Frank, C. W. Landsea, and J. L. McBride, 2017: The science of William M. Gray: His contributions to the knowledge of tropical meteorology and tropical cyclones. *Bull. Amer. Meteor. Soc.*, **98**, 2311-2336.

Knutson, T. R. and K. M. Weickmann, 1987: 30-60 Day atmospheric oscillations: composite life cycles of convection and circulation anomalies. *Mon. Wea. Rev.*, **115**, 1407-1436.

Kousky, V. E., 1980: Diurnal rainfall variation in northeast Brazil. *Mon. Wea. Rev.*, **108**, 488-498.

Kraus, E. B., 1963: The diurnal precipitation change over the sea. *J. Atmos. Sci.*, **20**, 551-556.

Lang, T. J., 2017: Investigating the seasonal and diurnal cycles of ocean vector winds near the Philippines using RapidScat and CCMP. *J. Geophys. Res. Atmos.*, **122**, 9668-9684.

Lau, K.-M., and P. H. Chan, 1986: Aspects of the 40-50 day oscillation during the northern summer as inferred from outgoing longwave radiation. *Mon. Wea. Rev.*, **114**, 1354-1367.

Lawrence, D. M. and P. J. Webster, 2002: The Boreal Summer Intraseasonal Oscillation: Relationship between northward and eastward movement of convection. *J. Atmos. Sci.*, **59**, 1593-1606.

Lee, J.-Y., B. Wang, M.C. Wheeler, X. Fu, D.E. Waliser, and I.-S. Kang, 2013: Real-time multivariate indices for the boreal summer intraseasonal oscillation over the Asian summer monsoon region. *Climate Dyn.* **40**, 493-509.

Liebmann, B., and C. A. Smith, 1996: Description of a complete (interpolated) outgoing longwave radiation dataset. *Bull. Amer. Meteor. Soc.*, **77**, 1275-1277.

Lin, X., and R. H. Johnson, 1996: Heating, moistening, and rainfall over the western Pacific warm pool during TOGA COARE. *J. Atmos. Sci.*, **53**, 3367-3383.

Lindzen, R. S., 1978: Effect of daily variations of cumulonimbus activity on the atmospheric semidiurnal tide. *Mon. Wea. Rev.*, **106**, 526-533.

Liu, C. and M. W. Moncrieff, 1998: A numerical study of the diurnal cycle of tropical oceanic convection. *J. Atmos. Sci.*, **55**, 2329-2344.

Love, B. S., A. J. Matthews, and G. M. S. Lister, 2011: The diurnal cycle of precipitation over the Maritime Continent in a high resolution atmospheric model. *Quart. J. Roy. Meteor. Soc.*,**137**, 934-947.

Madden, R. A., and P. R. Julian, 1971: Detection of a 40-50 day oscillation in the zonal wind in the tropical Pacific. *J. Atmos. Sci.*, **28**, 702-708.

Madden, R. A., and P. R. Julian, 1972: Description of global-scale circulation cells in the tropics with a 40-50 day period. *J. Atmos. Sci.*, **29**, 1109-1123.

Madden, R. A. and P. R. Julian, 1994: Observations of the 40-50-Day Tropical Oscillation - A review. *Mon. Wea. Rev.*, **22**, 814-837.

Majda, A. J., and S. N. Stechmann, 2009: The skeleton of tropical intraseasonal oscillations. *Proc. Natl. Acad. Sci. USA*, **106**, 8417-8422.

Majda, A. J., and Q. Yang, 2016: A multiscale model for the intraseasonal impact of the diurnal cycle over the Maritime Continent on the Madden-Julian oscillation. *J. Atmos. Sci.*, **73**, 579-604.

Maloney, E. D., and D. L. Hartmann, 1998: Frictional moisture convergence in a composite life cycle of the Madden-Julian oscillation. *J. Climate*, **11**, 2387-2403.

Maloney, E. D., and D. L. Hartmann, 2001: The Madden-Julian oscillation, barotropic dynamics, and North Pacific tropical cyclone formation. Part I: Observations. *J. Atmos. Sci.*, **58**, 2545-2558.

Maloney, E. D. and M.J. Dickinson, 2003: The Intraseasonal Oscillation and the energetics of summertime tropical western North Pacific synoptic-scale disturbances. *J. Atmos. Sci.*, **60**, 2153-2168.

Maloney, E. D., 2009: The moist static energy budget of a composite tropical intraseasonal oscillation in a climate model. *J. Climate*, **22**, 711-729.

Mapes, B. E., T. T. Warner, M. Xu, and A. J. Negri, 2003a: Diurnal patterns of rainfall in northwestern South America. Part I: Observations and context. *Mon. Wea. Rev.*, **131**, 799-812.

Mapes, B. E., T. T. Warner, and M. Xu, 2003b: Diurnal patterns of rainfall in northwestern South America. Part III: Diurnal gravity waves and nocturnal convection offshore. *Mon. Wea. Rev.*, **131**, 830-844.

Matsuno, T., 1966: Quasi-geostrophic motions in the equatorial area. *J. Meteor. Soc. Japan*, **44**, 25-43.

Matthews, A. J., 2000: Propagation mechanisms for the Madden-Julian Oscillation. *Quart. J. Roy. Meteor. Soc.*, **126**, 2637-2651.

Matthews, A. J., B. J. Hoskins, and M. Masutani, 2004: The global response to tropical heating in the Madden-Julian oscillation during the northern winter. *Quart. J. Roy. Meteor. Soc.*, **130**, 1991-2011.

Matthews, A. J., G. Pickup, S. C. Peatman, P. Clews, and J. Martin, 2013: The effect of the Madden-Julian oscillation on station rainfall and river level in the Fly River system, Papua New Guinea. *J. Geophys. Res. Atmos.*, **118**, 10926-10935.

Matthews, A. J., D. B. Baranowski, K. J. Heywood, P. J. Flatau, and S. Schmidtko, 2014: The surface diurnal warm layer in the Indian Ocean during CINDY/DYNAMO. *J. Climate*, **27**, 9101-9122.

McBride, J. L., and W. M. Gray, 1980: Mass divergence in tropical weather systems. Paper I: Diurnal variation. *Quart. J. Roy. Meteor. Soc.*, **106**, 501-516.

Mori, S., H. Jun-Ichi, Y. I. Tauhid, M. D. Yamanaka, N. Okamoto, F. Murata, N. Sakurai, H. Hashiguchi, and T. Sribimawati, 2004: Diurnal land-sea rainfall peak migration over Sumatera Island, Indonesian Maritime Continent, observed by TRMM satellite and intensive rawinsonde soundings. *Mon. Wea. Rev.*, **132**, 2021-2039.

Myers, D. S., and D. E. Waliser, 2003: Three-dimensional water vapor and cloud variations associated with the Madden-Julian oscillation during Northern Hemisphere winter. *J. Climate*, **16**, 929-950.

National Geophysical Data Center, 2006: 2-minute Gridded Global Relief Data (ETOPO2) v2. National Geophysical Data Center, NOAA, accessed 12 February 2018 at doi:10.7289/V5J1012Q

Neale, R., and J. Slingo, 2003: The Maritime Continent and its role in the global climate: A GCM study. *J. Climate*, **16**, 834-848.

Nesbitt, S. W., and E. J. Zipser, 2003: The diurnal cycle of rainfall and convective intensity according to three years of TRMM measurements. *J. Climate*, **16**, 1456-1475.

Nesbitt, S. W., D. J. Gochis, and T. J. Lang, 2008: The diurnal cycle of clouds and precipitation along the Sierra Madre Occidental observed during NAME-2004: Implications for warm season precipitation estimation in complex terrain. *J. Hydrometeor.*, **9**, 728-743.

Nitta, T., and S. Sekine, 1994: Diurnal variation of convective activity over the tropical western Pacific. *J. Meteor. Soc. Japan*, **72**, 627-641.

Oh, J.-H., K.-Y. Kim, and G.-H. Lim, 2012: Impact of MJO on the diurnal cycle of rainfall over the western Maritime Continent in the austral summer. *Climate Dyn.*, **38**, 1167-1180.

Ohsawa, T., H. Ueda, T. Hayashi, A. Watanabe, and J. Matsumoto, 2001: Diurnal variations of convective activity and rainfall in tropical Asia. *J. Meteor. Soc. Japan*, **79B**, 333-352.

Peatman, S. C., A. J. Matthews, and D. P. Stevens, 2014: Propagation of the Madden-Julian Oscillation through the Maritime Continent and scale interaction with the diurnal cycle of precipitation. *Quart. J. Roy. Meteor. Soc.*, **140**, 814-825.

Pielke, R.A., 1974: A three-dimensional numerical model of the sea breezes over south Florida. *Mon. Wea. Rev.*, **102**, 115-139.

Powell, S. W., and R. A. Houze, 2013: The cloud population and onset of the Madden-Julian Oscillation over the Indian Ocean during DYNAMO-AMIE. *J. Geophys. Res. Atmos.*, **118**, 11979-11995.

Powell, S. W., and R. A. Houze, 2015: Evolution of precipitation and convective echo top heights observed by TRMM radar over the Indian Ocean during DYNAMO. *J. Geophys. Res. Atmos.*, **120**, 3906-3919.

Qian, J., 2008: Why precipitation is mostly concentrated over islands in the Maritime Continent. *J. Atmos. Sci.*, **65**, 1428-1441.

Ramage, C. S., 1968: Role of a tropical "Maritime Continent" in the atmospheric circulation. *Mon. Wea. Rev.*, **96**, 365-370.

Rampanelli, G., D. Zardi, and R. Rotunno, 2004: Mechanisms of up-valley winds. *J. Atmos. Sci.*, **61**, 3097-3111.

Randall, D. A., Harshvardhan, and D. A. Dazlich, 1991: Diurnal Variability of the Hydrologic Cycle in a General Circulation Model. *J. Atmos. Sci.*, **48**, 40-62.

RapidScat Project, 2016: RapidScat level 2B climate ocean wind vectors in 12.5 km footprints. Ver. 1.0. PO.DAAC, CA, USA, accessed 19 July 2017 at https://doi.org/10.5067/RSX12-L2C11

Rauniyar, S. P., and K. J. E. Walsh, 2011: Scale interaction of the diurnal cycle of rainfall over the Maritime Continent and Australia: Influence of the MJO. *J. Climate*, **24**, 325-348

Raupp, C. F. M., and P. L. Silva Dias, 2009: Resonant wave interactions in the presence of a diurnally varying heat source. *J. Atmos. Sci.*, **66**, 3165-3183.

Raymond, D. J., 2000: Thermodynamic control of tropical rainfall. *Quart. J. Roy. Meteor. Soc.*, **126**, 889-898.

Raymond, D. J., 2001: A new model of the Madden-Julian oscillation. *J. Atmos. Sci.*, **58**, 2807-2819.

Raymond, D. J., and Ž. Fuchs, 2009: Moisture modes and the Madden-Julian oscillation. *J. Climate*, **22**, 3031-3046.

Romilly, T. G., and M. Gebremichael, 2011: Evaluation of satellite rainfall estimates over Ethiopian river basins. *Hydrol. Earth Syst. Sci.*, **15**, 1505-1514.

Rowe, A. K., and R. A. Houze, 2015: Cloud organization and growth during the transition from suppressed to active MJO conditions. *J. Geophys. Res. Atmos.*, **120**, 10324-10350

Ruppert, J. H., and R. H. Johnson, 2015: Diurnally modulated cumulus moistening in the preonset stage of the Madden-Julian oscillation during DYNAMO. *J. Atmos. Sci.*, **72**, 1622-1647.

Ruppert, J. H., and R. H. Johnson, 2016: On the cumulus diurnal cycle over the tropical warm pool. *J. Adv. Model. Earth Syst.*, **8**, 669-690.

Saito, K., T. Keenan, G. Holland, and K. Puri, 2001: Numerical simulation of the diurnal evolution of tropical island convection over the maritime continent. *Mon. Wea. Rev.*, **129**, 378-400.

Sakaeda, N., G. N. Kiladis, and J. Dias, 2017: The diurnal cycle of tropical cloudiness and rainfall associated with the Madden-Julian Oscillation. *J. Climate*, **30**, 3999-4020.

Sakaeda, N., S. W. Powell, J. Dias, and G. N. Kiladis, 2018: The diurnal variability of precipitating cloud populations during DYNAMO. *J. Atmos. Sci.*, **75**, 1307-1326.

Sakurai, N., and Coauthors, 2005: Diurnal cycle of cloud system migration over Sumatera Island. *J. Meteor. Soc. Japan*, **83**, 835-850.

SeaPAC, 2016: QuikSCAT Level 2B Ocean Wind Vectors in 12.5km Slice Composites Version 3.1. PO.DAAC, CA, USA, accessed 31 May 2017 at ftp://podaac-ftp.jpl.nasa.gov/allData/quikscat/L2B12/v3.1

Sengupta, D., B. N. Goswami, and R. Senan, 2001: Coherent intraseasonal oscillations of ocean and atmosphere during the Asian summer monsoon. *Geophys. Res. Lett.*, **28**, 4127-4130.

Slingo, J., P. Inness, R. Neale, S. Woolnough, and G. Yang, 2003: Scale interactions on diurnal to seasonal timescales and their relevance to model systematic errors. *Ann. Geophys.*, **46**, 139-155.

Sobel, A. H., J. Nilsson, and L. M. Polvani, 2001: The weak temperature gradient approximation and balanced tropical moisture waves. *J. Atmos. Sci.*, **58**, 3650-3665.

Sobel, A. H. and E. D. Maloney, 2000: Effect of ENSO and the MJO on western North Pacific tropical cyclones. *Geophys. Res. Lett.*, **27**,1739-1742.

Sobel, A. H., and E. D. Maloney, 2012: An idealized semi-empirical framework for modeling the Madden-Julian oscillation. *J. Atmos. Sci.*, **69**, 1691-1705.

Sobel, A. H., and E. D. Maloney, 2013: Moisture modes and the eastward propagation of the MJO. *J. Atmos. Sci.*, **70**, 187-192.

Sobel, A. H., S. Wang, and D. Kim, 2014: Moist static energy budget of the MJO during DYNAMO. *J. Atmos. Sci.*, **71**, 4276-4291.

Straub, K. H., and G. N. Kiladis, 2003: Interactions between the boreal summer intraseasonal oscillation and higher-frequency tropical wave activity. *Mon. Wea. Rev.*, **131**, 945-960.

Sui, C.-H., and K.-M. Lau, 1992: Multiscale phenomena in the tropical atmosphere over the western Pacific. *Mon. Wea. Rev.*, **120**, 407-430.

Sui, C.-H., Y. N. Takayabu, and D. A. Short, 1997: Diurnal variations in tropical oceanic cumulus convection during TOGA COARE. *J. Atmos. Sci.*, **54**, 639-655.

Tabata, Y., H. Hashiguchia, M. K. Yamamoto, M. Yamamoto, M. D. Yamanaka, S. Mori, F. Syamsudinc, and T. Manik, 2011: Observational study on diurnal precipitation cycle in equatorial Indonesia using 1.3-GHz wind profiling radar network and TRMM Precipitation Radar. *J. Atmos. Sol. Terr. Phys.*, **73**, 1031-1042.

Tan. J., W. A. Peterson, P.-E. Kirstetter, and Y. Tian, 2017: Performance of IMERG as a function of spatiotemporal scale. *J. Hydrometeor.*, **18**, 307-319.

Tseng, K.-C., C.-H. Sui, and T. Li, 2015: Moistening processes for Madden-Julian oscillations during DYNAMO/CINDY. *J. Climate*, **28**, 3041-3057.

Tulich, S. N., and G. N. Kiladis, 2012: Squall lines and convectively coupled gravity waves in the tropics: Why do most cloud systems propagate westward? *J. Atmos. Sci.*, **69**, 2995-3012.

Vincent, C. L., and T. P. Lane, 2016: Evolution of the diurnal precipitation cycle with the passage of a Madden-Julian Oscillation event through the Maritime Continent. *Mon. Wea. Rev.*, **144**, 1983-2005.

Vincent, C. L., T. P. Lane, and M. C. Wheeler, 2016: A local index of Maritime Continent intraseasonal variability based on rain rates over the land and sea. *Geophys. Res. Lett.*, **43**, 9306-9314.

Wallace, J. M., 1975: Diurnal Variations in Precipitation and Thunderstorm Frequency over the Conterminous United States. *Mon. Wea. Rev.*, **103**, 406-419.

Wang, S., Ma, D., Sobel, A. H., and Tippett, M. K., 2018: Propagation characteristics of BSISO indices. *Geophys. Res. Lett.*, **45**, 9934-9943.

Wheeler, M., and G. Kiladis, 1999: Convectively coupled equatorial waves: Analysis of clouds in the wavenumber-frequency domain. *J. Atmos. Sci.*, **56**, 374-399.

Wheeler, M., and H. H. Hendon, 2004: An all-season real-time multivariate MJO index: Development of an index for monitoring and prediction. *Mon. Wea. Rev.*, **132**, 1917-1932.

Xu, W. and S. A. Rutledge, 2014: Convective characteristics of the Madden-Julian oscillation over the central Indian Ocean observed by shipborne radar during DYNAMO. *J. Atmos. Sci.*, **71**, 2859-2877.

Xu, W. and S. A. Rutledge, 2018: Convective variability associated with the Boreal Summer Intraseasonal Oscillation in the South China Sea region. *J. Climate*, **31**, 7363-7383.

Yamamoto, M. K., F. A. Furuzawa, A. Higuchi, and K. Nakamura, 2008: Comparison of diurnal variations in precipitation systems observed by TRMM PR, TMI, and VIRS. *J. Climate*, **21**, 4011-4028.

Yanase, A., K. Yasunaga, and H. Masunaga, 2017: Relationship between the direction of diurnal rainfall migration and the ambient wind over the Southern Sumatra Island. *Earth and Space Science*, **4**, 117-127.

Yang, D., and A. P. Ingersoll, 2011: Testing the hypothesis that the MJO is a mixed Rossby-gravity wave packet. *J. Atmos. Sci.*, **68**, 226-239.

Yang, D., and A. P. Ingersoll, 2013: Triggered convection, gravity waves, and the MJO: A shallow-water model. *J. Atmos. Sci.*, **70**, 2476-2486.

Yang, G.-Y., and J. Slingo, 2001: The diurnal cycle in the tropics. *Mon. Wea. Rev.*, **129**, 784-801.

Yang, S., and E. A. Smith, 2006: Mechanisms for diurnal variability of global tropical rainfall observed from TRMM. *J. Climate*, **19**, 5190-5226.

Yang, S., and E. A. Smith, 2008: Convective-stratiform precipitation variability at seasonal scale from 8 yr of TRMM observations: Implications for multiple modes of diurnal variability. *J. Climate*, **21**, 4087-4114.

Yuan, J. and R. A. Houze, 2013: Deep convective systems observed by A-Train in the tropical Indo-Pacific Region affected by the MJO. *J. Atmos. Sci.*, **70**, 465-486.

Zhang, C., and M. Dong, 2004: Seasonality in the Madden-Julian oscillation. *J. Climate*, **17**, 3169-3180.

Zhang, C., 2013: Madden-Julian Oscillation: Bridging Weather and Climate. *Bull. Amer. Meteor. Soc.*, **94**, 1849-1870.

Zhou, W., and J. C. L. Chan, 2005: Intraseasonal oscillations and the South China Sea summer monsoon onset. *Int. J. Climatol.*, **25**, 1585-1609.

Zhu, H., and H. Hendon, 2015: Role of large-scale moisture advection for simulation of the MJO with increased entrainment. *Quart. J. Roy. Meteor. Soc.*, **141**, 2127-2136.

Zuluaga, M. D., and R. A. Houze, 2013: Evolution of the population of precipitating convective systems over the equatorial Indian Ocean in active phases of the Madden-Julian Oscillation. *J. Atmos. Sci.*, **70**, 2713-2725.